

**Effects of Microstructure and
Strain Ageing on
Toughness of Nuclear PWR Reactor Weld
Metals.**

By

Victoria Jane Farron.

Volume I

A thesis submitted to the Faculty of Engineering of the University of Birmingham for the degree of Doctor of Philosophy.

School of Metallurgy and Materials.

The University of Birmingham.

Edgbaston,

Birmingham.

B15 2TT.

2009.

UNIVERSITY OF
BIRMINGHAM

University of Birmingham Research Archive

e-theses repository

This unpublished thesis/dissertation is copyright of the author and/or third parties. The intellectual property rights of the author or third parties in respect of this work are as defined by The Copyright Designs and Patents Act 1988 or as modified by any successor legislation.

Any use made of information contained in this thesis/dissertation must be in accordance with that legislation and must be properly acknowledged. Further distribution or reproduction in any format is prohibited without the permission of the copyright holder.

Genius is one per cent inspiration;
ninety-nine perspiration.

Thomas A. Edison

(1847-1931)

Acknowledgements.

Firstly, I would like to thank the EPSRC in conjunction with the Nuclear Installations Inspectorate Health and Safety Executive (NII HSE) for sponsorship and the University of Birmingham for granting me the great opportunity to pursue my Ph.D. education in the Department of Metallurgy and Materials.

I would like to thank Professor P. Bowen, for his interest and encouragement throughout this project. I am grateful to the late Dr R. D. Nicholson from the NII HSE for his input and continued interest in this thesis and subject area. I would like to thank all academic and technical support staff for their guidance and support in using the departmental facilities.

Technical assistance and useful advice from Dr M. Novovic are gratefully acknowledged. Additionally, special thanks are due to the members of the Fatigue and Fracture Group for their support and great friendship over the past 5 years.

Finally and most importantly, I would like to thank my parents for their unending support (mostly financial), encouragement and inspiration. Without them I would not be who I am. Also to my husband to be, Lee who has put up with the saying “When I have finished I could do.....” And who I love.

Synopsis.

The effects of microstructure and prestraining and ageing on ductile-to-brittle transition temperature, fracture toughness and cleavage fracture resistance of a multi-pass low-alloy ferritic steel weld metal have been investigated. The weld metal simulated submerged arc welds used in the fabrication of Sizewell B power station reactor pressure vessel. The study aimed to investigate differences in mechanical properties of a single microstructure; as-deposited and reheated microstructures and subjected to various mechanical tests. Additionally, to simulate the effects of irradiation embrittlement a number of specimens were prestrained and then statically strain aged. Charpy impact transition curves had obvious trends depending upon microstructure and condition, with microstructure having a significant influence on the transition region and upper-shelf impact energy level. Prestraining and ageing the specimens promoted an increase in the ductile-to-brittle transition temperature and reduction the upper shelf energy level for both microstructures. The extremes of behaviour were defined by the reheated as-received and as-deposited prestrained and aged conditions, being the “best” and “worst conditions” respectively. This trend was repeated with the crack-tip opening displacement tests. A combination of factors decreases toughness for the as-deposited prestrained and aged condition, which exhibited the highest yield stress, and lowest work hardening exponent and the best cleavage fracture resistance. Such factors result in marked upwards shifts in Charpy impact transition curves and decrease in the crack growth resistance curves.

Contents

Acknowledgements.....	3
Synopsis.....	4
Contents.....	I
Chapter 1 - Introduction.....	1
Chapter 2 - Literature Review.....	6
2.1 Pressurized Water Reactor.....	6
2.2 Neutron Embrittlement of Reactor Pressure Vessel (RPV Materials).....	9
2.2.1 Safety concerns about the introduction of PWR's in the UK.....	11
2.2.2 Further Safety Concerns: The Loss of Coolant Accident (LOCA).....	12
2.2.3 Micromechanics of Irradiation Embrittlement.....	13
2.2.4 Radiation Damage Dislocations in Ferritic/ Martensitic Steels.....	14
2.2.5 Interactions Between Dislocations and Irradiation-Induced Defects.....	15
2.2.6 Forces of Dislocations.....	16
2.3 Material Requirements.....	17
2.4 Cold Deformation.....	18
2.5 Other Embrittlement Mechanisms.....	20
2.5.1 Interactions Between Solute Atoms and Dislocations.....	25
2.6 Carbon-Manganese Welds.....	25
2.6.1 Fusion Welding.....	25
2.6.2 Submerged Arc Welding (SAW).....	26
2.6.3 Effects of welding process variables on C-Mn metal microstructures.....	29
2.6.4 Non-Metallic Inclusion Formation.....	32
2.6.5 Weld Pool Solidification.....	34
2.6.6 Transformations and Microstructural Development.....	36
2.6.7 Weld Microstructures and Nomenclature and Development.....	39
2.6.8 Multi-pass Welds and Reheated Microstructure.....	47
2.6.9 Previous work on the toughness of C-Mn weld metal.....	49
Chapter 3 - Fracture Mechanics.....	53
3.1 Linear Elastic Fracture Mechanics.....	53
3.1.1 The Griffith Theory.....	53
3.1.2 The Stress Intensity Factor Approach.....	56
3.1.3 Critical Tensile Fracture Stress, σ_f^*	61
3.1.4 Linear Elastic Fracture Mechanics (LEFM).....	63
3.1.5 Elastic Plastic Fracture Mechanics (EPFM).....	67
3.2 Microscopic Models For Cleavage Fracture.....	71
3.2.1 Stroh's Theory.....	71
3.2.2 Cottrell's Theory.....	73
3.2.3 Smith's Theory.....	75
3.2.4 Measurement of the Microscopic Cleavage Fracture Stress.....	76
3.3 Fracture Criteria for Precracked Specimens.....	77

3.3.1	Microstructural Effects on Cleavage Fracture.....	77
3.3.2	The Ritchie-Knott-Rice Model.....	80
3.3.3	Statistical Approach (RKR) model.....	81
3.3.4	The relationship between microscope cleavage fracture stress (σ_f^*) and macroscopic toughness parameter K_{IC}	82
3.4	Ductile Fracture	83
3.5	Ductile-to-Brittle Transition Region (DBTT)	85
3.6	Intergranular Failure	87
Chapter 4 -	Experimental.....	89
4.1	Introduction	89
4.2	Experimental.....	90
4.2.1	Material.....	90
4.2.2	Materials Plan	90
4.3	Thermo-Mechanical Heat Treatments	91
4.3.1	Cold Deformation Procedure.....	91
4.3.2	Static Strain Aged Condition.....	92
4.4	Material Characterisation	92
4.4.1	Microstructural Analysis	92
4.4.2	Inclusion Analysis	93
4.4.3	Glow Discharge Spectrometry (GDS).....	95
4.5	Hardness Tests.....	95
4.5.1	Macrohardness.....	95
4.5.2	Microhardness	96
4.6	Tensile Tests	96
4.6.1	5% Plastically Deformed and Strain aged at 300°C	98
4.7	Charpy Tests.....	99
4.8	Slow Blunt Notch Bend Tests	102
4.9	Crack Tip Opening Displacement (CTOD).....	104
4.9.1	Test Specimens	105
4.9.2	Fatigue Precracking	105
4.9.3	Potential Difference Technique.....	106
4.9.4	Testing	107
4.10	Fractography.....	109
Chapter 5 -	Results - Materials Characterisation.....	111
5.1	Introduction	111
5.2	Results	112
5.2.1	Microstructure	112
5.2.2	Inclusion Analysis	113
5.2.3	Glow Discharge Spectrometry (GDS).....	115
5.2.4	Macrohardness.....	115
5.2.5	Microhardness	117
5.3	Discussion.....	118
5.3.1	Microstructure	118
5.3.2	Hardness Tests.....	119
5.4	Conclusions	123
Chapter 6 -	Results - Tensile and Charpy Tests.	125
6.1	Introduction	125
6.2	Results	125

6.2.1	Tensile Testing	125
6.2.2	Analysis of Charpy Tests.....	130
6.3	Fractography.....	133
6.3.1	Tensile Tests	133
6.3.2	Charpy Tests	134
6.4	Discussion.....	136
6.4.1	Tensile Testing	136
6.4.2	Charpy Tests	141
6.5	Conclusions	147
Chapter 7 -	Results – Slow Notched Bend Tests.....	149
7.1	Introduction	149
7.1.1	Results	150
7.2	Fractography.....	153
7.3	Discussion.....	155
7.3.1	Blunt Notch Tests	155
7.3.2	Previous proposed model for cleavage fracture in C-Mn weld metal.	155
7.3.3	Static strain ageing effect on cleavage fracture.	156
7.3.4	Plastic deformation and strain ageing in low alloy ferritic steel weld metal....	157
7.3.5	Relative position between maximum principal tensile stress (σ_{yymax}) and the cleavage initiation site.	159
7.3.6	Relationship between inclusion size and local cleavage fracture stress, σ_{X0} . ..	161
7.4	Conclusions	162
Chapter 8 -	Results - Crack Tip Opening Displacement (CTOD) Tests.	164
8.1	Introduction	164
8.2	Results	164
8.2.1	Fatigue pre-cracking.	164
8.2.2	CTOD Results for Weld N ^o 1.....	165
8.2.3	CTOD Results for Weld N ^o 2.....	167
8.3	Fractography.....	169
8.4	Discussion.....	171
8.4.1	CTOD values.	171
8.4.2	Modelling Cleavage Fracture.	173
8.4.3	δ -R Data Validity.....	174
8.4.4	Fractography.....	176
8.5	Conclusions	178
Chapter 9 -	General Discussion.....	179
9.1	Introduction	179
9.2	Comparison of impact transition curves and CTOD values.....	179
9.3	Trends between Weld N ^o 1 and Weld N ^o 2	182
Chapter 10 -	Conclusions and Suggestions for future work.	185
10.1	General Conclusions.....	185
10.2	Suggestions for Future Research	188
Chapter 11 -	References.....	190

Chapter 1 - Introduction.

The nuclear power industry has been developing and improving designs for reactor pressure vessel (RPV) technology for over 50 years. In the past 30-40 years the importance of the design against brittle failure has been emphasised, as failure of this nature is catastrophic. Structural integrity of engineering structures is of fundamental importance for safe operation, as in-service failures may result in widespread damage and fatalities. Considerable effort is made to ensure that components can resist failure under every condition and operation, e.g. start-up, normal, loss of coolant (LOCA) and shutdown [1-6]. Around the world, 31 countries have a combined total of 440 commercial nuclear reactors. About 22% of the electricity produced in the UK today comes from nuclear power stations, with a quarter of these being Magnox reactors. The expected service life of these reactors was originally 20 to 25 years, however all but one of these plants has exceeded its projected life. The continued operation and the future of nuclear power plants depends on many issues arising from day to day operation and maintenance to plant ageing, with the most important factor being the continued safe operation of the nuclear plants. The main mechanisms affecting the ageing of the lifetime operation of the nuclear reactor is neutron embrittlement [7, 8].

The nuclear industry has been improving technology from the first commercial concept, Calder Hall in 1956 which had prototype reactors called “Magnox Gas Cooled Reactors” and following successful operation nine full scale Magnox power stations were built in the UK, as well as one each in Italy and Japan. Out of these eleven, three have now been decommissioned. From the original Magnox concept, there have been new designs and developments of light water technology. Pressurized water reactors (PWR) and advanced boiler water reactors (ABWR) have been built in the USA and Japan. A large proportion of contemporary nuclear power is supplied by light water reactors whose cores are contained within RPVs, and which must safely operate at temperature of $\approx 290^{\circ}\text{C}$ [6, 9-11] and pressures of $\approx 7\text{MPa}$ in a BWR and $\approx 14\text{MPa}$ in a PWR. Other nuclear technologies are CANDU (Canada Deuterium Uranium) based on natural uranium moderated and cooled by heavy

water, experimental pebble bed modular reactor (PBMR) and advanced gas cooled reactors (AGR), of which there are seven in the UK. Some of these technologies are already active and producing electricity, bringing advantages of low capital investment, modular construction, reduced construction time and increased efficiency.

Over the last 40 years research has been carried out worldwide in to the modelling of neutron irradiation and more recently emphasis has been placed on the understanding the mechanisms that cause embrittlement. The assessments of nuclear power plant standards are monitored by the UK regulatory regime, whose main objective is to continually assess and monitor the effects of neutron irradiation on the mechanical and fracture properties of materials within the plant.

Surveillance programmes monitor the effects on mechanical and fracture properties of neutron irradiation of the pressure vessel steel (RPV). Neutron irradiation causes an embrittlement process, which consequently results in an increase in the ductile-to-brittle transition temperature (DBTT) and decrease in fracture toughness properties, e.g. ductility. Surveillance programmes highlighted with some concern that submerged-arc welds were the most severely affected areas of a vessel, and have resulted in the adjustment of operational parameters of some plants to offset the effects of embrittlement.

The efficiency of a nuclear power plant is governed by the maximum temperatures and pressures that can be safely maintained. Safe operation of a reactor pressure vessel is governed by maintaining the temperature and pressure within set margins relative to their maximum values. In the UK, these parameters are established by considering both resistance to plastic collapse and brittle fracture using the R6 failure assessment diagram (BS 7910) [12]. The assessment uses information on the size of defects assumed to be present in the vessel, operating stresses, tensile properties of the pressure vessel steel and temperature dependence of fracture toughness of the particular steel. Tensile properties can be ascertained from surveillance programmes of the irradiated material; however the temperature dependency of

fracture toughness for irradiated material has to be derived from comparing start-of-life material to irradiated materials removed during the surveillance programme. However, such programs are limited by the amount of materials that can be removed, due to the difficulty involved in the acquisition of the specimens as well as the high costs involved. Due to this lack of relevant data large uncertainties can occur as these are an important factor in achieving accurate embrittlement trend equations.

This thesis attempts to address some of these issues in the structural integrity assessment of a Pressurised Water Reactor (PWR) vessel. The particular weld metal investigated closely matches the start-of-life properties of the “Sizewell B” pressurised water reactor, commissioned by the Nuclear Installations Inspectorate (NII HSE) and produced by ESAB Group UK. The effects of irradiation were simulated by a prestraining treatment; this process permitted unlimited use of large numbers of sample pieces tested under various conditions to assess the changes in flow and toughness properties. The programme was set up to investigate the effects of material microstructure, prestraining and static strain ageing of mechanical properties of the weld metal. This series of experiments follow on from previous programmes which had studied the effects of microstructure and prestraining on the mechanical properties of carbon-Manganese steel (C-Mn steel) weld metal, similar to that used in Magnox type reactors. The preceding tests were carried out in work by Novovic [13] and also work carried out by both Wenman [14], using a simulated Mn-Mo-Ni weld metal produced by the TWI, and do Patrocínio [15], who used a similar A533B weld. These studies were commissioned by the NII and all the studies revealed a difference in the toughness of the weld metal, between the as-deposited and reheated microstructural regions.

Mechanisms of neutron embrittlement in low alloy ferrite steels such as MnMoNi weld metal are reviewed in Chapter 2. Also presented are other known embrittlement mechanisms, such as dynamic and static strain ageing. They are compared to rationalise the use of cold deformation to simulate irradiation embrittlement. The submerged-arc welding process is reviewed in this chapter, as well as the weld pool solidification process and solid phase

transformations that lead to the final microstructural constituents of the weld pool. The effects of alloying elements on the final weld microstructure are also considered.

Chapter 3 outlines the Linear Elastic Fracture Mechanics (LEFM) and Elastic Plastic Fracture Mechanics (EPFM), whilst presenting the concept proposed by Griffith and the extension of this theory by Orowan-Irwin. Also reviewed are the microscopic models for cleavage failure proposed by Cottrell, Smith, Stroh and Ritchie-Knott-Rice (RKR) model for fracture criteria.

Chapter 4 describes the different experimental procedures and techniques which were performed throughout this thesis, including the cold deformation and thermal ageing procedures employed as well as Charpy Impact testing, Crack-Tip Opening Displacement, CTOD, tensile testing and Blunt notch testing.

Chapter 5 describes the material characterisation of the different weld metal samples presented within this thesis. Discussing the results obtained from Energy Dispersive X-ray analysis (EDX), Glow discharge spectrometry (GDS), both macro and micro hardness testing and inclusion analysis.

The effects of the strain hardening and thermal ageing of the weld metal are compared with the as-received weld metal with respect to various microstructures as well as the flow properties of the material and the Charpy energy absorbed are presented in Chapter 6.

Chapter 7 reports the effects of the prestraining and ageing treatment on the fracture resistance by calculating the intrinsic local cleavage fracture stress.

Chapter 8 examines the effects of prestraining and ageing on the fracture toughness of the weld metal, assessed in terms of CTOD) across a wide temperature range, -196°C to room temperature, Assessing the fracture toughness for both the microstructures and in both conditions; As-deposited As-received: ADAR, Reheated As-Received: RHAR, As-deposited 5% strain and statically aged: AD5%SA and Reheated 5% strain and statically aged: RH5%SA.

A general discussion of the effects of prestraining and static strain ageing on the mechanical properties of the weld metal are presented in Chapter 9. Chapter 10 summaries the main conclusions found in this work.

Chapter 2 - Literature Review.

2.1 Pressurized Water Reactor

The pressurized water reactor (PWR) is a generation II nuclear power reactor that uses ordinary water under high pressures as a coolant and neutron moderator, with the primary coolant loop kept pressurized to prevent the water from boiling. PWRs are the most common type of commercial reactor in the world, and were originally designed by Bettis Atomic Power Laboratory in the USA for naval use, especially submarine propulsion. The first nuclear submarine of this type was the Nautilus, launched in 1945 and the vessel remained in service until 1983. More than 60% of the world's commercial reactors are PWRs, with the rest being gas-cooled or heavy-water reactors. The world's first fully operational reactor was demonstrated at Oak Ridge, USA. The X-10 graphite pile was designed and built within ten months and went into operation in November 1943. The pile was built to irradiate natural uranium to produce plutonium which could be recovered and purified. This plutonium was used to produce the second Atomic Bomb developed, which was dropped onto the city of Nagasaki, Japan on August 9 1945. In 1953, the world's first commercial nuclear power station, Calder Hall was under construction in the UK and connected to the grid in 1956 [16]. Calder Hall was the prototype for reactors called "Magnox Gas Cooled Reactors" and following the success of Calder Hall nine full scale power stations were built in the UK, as well as one in Italy and Japan. These stations use natural uranium metal, encased in non-oxidising magnesium alloy (hence the MagNOX acronym) as fuel and carbon dioxide as the gaseous coolant.

In 2005, world-wide nuclear generation capacity was approximately 381 Gigawatt days, which corresponds to approximately 16% of the world's electricity generation. As of October 2005 there were 441 nuclear reactors currently known to be operating in 34 countries, with a further 30 planned in 11 countries, notably in China, South Korea and Russia. The UK

currently has a total of 23 reactors on 12 sites providing approximately 20% of the UK's electricity supply. A map showing the current locations around the world is shown in Fig. 2.1

A nuclear reactor works by allowing fissile materials in the nuclear fuel to become engaged in a chain reaction in the reactor pressure vessel; energy is released continuously by a fission process maintained within the reactor core. Large amounts of heat are released; this heat energy is transferred from the core via a circuit of normal light water which acts as both the moderator and coolant through the reactor. This primary coolant loop is pressurised so that the water does not boil. The water within the reactor core reaches temperatures of approximately 325°C, remaining liquid under approximately 150 times atmospheric pressure (≈ 150 bar). The more modern reactors use uranium dioxide (UO_2) enriched to 3.2%. This allows higher “burn up” (energy release) from the fuel and the ceramic UO_2 pellets are contained within Zircaloy (zirconium alloy) tubes. Within the reactor core, the primary cooling circuit is a neutron moderator, so if any of the water turned to steam the fission reaction would slow down; this negative feedback effect is called a negative void coefficient, and is one of the main inbuilt safety features of a PWR. Many PWRs have a secondary shutdown system which involves injecting a strong neutron absorber such as boron, into the primary circuit, as shown in Fig. 2.2 and 2.3. Boron is also routinely added into the primary coolant water during normal operation as this allows more enriched fuel to be used, increasing the potential “burn up” for the fuel in the reactor. However, a drawback to this is it makes the cooling water corrosive. The heat raised in the reactor is passed from the primary to a secondary coolant circuit via heat exchangers, where the energy is converted to steam at approximately 70 bar and 280°C. The high-pressure steam then drives the turbine to produce electricity, the steam then condenses back into water and returns to the heat exchangers by the primary coolant loop. The thermal efficiency is approximately 32% and with the design is also inherently safer than those of boiling water reactors (BWR).

Sizewell B is located in Leiston, Suffolk and is the only commercial pressurized water reactor, PWR, within the UK. Construction of Sizewell B started in 1987 and the power station was finished in 1994, when it was connected to the main electric grid, originally

designed for a commercial life of 40 years; around 2035, although similar stations elsewhere in the world have been granted extensions to a total of 60 years. The site is owned and maintained by British Energy, who also own mainly nuclear sites in the UK; including Hinkley Point B and Hunterston B. Sizewell B can produce a maximum of 1200 MW and works continuously throughout the year generating electricity for more than 1.5 million people and supplies 3% of the UK's total energy needs.

An aerial view of Sizewell B is shown in Fig. 2.4 and the reactor is contained within a concrete biological shield and that is contained within further secondary containment. The casing acts a radiation shield and is designed to prevent the release of radioactivity into the environment. The design is very compact compared to earlier reactors as water is a more effective moderator than graphite. Thermal energy produced by the reactor system is carried away by pressurised water; the thermal energy is used to create steam in the secondary water circuit and passed through two turbines. Each turbine comprises of one high-pressure cylinder and three low-pressure cylinders, driving a 62.5 MW generator, operating at 23.5 kV, which is then raised to 400 kV, to be supplied to the national grid. As with many other PWRs, Sizewell B was intended to be operated on an 18 month operating cycle, at around 100% continuously for around 17 months and followed by a month's shutdown for maintenance and refuelling. PWR vessels have a cylindrical shell design; ranging from 3.0-5.0 metres in diameter and range from 12-15 meters in height. The thickness of the reactor pressure vessel is around 0.25 meters and is subjected to multi-axial loading. It is designed to withstand hostile environments, accidents and changes in transient conditions by decreasing temperatures or pressure. The reactor pressure vessel is made from nuclear grade steel forgings. These forgings are welded together using a submerged-arc process.

2.2 Neutron Embrittlement of Reactor Pressure Vessel (RPV Materials)

The reactor efficiency is governed by the high internal temperature of fluid, which is also at relatively high internal pressures. The vessel material must not only be resistant to this hostile environment, it must also be resistant to the constant bombardment of high-energy neutrons radiating from the enriched uranium-235 enriched fuel, as well as the alpha α , beta β and gamma γ radiation of uranium isotopes and fission products. When the high-energy neutrons pass through the weld belt-line, plate and forgings of the pressure vessel; they cause very intense but local damage, which may cause the steel atoms to be displaced from their normal position. When the first Magnox power stations were built the effect and mechanisms of irradiation embrittlement on welds were not well understood. At the normal operating temperature of the reactor pressure vessel (RPV) these displaced atoms can quickly return to their position, however there is a small change in the atomic structure of the remaining steel. Thus over the operating life of the RPV, which can be many years, even decades these small changes can accumulate to result in significant changes in mechanical properties, as a consequence of embrittlement of the steel. Despite this effect there are very few models physically based explaining or clarifying the underlying mechanisms of neutron embrittlement in RPV steels. It is well understood that the material's strength usually increases under these conditions, which by itself is not necessarily a deleterious effect, however the increase in strength also causes a loss in the material's toughness, Fig. 2.5. Neutron irradiation effects the material by raising the ductile-to-brittle transition temperature and reducing the toughness. Clearly this increasing brittleness will change the safe operational limits of the materials according to the R6 procedure [12, 17].

The changes in the properties of the RPV can be monitored through surveillance programmes which measure the shifts in ductile-to-brittle transition temperatures (DBTT) and the upper shelf energy (USE) level reduction using Charpy impact tests. Thus start of life properties need to be accurately defined in terms of Charpy impact transition curves, transition temperatures are compared at 40 or 41J. These values originate from the nil ductility

temperature of Pellini drop weight test used on ship steel plate from the World War II Liberty ships where 28J occurs at the nil ductility temperature, Fig. 2.6 [18]. This is the equivalent value of 30 ft. lb (40.7J) [19] therefore has found favour within the nuclear industry for the same reason, i.e. it occurred at the nil ductility temperature of commonly used higher strength steels for nuclear RPV's. The nuclear industry found acceptance in the relationship between the transition temperature at 40J (ΔT_{40J}) showing an equal temperature shift at 100 MPam^{1/2} for fracture toughness tests [19].

The RPV can tolerate modest reductions in toughness without any loss of integrity, due to the conservative design codes, however large changes must be avoided. The materials and the weld metals which go into constructing the RPV are selected to minimise the effects of neutron embrittlement and today most weld metals used in the fabrication of the RPV have better toughness than the steel plates they weld together. Early weld metals contained trace amounts of copper in their composition, which made the weld more sensitive to the effects of neutron irradiation than the steel plates. Shown in Fig. 2.7 displays the change in toughness in a submerged arc weld metal with 0.23% copper content, due to the neutron embrittlement as an example, the sample was tested by workers at the Oak Ridge National Laboratory [20]. The figure shows the copper contribution remains unchanged after the development of the maximum value, it can also be seen that the position of the plateau increased with a corresponding increase in copper content. This example demonstrates that for materials with a high copper content, a higher shift in Charpy Impact toughness from neutron irradiation is to be expected. As the weld metal strength increases, the impact toughness transition region shifts to higher temperatures by nearly 100°C and the upper shelf impact toughness is reduced by 1/3. There are several different regulations that limit the upper shelf energy and transition temperatures; if either of these limits is projected to be exceeded then additional analysis may be required. In some cases the continued operation of the power plant can not be justified due to the levels of embrittlement, without reducing the embrittlement by thermal annealing.

2.2.1 Safety concerns about the introduction of PWR's in the UK.

The British government during the 1970's considered nuclear power as a clean method for providing the future power requirements in the UK. The Central Electricity Generating Board (CEGB) favoured introducing a PWR, as of the type used in the USA and marketed by the Westinghouse Electric Corporation; however there was a debate in the UK over the safety of such reactors. Two particular issues were raised:

1. In the event of a major rupture of the primary cooling circuit, would the emergency core-cooling water system (ECCS) be able to prevent the nuclear fuel elements overheating, melting and releasing their fission products?
2. Could the pressure vessel, which contains the nuclear core fail catastrophically?

The Nuclear Health and Safety Executive Nuclear Installations Inspectorate (HSE NII) were asked to investigate these concerns by the government. The Marshall Report [21] states that failures of such a structure can occur by two distinct mechanisms; non-ductile failure and ductile failure.

2.2.1.1 Non-Ductile Fracture

The first of these mechanisms is termed non-ductile fracture and used to describe mechanisms in which plastic collapse through the section thickness does not occur before the structure fails.

2.2.1.2 Ductile Fracture

This second mechanism occurs when a section of a structure is stressed to a level beyond the ultimate stress of the material, thus the material is yielding plastically and permanently deforming. The material begins to deform more and more, resulting in the load bearing area being reduced further and eventually to the material breaking.

Non-ductile fracture formed part of a research programme, which is still in progress today. The issues were raised by Sir Alan Cottrell, the then Government Chief Scientist, and he recognised that the likely failure of a pressure vessel of the Westinghouse type of PWR was “rapid fracture” or non-ductile. The term rapid fracture implies failure extending from a crack, which is smaller than the wall thickness of the vessel, and growing in an unstable manner within the pressure vessel wall. This can occur in sections that are thick enough to produce plain strain conditions, which is possibly within the Westinghouse design. As a result of this, the “leak-before-break” scenario, a safety feature of the vessel leaking before catastrophic failure occurs, is not available. This means the critical size of defect e.g. another flaw or crack, of sufficient size to propagate in an unstable manner, for a given wall thickness of the pressure vessel must be determined, and a method found to allow detection by non-destructive testing methods.

2.2.2 Further Safety Concerns: The Loss of Coolant Accident (LOCA)

Attention was paid to accidents which could possibly occur during the operation of the RPV and could question the integrity of the vessel. One such accident is LOCA-loss of coolant accident, the most severe form is accompanied with rupture of the primary coolant pipe, such that the pressure within the primary cooling system falls instantly to atmospheric and the coolant temperature drops from 291°C within the next 45 seconds. This sudden depressurisation is accompanied by a sharp thermal gradient, which is of significant

importance as the possibility of RPV material decreasing in temperature from the upper shelf to a transition region temperature could allow for unstable brittle fracture of a pre-existing flaw; the driving process is thermal shock of the vessel. Mechanisms of fracture become more important because the reactor pressure vessel is ageing in service and the temperature at which brittle fracture can occur increase with the increasing irradiation dose. A loss of coolant incident has a more significant effect by allowing the core to become uncovered (i.e. no heat removal from the fuel modules), thus leading to possible melt down of the reactor.

2.2.3 Micromechanics of Irradiation Embrittlement

Research carried out into irradiated steels of the type used for making reactor pressure vessels has identified three main micromechanisms of irradiation embrittlement [1, 9, 11, 22-31]

1. Precipitation damage through the formation of copper-rich precipitates, direct evidence of copper-rich precipitates; leading to the formation of precipitates or clusters, which are enhanced with Cu, Mn, Ni and Si, have been obtained using various microstructural techniques (transmission electron microscopy (TEM), scanning transmission electron microscopy and small angle neutron scattering, etc.) [1, 4, 5, 23, 32-36].
2. Formation of point defect clusters (cluster of vacancies and interstitials) and dislocation loops (due to fine scale of this matrix damage, the direct evidence is hindered; the effect is inferred through changes in mechanical properties). The effect of matrix damage is reflected in an increase in the athermal part of lattice friction stress component of yield stress [30, 37, 38].
3. Irradiation induced/ enhanced segregation of impurity elements (such as phosphorus) to grain boundaries [5, 26, 27, 30, 39].

The first two mechanisms harden the material; therefore there is an increase in the yield strength, while the third mechanism decreases the fracture strength. The last two effects are

also a consequence of the first, meaning that in unirradiated steel both phosphorus segregation and copper precipitation occur at high temperatures, around 500°C, compared to the operating temperature of a reactor pressure vessel. Therefore, the increased concentration of vacancies caused by high-energy neutrons increases the diffusion of copper and phosphorus and as a result the phenomenon can occur at lower temperatures.

Reactor pressure vessel (RPV) steels, operating at temperature 280°C are exposed to low-dose neutron irradiation which is known to result in hardening and embrittlement and which contributes to the production of radiation damage defects. Although there have been numerous investigations, the matrix component of damage has not been identified, it is currently thought that it consists of sub-microscopic vacancy-impurity complexes or impurity stabilized microvoids.

2.2.4 Radiation Damage Dislocations in Ferritic/ Martensitic Steels

The type of steel being used in this study is affected by irradiation at temperatures below 400°C as a consequence both hardening and embrittlement are effected. Irradiation damage accumulation in steels is much slower than in some other metals and this damage takes the form of defect clusters of interstitials, vacancies, and dislocation loops, which appear as small black or white dots when using TEM, dependant upon the imaging conditions. Dislocation loops or second phase particles are generally greater than 5nm in length, smaller dislocation

loops have Burgers vectors of $b = \frac{1}{2}\langle 111 \rangle$, for larger loops these have a Burgers vector of $b = \langle 100 \rangle$. These loops are interstitial in nature. Voids or bubbles may be resolved at higher doses, while vacancy clusters do not resolve at lower doses.

2.2.5 Interactions Between Dislocations and Irradiation-Induced Defects

Dislocations move producing slip when sufficient external force is applied to the material.

Within a bcc lattice, slip occurs in the $\langle 111 \rangle$ close-packed direction the corresponding

Burgers vector is $\left(\frac{a_0}{2}\right)[111]$, this is a common direction in any of the following plane: (110), (112) and (123). Slip has been found to occur on (110), (112) and (113) planes in iron. While the slip plane is generally (110), there are three (110) type planes that intersect the [111] direction. Within the body-centred cubic lattice (111) planes are close-packed and intercept

more atoms than any other. Screw dislocations with Burgers vectors of $\left(\frac{a_0}{2}\right)[111]$ may move at random onto one of the (111) planes with a high resolved shear stress. This phenomenon is the source of a poorly defined slip plane in iron [40].

Cottrell [41, 42] proposed a dislocation reaction in a bcc lattice, which appears to lead to the formation of immobile dislocations; this reaction has been shown to be a mechanism for producing a crack nuclei that may lead to brittle fracture. Shown in Fig. 2.8, dislocation A

with Burgers vector $\left(\frac{a_0}{2}\right)[\bar{1}\bar{1}1]$ is moving on the plane (101), whilst intersecting with B with

a Burgers vector of $\left(\frac{a_0}{2}\right)[111]$ and gliding on an intersecting plane of $(10\bar{1})$. The two dislocations come together and react to lower the strain energy by providing a pure edge dislocation which lays on the (001) plane.

$$\frac{a_0}{2}[\bar{1}\bar{1}1] + \frac{a_0}{2}[111] = a_0[001] \quad \dots(2.1)$$

The dislocation is immobile since the (001) plane is not a close-packed slip plane in the bcc lattice. The (001) plane is the cleavage plane along which brittle fracture occurs [40]. There has been extensive research into dislocation interactions, using various methods such as atomistic modelling and in-situ TEM, this has mostly been carried out on fcc metals. This research has concluded that screw dislocations are more effective than edge dislocations at removing defects; however the defect is not destroyed by the interaction with just one dislocation. The stress required for a dislocation to break free from a defect can be determined from its curvature prior to breaking away. A range of strengths may be presented dependant on the obstacle's interface/ interaction with the matrix, this is reflected by different interactions geometries and interactions with different defect types. In contrast very few studies have been carried out in ferritic materials, which present more of a problem from an experimental point of view (difficulty in observing ferromagnetic materials using an electron microscope) and theoretically (difficulty of developing a reliable potential for atoms with magnetic moments). However, TEM observations by Nogiwa [43] of movement of edge dislocations through ultrafine obstacles (believed to be small Cu precipitates) in a Fe-Cu alloy, and made estimates of obstacle strength.

2.2.6 Forces of Dislocations

A slip line forms when a dislocation moves when there is a force acting on it (shear stress τ), this moves the dislocation in the direction of its Burgers vector, shown in Fig. 2.9. An element of the dislocation line ds is moved in the direction of slip normal to ds by an amount dl [40]. The area swept by the element is $dl ds$. The crystal is displaced by $(ds dl/A)b$, which is a comparison of the amount above the slip plane relative to the amount below, where A is the area of the slip plane. Thus the work done by the applied force creating the applied stress τA , when increment of slip occurs

$$dW = \tau A \left(\frac{dsdl}{A} \right) b \quad \dots(2.2)$$

and

$$F = \frac{dW}{dsdl} = \tau b \quad \dots(2.3)$$

where F is the force per unit length of dislocation line.

The dislocation line is perpendicular to the force and it is constant at any point selected along the line, if τ is constant, then the Burgers vector is constant along a curve dislocation line, resulting in the force on a dislocation not necessarily in the same direction at the applied stress.

2.3 Material Requirements

The environmental and operating conditions to which reactor pressure vessel (RPV) materials are subjected to during the operational lifetime are very severe. The specification of the material is such that it cannot fail by either ductile or plastic collapse mechanism, by a brittle catastrophic failure mechanism. For this to be achieved standards for the material are set by nuclear regulatory guidelines [33, 44] and design codes (e.g. ASME Boiler and Pressure Vessel Code) [45, 46] must be followed during the design and operation of the components. Hence, within these guidelines fracture toughness is an essential material property and therefore carefully considered in the selection of material. It is not feasible to discuss design codes without first defining the yield stress and the fracture toughness. The yield stress is the

point at which a material stops behaving in an elastic manner according to Hooke's Law and begins to deform plastically, i.e. it no longer returns to its original shape. Fracture toughness is simply a measure of the material's resistance to fracture in the presence of a sharp pre-crack. This is explained and examined in further detail in Chapter 3. For fracture to occur under linear elastic conditions, which is essentially the brittle type of fracture, then the stress intensity factor, K , of the material must not exceed the fracture toughness values or critical values, K_{IC} . K_{IC} corresponds to the stress at the crack tip needed to cause failure or fracture on Mode I opening (pure tension) whilst under plane strain (triaxial stress state) conditions. As a consequence, the material for the RPV needs to operate within defined maximum and minimum levels for both operating temperatures and pressures. These values are defined by the design codes and guidelines (e.g. ASME codes) [45, 46], in order to avoid either plastic collapse or rapid failure. Some of the materials chosen for RPV are known as A508 and A533B steel for plate and forging materials, these alloys are chosen as they are relatively low cost ferritic steels with yield and tensile strengths not high enough to promote catastrophic brittle failure but strong enough that plastic collapse is avoided. The steel's chemical composition is closely controlled, keeping levels of certain elements low, such as Ni, P and Cu, due to their embrittling effects during irradiation. Following neutron irradiation exposure, possible mechanical changes are monitored through surveillance programs throughout the operational life of the reactor pressure vessel using Charpy impact test on specimens removed from the base, weld and heat-affected zones of the material.

2.4 Cold Deformation

Irradiation embrittlement can be characterised by one embrittling mechanism (segregation of impurity elements at grain boundaries) and two hardening mechanisms (matrix damage and copper precipitation). Designing a simulation treatment that would produce similar mechanical behaviour to that of irradiated material is both complex and difficult due to these micromechanisms [13, 14].

Groom and Knott [47] studied the effects of prestraining on transition temperature and fracture stress shifts in mild steels, noting that prestraining caused a slight increase in the fracture stress, (increased yield stress due to work hardening overcomes the improvement in fracture stress, thus the overall effect is an increase in the ductile-to-brittle transition temperature (DBTT)). Following on from this Novovic [13] applied a simple cold deformation process, intended to achieve an increase in yield stress and a reduction in work-hardening rate, similar to those of irradiation embrittlement, Fig. 2.10. Prestraining is considered as a good approximation of matrix damage through the formation of clusters of vacancies, interstitials and dislocation loops. The effect of hardening due to copper precipitation can also be achieved, even though the micromechanism of these two processes is quite different, but the third of this irradiation micromechanism, irradiation-induced grain-boundary segregation of impurity elements (primarily phosphorus) cannot be achieved by prestraining. The main effect of segregation is a reduction in the materials fracture stress with no apparent alterations to the flow properties [13-15].

Novovic [13] used prestraining only as a first order simulation of irradiation, where as in previous work by Patrocínio [15] and this present work the MnMoNi steel weldment was subjected to 5% cold deformation to simulate the effects of neutron irradiation, an additional step was introduced of static-strain ageing at 300°C, this temperature is close to the operating temperature of a PWR [9, 27]. It should be noted, this temperature does not induce the segregation of phosphorous or copper precipitation during the ageing process of the weld unirradiated steel. These micromechanisms tend to occur at higher temperatures around 500°C.

Cold-working also has the important effect of shifting the transition temperature of body-centred cubic metals. Thus general effects of irradiation on the RPV weld metal can be readily simulated through prestraining and ageing treatments. The advantage of this choice of programme is that it allows unlimited samples of welded material that can be tested to infer the effect of irradiation on the temperature dependence of the materials toughness. The interaction of dislocations with foreign atoms and irradiation-induced defects has been

discussed and several studies carried out [3, 30, 33, 48-50]. Dislocation theory has been used to give a qualitative picture of solid-solution hardening (C and N mechanisms in irradiated RPV steel) and explaining strain ageing mechanisms and yield point behaviour. However the neutron irradiation atmosphere causes point defect clusters to form (clusters of vacancies and interstitials) as previously discussed.

Forming operations can have an influence on the materials responses and influenced by the strain rate at which it is being deformed. For practical purposes the rate of strain can be considered to have little effect because for cold working a change in strain of several orders of magnitude would result in only a 20% increase in the flow curve. There is a well established phenomenon known as the Bauschinger effect [40, 51] which is common in polycrystalline metals which have been deformed plastically, e.g. cold-worked. It states that a lower stress (σ_{ys}^b) was needed to reverse the slip direction on a certain plane than to continue slip in the original direction (σ_{ys}^c), shown in Fig. 2.11.

2.5 Other Embrittlement Mechanisms

Other embrittlement mechanisms are known to operate in irradiated and unirradiated pressure vessel steels due to the influence of interstitial elements like C and N on the mechanical properties of low alloy ferritic steel through static strain ageing (SSA) and dynamic strain ageing (DSA). The normal operating inlet temperature of the PWR is 288°C, which is within the temperature region where strain ageing occurs in plain carbon steels. Steel heated to temperatures ranging from 230 and 380°C shows a decrease in notch-impact resistance and tensile ductility, this temperature range is known as blue brittleness and steels in this region show a minimum in strain-rate sensitivity and maximum rate of strain ageing. Research [30, 32, 52-63] has been carried out to understand this phenomenon and the combined effect of strain ageing and radiation damage due to neutron embrittlement on RPV materials, most research has focused on dynamic strain ageing [35, 36].

Strain ageing is associated with yield-point phenomenon; the metal exhibits an increase in strength as well as a decrease in ductility on heating at relatively low temperatures preceding cold working. Strain ageing is a fairly common phenomenon in body centred cubic metals. Strain ageing also produces a low value of strain-rate sensitivity as well as increasing the yield stress and seeing the appearance of the yield point. This can be subdivided into dynamic strain ageing (DSA) and static strain ageing (SSA).

Within the plastic zone ahead of the crack tip strain ageing may occur. This can be static strain ageing, as the material has already been plastically deformed and then aged. It can also have a dynamic component as ageing occurs when the plastic zone is exposed to creep deformation. BCC metals are prone to strain ageing when interstitial atoms such as N and C, are present in sufficient quantities. Strain ageing is caused by elastic interaction between dislocations and interstitial atoms. BCC metals and alloys can exhibit extreme sensitivity to small additions of interstitial atoms. Solute atoms collect around dislocations and pin them in one place. In order to free the pinned dislocation an increase in stress is required. This increase in stress is greater than normally required to move the dislocation due to having to overcome increased pinning by solute atoms and the stress increases with plastic strain. With the continuation of plastic deformation the density of mobile dislocations increases. Also there is an increase in interactions between solute atoms and mobile dislocation.

Both static and dynamic strain ageing in steels are a result of interactions between dislocation and interstitial solute atoms, predominantly nitrogen and carbon. Low-carbon steels are susceptible to strain ageing, this involves a gradual change in certain properties over time (e.g. strength and hardness) after plastic straining. Both the static and dynamic strain ageing mechanisms affect the plastic deformation or work hardening behaviour, as well as increasing yield stress and decreasing ductility. Ageing is aided by temperature; at room temperature ageing occurs slowly, while changes occur more rapidly at elevated temperatures, due to increased diffusion rates. Strain ageing results in the reappearance of the upper yield point and yield point elongation in the samples. Chakravartty [54, 55] carried out a study into the kinetics of strain ageing, the result of which suggested that the strain ageing phenomenon is

controlled by an interstitial in solution, probably nitrogen. The microstructure did not appear to have any influence on the changes in mechanical properties observed due to strain ageing. A study of ASTM A533B Class 1 type of steels which had received a post weld heat treatment, and exposed to ageing temperatures of 300 to 550°C was carried out. Charpy impact testing indicated an increase in the ductile-to-brittle transition temperature (DBTT); this was dependent on the original material, the heat treatment applied and the ageing time, but had relatively little influence on the upper shelf energy, Fig. 2.12. It was also shown that the primary cause of embrittlement upon ageing was segregation of phosphorus to the prior austenite grain boundary over the ageing temperature range.

The dynamic strain ageing mechanism is rapid and occurs during the straining process, whereas static strain ageing occurs slowly. Strain ageing is aided by elastic interactions between interstitials and dislocations within steels, resulting in strong dislocation pinning. Dynamic strain ageing occurs when the magnitude of strain is such that interstitials can diffuse and then pin mobile dislocations. Segregations occur due to a rapid generation of new dislocations and the stress increases, but once the dislocations are released the stress decreases to sustain movement until interstitials diffuse and repin these dislocations. Due to the rapid generation of dislocations this leads to inhomogeneous deformation. This is characterized by serrated flow called Portevin-Le Chatelier effect (PLC). This effect can be characterised by a decrease in the toughness resistance and may occur at room temperature or on heating at 230 to 380°C. The strain ageing phenomenon is related to the diffusion of free carbons and nitrogen atoms to dislocations during the ageing process and these form new atmospheres of interstitials anchoring the dislocations. These new interstitials are too small to be examined by energy-dispersive X-ray (EDX) methods, so TEM is more suitable. It has been found that the activation energy for the return of the yield point on ageing is similar to that for diffusion of nitrogen and carbon in alpha iron [5, 54, 55, 64, 65].

It is widely accepted that this leads to discontinuous plastic flow in solution hardened alloys. Yoon [66] noted that dynamic strain ageing occurs at certain test temperatures and strain rates; this combined condition revealed serrated flow within the uniaxial stress-strain curve.

Under these specific conditions an increase of strength and a decrease of ductility can be easily detected. Fig. 2.13 shows the temperature effect on flow curves of A533B steel at a constant rate, revealing the existence of dynamic strain ageing. Other studies have investigated the strain ageing process in low alloy ferritic steels, such as MnMoNi steels, including A533B plate and A508B forging types, it has been reported that there is an appreciable loss of fracture toughness of A533B RPV steel at elevated temperatures, this is a result of strain ageing.

Dynamic strain ageing occurs within metals containing interstitial solute atoms, (e.g. nitrogen). Such atoms interact with dislocations, increase work hardening rates, flow stress and ultimate tensile strength (UTS). There is also an increase in the ductile-to-brittle transition (DBTT), ductility decreases in terms of elongation, there are reductions in area, fracture toughness, strain rate sensitivity coefficient and upper shelf energy. Research into C-Mn steels carried out by Kim and Wagner [61-63, 67, 68] both observed that carbon and nitrogen were the main interstitial species. It was also noted that the nitrogen content had a greater influence than carbon on strain ageing of the material. The addition of interstitial impurities, such as carbon and nitrogen, lead to the yield-point phenomenon in ferritic steels. In turn serrated stress-strain curves (dynamic strain ageing, DSA) are observed. Sachdev [53] studied DSA in various steels, concluding that high strength low-alloy and dual phase steels show a smaller decrease in uniform elongation compared to plain carbon steels. Researchers also observed the critical temperature for the appearance and disappearance of serrate flow was dependant on the strain rate applied. The temperature and strain rate at which serration occurs depends on the concentration of carbon and nitrogen. Kim [67-69] used SA508-Class 3 material and noted that there was a decrease in the fracture toughness in the upper shelf region. This was due to the interaction between the carbon and nitrogen impurities with dislocations being generated in the well-developed plastic zone ahead of the crack front. Nitrogen is more important than carbon in the role of strain ageing, because its of higher solubility and diffusion coefficient as well as producing less complete precipitation on slow cooling. Nitrogen also associated with fine precipitates, ~10nm or clustering located at dislocations within the ferrite grains. This known link between strain-ageing and nitrogen suggests the particles are nitrides or carbonitrides. These effect the Charpy-V impact

transition temperature by 50°C. Both cold working and strain ageing will increase the transition temperature, although strain ageing has a greater influence and increases it by 20 to 35°C. Patel [70] investigated the fracture behaviour of A533B using Charpy specimens across a range of temperatures and deformation rates using three-point bend tests, Fig. 2.14 shows the effect of dynamic strain ageing, resulting in large “raises and falls” in fracture energy at the upper shelf.

Little [32] at AERE (UK) researched strain ageing combined with the effects of temperature (277°C) neutron irradiation ($\sim 3 \times 10^{23}$ neutrons/m²) on the properties measured using Charpy impact values on commercial RPV steels (of the type A533B). It was observed that neutron irradiation suppressed ductile-to-brittle transition shifts associated with nitrogen strain ageing, demonstrating that the effects of radiation need not to be cumulative. Similar conclusions were reached by Murty, Little and Harries and Jung and Murty [30, 34, 48, 49]. At temperatures below 300°C the effects of the interstitial elements are dominant, being dependant on deformation conditions, (e.g. loading and strain rate). These forces can be significant during pressurised thermal shock, as interactions of impurities such as copper become important at operating conditions for the reactor. Little [49] also investigated the radiation hardening processes that occur in phosphorus and copper doped A533B alloys. Using small angle neutron scattering technique (SANS), the presence of copper was found and gave rise to the creation of scattering centres <1nm in diameter, the volume increasing with increased levels of copper, with the addition of nickel further enhancing these precipitates. Chakravarthy [55] researched dynamic strain ageing in A203D steel, noting that the DSA led to serrate stress-strain curves for both martensite and ferrite-pearlite structures, both the characteristics and activation energy for the onset of serrations were identical in both microstructures. It was also commented on that the microstructure has negligible effect on DSA when the effect of irradiation is taken into account, thus control of the chemistry may be the only way to reduce the effects of DSA on the mechanical properties and behaviour.

2.5.1 Interactions Between Solute Atoms and Dislocations

Interstitial solid solutions commonly comprise of the elements carbon and nitrogen, although interstitials containing one or more of oxygen, nitrogen and boron are known to exist. These interstitials are also commonly associated with the formation of yield-point, thus it is important to discuss the interaction between solute atoms and dislocations. Solute atoms can interact with dislocation via the following mechanisms [40]; modulus interaction; elastic interaction; short-range order interaction and stacking faults interaction. A modulus interaction occurs if a solute atom locally changes the modulus of the crystal. Elastic interaction between solute atoms and dislocations arise from the mutual inaction of elastic stress fields surrounding the core edge of the dislocation and misfitting solute atoms. Stacking-fault interactions happen because solute atoms preferentially segregate to stacking faults contained in extended dislocations. Short-range order interactions arise because the solute atoms tend to arrange themselves so that they have more than the equilibrium number of dissimilar neighbours.

2.6 Carbon-Manganese Welds

2.6.1 Fusion Welding

The history of joining metals stretches back over several thousands of years. Some of the earliest examples come from the Bronze Age and are small gold circular boxes which were made by pressure welding lap joints together. It was during the Middle Ages that the Egyptians learnt to weld pieces of iron together [71]. It was throughout this time the art of blacksmithing was developed in the west and many items of iron were produced which were welded together by hammering the joints together to form a bond and this is considered a solid-phase process. Forge and hammer welding was used on a limited scale up until the 1930's for the manufacture of aluminium and steel vessels from plate up until the 1930's, however this process was costly and required great skill.

To overcome this problem, fusion welding was applied, in which a heat source intense enough to melt the edges of the material is traversed along the joint. At the end of the 19th century intense heat sources became available on an industrial scale, where arc welding, gas welding and resistance processes all made their appearance [71]. The most important fusion process is arc welding with a fusible electrode, which is a complex process and consequently slower to develop than the relatively simple gas welding process. Initially, the end results of welding were very brittle due to high nitrogen content. To avoid this embrittlement mechanism electrodes were wrapped with different substances, such as paper or asbestos, more recently, however, with the development of modern arc welding electrodes, these are coated with a mixture of ferro-alloys, minerals and in some cases organic materials, bonded with sodium or potassium silicate.

In modern times the use of fusion welding has increased rapidly and is widely used for many applications from ship building, petroleum, chemical and steam power plants, e.g. reactor pressure vessels, as well as for bonding of structural steel work. Welding has become widespread and replaced riveting for the majority of fabrication processes [71, 72]. As a consequence there is an incentive to develop alloys, electrodes, and other consumers, that retain desirable characteristics and are also readily weldable. Examples of alloys that have been developed for improved weldability are low alloy steel, titanium-stabilised austenitic stainless steel and phosphorous-deoxidised copper. Welding has come to influence not only fabrication but metals technology as a whole.

2.6.2 Submerged Arc Welding (SAW)

Submerged arc welding (SAW) is the fusion welding process used to produce the weld metal samples investigated in this thesis and therefore will be described in some detail. The SAW process is based on an arc formed between a bare wire electrode that is continuously fed onto parent plate material. The filler wire is melted to fill the joint gap between the two edges or

surfaces. The arc, electrode end and the molten pool operate under a layer of granulated flux and they are termed “submerged” Fig. 2.15. The electrode is constantly shielded by a layer of molten flux which is a layer on un-fused flux in a granular state, therefore there is no visible evidence of current between the electrode and the workpiece during the welding process, and as a consequence the weld is produced with none of the sparks, spatter, smoke or flash commonly observed in other welding processes. The SAW process is commonly used for fusion welding joints of carbon, low-alloy and high-alloy steels and copper alloys. The filler wire in the SAW process is fed from a reel and therefore can be used for automatic welding of large structures that need a continuous welded joint such as pressure vessels, boilers and horizontal joints in storage tanks. However, it is limited as the flux is fed from a hopper that relies on gravity and therefore can not be used to weld vertical structures [14].

Some of the granulated flux melts under the heat of the arc, adding alloying elements to the weld pool. Slag forms as a layer that protects the weld from contamination and oxidation from the atmosphere. A flux is fed from a container which is attached to the welding head through the front of the arc. The electrode is fed into the arc by a servo-controlled motor, this matches the speed of the electrode feed to the speed at which the electrode is melting, meaning that the arc is kept at a constant length, shown in Fig. 2.15. During the submerged-arc welding process, the flux completely covers the arc and this covering increases the thermal efficiency of the welding to approximately 60% compared to conventional manual metal arc welding which is about 25% efficient. Submerged-arc welding can use both Direct Current (DC) and Alternating Current (AC) as a power source, Fig. 2.16 shows the SAW process using AC or DC current. The output voltage can range from 3-35V and the electrode wire generally acts as the anode. Depending on the electrode wire diameter, the current can be varied from 200-1600A, although in practice a current of 600-900A is used [71]. For DC operation, the electrode is normally connected to the positive terminal. Electrode negative (DCEN) polarity can be applied to increase the rate of deposition, though with this technique the penetration depth is reduced by 20-25% [71]. DCEN is applied to surface applications, where the dilution of the parent metal is important. Direct Current has a constant voltage output, which produces a self-regulating arc. AC power sources have a constant current output, therefore they are not self-regulating. The arc must be controlled by sensing the arc

voltage and using a signal to control the speed of the wire feed. The SAW process can be applied by two techniques; manual and mechanised. Due to the high rate of deposition, mechanised submerged-arc welding is generally applied in most cases. A number of methods are used to move the welding head at a controlled speed along the length of the weld line, these include; an electrically-driven tractor unit, a motorised drive that transverse along the horizontal beam and a hand operated trolley. In the case of circumferential joints, the welding head is fixed and the work piece is rotated beneath it.

Submerged-arc welding uses relatively high welding currents. Hence, there are high rates of deposition and therefore high productivity can be obtained. SAW is versatile and especially appropriate for longitudinal and circumferential welded joints. There are virtually no restrictions to the thickness of materials that it can be applied to as multi-passes can be used. Another advantage with the SAW process is that it can be applied to the most materials including; C-Mn steels, low-alloy steels and stainless steels, with typical applications in pressure vessels, ships, bridges and large structures [73, 74].

Generally, a single wire is used for the SAW process for either DC or AC current. Twin or triple wire variants can be applied to increase the deposition rate of weld metal and/ or travel speeds. There is a large variety of wire with varying compositions and a range in diameters from 0.8-6 mm. The wire electrode tends to be copper coated: this ensures a good electrical contact between the work piece and the power source [71]. Fig. 2.17 shows the larger the wire diameter and the higher the welding current, more weld metal that can be deposited. The main role of the flux in the SAW process is to protect the weld pool and the arc from the atmosphere. It also cleans the surface of the pool and can influence the surface profile of the weld. Fluxes used in the SAW process are made up of granular minerals, which contain oxides of manganese, titanium, calcium, silicon and aluminium. The fluxes are in two classifications, according to the manufacturing process, agglomerated (bonded) and fused. Agglomerated fluxes are manufactured by bonding the dried ingredients with low-melting components, for example sodium silicate. Fused fluxes are manufactured by mixing and melting the ingredients, then casting them to form solid glassy particles. These are then

ground to the required particle size [75]. Fused fluxes produce a stable arc and easily removable slag, whereas agglomerated fluxes produce slag which is difficult to remove, and the welded surface is not as smooth as it is with fused fluxes. Agglomerated fluxes are both alloying and deoxidising. The constituents are not affected in the melting process, as this generally takes place at lower temperature. Fused fluxes formed at higher temperatures have difficulty in retaining the deoxidising and alloying elements [71].

The choice of welding parameters, such as current, heat input, travel speed, pre and post-heat inputs along with flux and filler wire will all affect the weld pool solidification. This in turn will affect the weld geometry, the weld microstructure, the size of the weld beads, the number of passes necessary to fulfil the joint gap and finally the heat affected zone (HAZ) of the weld. The HAZ is the region surrounding the weld pool whose temperature is not sufficient to cause melting; however some solid state transformations may occur, such as, precipitate dissolution; coarsening grain growth; and alpha to gamma ($\alpha \rightarrow \gamma$) phase transformation.

2.6.3 Effects of welding process variables on C-Mn metal microstructures.

Weld metal microstructure is primarily controlled by two factors; the weld metal composition and cooling rate. The heat input controls the cooling rate and the rate weld pool heat liberation which is a function of base plate thickness, extent of preheat and weld joint geometry. Other influencing factors are interpass temperature, flux and heat input rate [75].

2.6.3.1 Heat Input Rate

One of the most important variables in fusion welding is the heat input rate, as this influences cooling rates, heating rates and weld pool size. As a general rule, the higher the heat input rate the slower the cooling rate and larger weld pool. It also controls the grain size in the AD

and the HAZ of the weld metal. Previous research [71, 73, 74] has shown that there is an inverse relationship between the cooling rate and the size of weld pool. This is an important relationship in the welding of steel since increased cooling rates increases the risk of hydrogen-induced cracking [76].

Previous research has shown that a high input rate process like SAW has less HAZ cracking in the welding of alloy steel, than manual metal arc welding, where the heat inputs are lower (n.b. there might be other variables that contribute to the difference in behaviour). As a result this leads to coarsening of the prior austenitic grain size and also a general coarsening of the as-deposited (AD) microstructure of the weld [14, 15], as well as a decrease in the degree of acicularity was observed. Slower cooling rates produce a decrease in such constituents as acicular ferrite as well as an increase in the volume fraction of the allotriomorphic ferrite at the expense of the acicular ferrite. Acicular ferrite volume fraction might be improved by an increase in the inclusion population density. Thus, as a result the weld pool remains molten for longer allowing manganese and silicon (key constituents for the formation of inclusions) to evaporate and allowing formed inclusions to diffuse into the slag. Also the way in which the heat input is introduced is important, if it is increased by raising the arc current, the width/depth ratio of the weld pool decreases, thus giving a shorter cooling time, even though the heat input is increasing.

2.6.3.2 Flux

Flux is a coarse granular powder, made of minerals, that is dispensed onto the workpiece immediately ahead of the arc; the main role of the flux in the SAW process is to protect the weld pool and the arc from the atmosphere. As well as cleaning the surface of the weld pool it can also influence the surface profile of the weld. The granular flux can be chemically basic, natural or acid. Fluxes generally basically fall into two classifications, according to how they manufactured by bonding the dried ingredients with low-melting components, for example MnO with SiO², or CaO with SiO² [72]. Fused fluxes are manufactured by mixing and melting the ingredients, then casting them to form solid glassy particles, and then ground

to the required particle size. Fused fluxes produce a stable arc and easily removable slag layer, whereas agglomerated fluxes produce slag, which is difficult to remove, and the welded surface is not as smooth, as it is with fused fluxes. Agglomerated fluxes are both alloying and deoxidising, the constituents are not affected in the melting process, as this generally takes place at lower temperature. Fused fluxes formed at higher temperatures have difficulty in retaining the deoxidising and alloying elements.

As the flux melts around the arc it forms a pool, which solidifies and reforms periodically, dependent on the movement of the welding torch. Metal may be transferred directly across the slag cavity so formed or occasionally around the edge of molten flux. The gases generated during the SAW process by vaporisation and chemical reaction at the electrode tip are also protective along with the flux, of the molten metal. The slag which is formed during the welding process protects the weld from the atmosphere and in particular from the absorption of moisture. Other compounds added in small quantities control the viscosity and help the flow of liquid filler metal into the weld pool.

2.6.3.3 Interpass Temperature

Whilst keeping other welding parameters constant, an increase in the interpass temperature will reduce the cooling rate. Evans [77] observed the following effects of increasing the interpass temperature; slight reduction in the amount of manganese and silicon; increased width of the recrystallised zones; coarsening of the AD weld metal region and a reduction of the volume fraction of the acicular ferrite phase.

2.6.3.4 Postweld Heat Treatment (PWHT)

Postweld heat treatment (PWHT) within the subcritical range has the influence of reducing both the hardness and strength of an alloy-steel weld deposit. In thickness over

approximately 30 mm, PWHT increases both the ductility and the fracture toughness of the welded joint, as a whole. It has been noted, in some cases, for Charpy impact and crack tip opening displacement (CTOD) values for the weld metals increase by PWHT, although there are certain circumstances where they might be reduced. To accurately determine the effect of PWHT, welding procedure testpieces must be subjected to the same thermal conditioning as that used in production.

2.6.4 Non-Metallic Inclusion Formation

Inclusion formation is the first development to occur on cooling of the liquid weld metal, this development will affect the final microstructure of the weld metal. Inclusions commonly arise from two sources: by entrapment of welding slag (exogenous); or by indigenous inclusions as a result of oxidation reactions (oxides) or solid state precipitation reactions (carbides, nitrides and sulphides) Fig. 2.18. Oxides normally begin to form at around 2026°C (2300K) while the weld pool is still molten. Oxides will influence the final weld microstructure in terms of their composition, size, spatial distribution and volume fraction, as well as influence other phases such as acicular ferrite, which is known to be nucleated by inclusions. The former group is usually observed to be heterogeneous in nature, with respect to shape (angular or spherical), chemistry (multiphase particles) and crystallographic properties resulting from the complex alloying systems that are involved, with the exception of C-Mn and low-alloy steel welds, as the oxide inclusions are predominately spherical, glassy, and manganese silicates, a survey of important weld metal inclusion characteristics is shown in Table 2.1 [78, 79].

Inclusion formation comprises of various distinct stages such as nucleation, coarsening and coalescence (as well as elimination from the weld to slag). Diffusion-controlled deoxidation is a characteristic of arc welding and complete within a fraction of a second in small volume, in which temperature gradients in the order of 1000°Cmm⁻¹ [80] with cooling rates for 1000°Cs⁻¹, for nuclei in the order of 10⁷mm³ or higher. In the weld pool the main source of oxygen is caused by the flux, the weld pool also contains reduced oxides like silica, iron oxide

and manganese oxide. Oxygen in the weld pool may be removed by deoxidizing elements through chemical reactions, thus inclusions are formed. In low-alloy steel weld metals, oxygen combines with various trace elements to form stable oxides in the order: Al^2O^3 , Ti^2O , SiO^2 , MnO , TiN and MnS , Fig. 2.19, as proposed by Bailey and Pargeter [81], although work by Hseith [82] has suggested the exact sequence is dependent on the weld composition. The growth of the inclusion is influenced by this sequence of stability and thus inclusions are found to have a core and a layered structure, Fig. 2.19, it has been observed in most weld metal inclusions that the core of the inclusions is an oxide such as Al^2O^3 and or TiO . The outer layer has acted as a nucleation point for microstructure formation around the inclusion, generally this is TiN and/ MnS . TiO is considered the most important for the nucleation of acicular ferrite. However, it should be noted that the free energy for formation of oxides depends on concentrations of deoxidising elements and oxygen, also the sequence of oxidation is different for welding conditions and different chemistry [83].

Oxidation reactions rapidly proceed by growth of nuclei larger than the critical size. The growth of these nuclei occurs by diffusion of the relevant reactants in the melt, and it can also be enhanced by collision and coalescence of inclusions. Coalescence is considered to be important for small nano-sized inclusions as the process takes place in a fraction of a second. Deoxidation products are trapped in the weld metal by the advancing solid and form what is termed as the oxide population. However not all the oxides formed are trapped inside the solid as the liquid cools, as some inclusions densities are lower than that of liquid iron. Work by Sudgen and Bhadshia [84] showed that inclusions are not randomly distributed but larger inclusions caught in the growing of the solid-liquid interface and pushed along by the “Margangani effect” (repulsive effect of interfacial tension between the inclusion interface and the liquid). Hence large inclusions are commonly preferentially distributed on the grain boundaries of δ ferrite, which is often the first phase to form. It should be emphasised that inclusions are not aligned with prior austenite grain boundaries [85]. Smaller inclusions are relatively unaffected by the solid interface and become trapped within the delta grains. Research by Nakonishi [86] showed that a reduction in the average inclusion size and the number of large inclusions influenced the Charpy toughness at low temperatures.

2.6.5 Weld Pool Solidification

Solidification behaviour of the weld pool distinctly differs from that of ingot solidification due to the presence of partially melted base metal grains at the fusion boundary. Heterogeneous nucleation of new grains occurs and grows into the weld pool, in the direction of maximum thermal gradient (the heat flow direction). This process is known as epitaxial solidification and shown in Fig. 2.20. Davis and Garland [87] summarized a number of basic differences:

- Weld solidification is orders of magnitude greater than that found in ingot solidification, thus leading to steep thermal gradients within the weld pool;
- in weld-metals the microscopic shape of the liquid/ solid interface remains constant over large portions of the weld length, whilst changes are progressive within an ingot;
- to initiate weld pool solidification no nucleation event is necessary, since the solidification interface is already present;
- electromagnetic stirring by an electric arc and the characteristics of the fusion welding process causes greater motion of the molten metal within the weld pool, compared to the molten metal experienced within a solidifying ingot.

Grain growth is of a cellular nature producing columnar grains which are similar in size to the base material from which they are originating. Fig. 2.21 shows cellular substructure which is characteristic of columnar grains [88, 89]. During the welding procedure dilution of the base material is inevitable. The initial size of the weld columnar grains is directly related to the grain growth zone adjacent to the fusion boundary, whereas the solidification microstructure depends on the grain coarsening behaviour of the base material. In high energy welding process such as submerged arc welding and gas shielded welding, this is considered a problem as grain growth from the base material can be considerable, thus columnar grains at the fusion boundary may be correspondingly coarse [89]. In practice though these problems can be overcome and eliminated by additions of inoculants from the filler wire, which helps to

assist the refinement of columnar grain structure through the heterogeneous nucleation of new (equiaxed) grains ahead of the advancing interface [78].

Within metals these grains have preferred directions of growth, known as “easy growth directions”. In cubic metals these are in the $\langle 100 \rangle$ direction [13, 14]. This is believed to be the preferential growth direction as it is the least close packed alloy and therefore has a faster growing rate than in other directions (close packed) during the crystallization process from the random atomic arrangement in the liquid. The speed of welding and the shape of the weld pool also influence the shape and size of the columnar grains. Faster welding leads to a tear shaped weld pool, with maximum thermal gradient relatively invariant from the fusion line to the centreline of the bead, and consequently a different columnar grain morphology, Fig. 2.22. Weld pool geometry can be characterised by dimensionless operating parameter, n^3 :

$$n_3 = \frac{q_0 v}{4\pi a^2 (H_m - H_0)} \dots (2.4)$$

where q_0 is the arc power;

v is welding speed;

a is thermal diffusivity of base plate

$(H_m - H_0)$ is heat content per unit volume at melting point.

However it should be pointed out that thermal properties of the base material (e.g. a and $(H_m - H_0)$) are important when defining the weld pool shape. As a result tear-shaped weld pools are normally observed in weldments with a low thermal conductivity (e.g. austenitic stainless steel), whereas spherical or elliptical weld pool is more likely to form during aluminium welding, because of the base material having a higher thermal conductivity. The weld pool is

also affected by convective heat transfer due to the presence of buoyancy, surface or electromagnetic tension gradient forces [78].

Weld microstructures are affected by the initial solidification phase rather than austenite or δ -ferrite for the two following reasons [13]:

- austenite and δ -ferrite has different solute partition coefficients. Also the diffusivity of elements in δ -ferrite is greater than that of austenite. Diffusivity of the solute in the solid decreases, redistribution becomes more restricted, thus increasing the degree of segregation [90, 91].
- non-metallic inclusions tend to segregate to grain boundaries of the phase which is the first to solidify [84]. If δ -ferrite is the first, the inclusions will, after the $\delta \rightarrow \gamma$ transformation be found in γ grains where they contribute to acicular ferrite formation. If austenite is the primary solidification phase, there would be a non-uniform distribution of large inclusions at the austenite grain boundaries (e.g. in allotriomorphic ferrite after the $\gamma \rightarrow \alpha$ transformation), thus reducing the amount of beneficial acicular ferrite phases, also serving as a potential site for initiation of cleavage [13, 14, 28, 29].

2.6.6 Transformations and Microstructural Development

Carbon and low alloy steels transform to austenite at a temperature not far from the solidification point and finally to ferrite regardless of the first phase to form within the microstructure. The equilibrium structure of iron-carbon alloys is shown in Fig. 2.23(a) and Fig. 2.23(b) shows a detailed region of the Fe-Fe₃C system [92]. Steel is austenitic when the temperature falls within the region of γ . Under slow cooling the austenite phase starts to transform when the temperature falls to a point on the lower boundary of this region relating to the amount of carbon in the steel—the upper critical temperature. Ferrite containing a small

amount of carbon in solid solution is precipitated, leaving austenite grains that become smaller and are progressively enriched in carbon as the temperature falls. At 723°C, the lower critical temperature, residual austenite, containing approximately 0.8% carbon transforms in pearlite—a laminated eutectoid mixture consisting of both ferrite and cementite (Fe₃C). The structure is obtained by slow cooling and consists of intermingled grains of ferrite and pearlite. Cementite can decompose to iron and graphite if held for long periods at elevated temperatures. The Fe-Fe₃C phase diagram is shown in Fig. 2.23a is considered metastable [71].

The temperature is depressed upon rapid cooling, this affects the γ to α change, and when this takes place. The distance carbon atoms can diffuse is reduced as the transformation temperature falls; there is a tendency to form structures involving progressively shorter movements of the atoms. However on slow cooling carbon segregates into individual austenite grains, with further rapid cooling carbides precipitate within and around ferrite, now with the appearance of fine needles or plates rather than just equiaxed grains. This structure is known as bainite, Fig. 2.24 [93]. Upon further and more rapid cooling, the temperature is further depressed and martensite is formed. Martensite is a product produced by shear movement of the austenite lattice; carbon is retained in solid solution in a distorted body-centred lattice. In general this transformation product is more hard and more brittle the lower the transformation temperature, and the higher the carbon content, especially in the case of martensite [71].

As previously discussed, as the shear rate decreases the cooling rate in the fusion welding increases thus the speed of welding also increases. It is higher for multi-pass welding in thicker plate than for single pass welding in thin plate, with other parameters being equal, it is reduced by increasing the preheat temperature. The weld metal and the associated HAZ form under continuous cooling conditions.

Continuous cooling transformation (CCT) diagrams can be used to analyse the effect of cooling rates of microstructure on steel weld deposits. CCT diagrams for weld metals have been presented by several authors, with an increase in cooling rates leading to a progressive decrease in the transformation-start temperature. As a consequence products forming at higher temperatures will be suppressed for those forming at a lower temperature. Experimental CCT diagrams were determined by Ito [94, 95] for welds at different oxygen contents, showing a shift to the left for higher oxygen content. It was also noted that the temperature at which ferrite forms was higher for a high oxygen weld content, this would increase the difference between the start temperatures for acicular and allotriomorphic ferrite, allowing more time for the growth of allotriomorphic ferrite and thus increasing the volume fraction of the weld. The apparent decrease in hardenability with increased oxygen content is explained with respect to the $\gamma \rightarrow \alpha$ transition temperature. Although Farrar and Watson [96] offered an alternative solution for the decrease in the hardenability with increased oxygen, it was suggested that oxygen combines with alloying elements present within the weld to form inclusions, and this depletes the weld of alloying elements, e.g. manganese and silicon and these reduce the weld hardenability.

An example of a continuous cooling transformation diagram, CCT, is shown in Fig. 2.25. Increasing the cooling rate leads to a decrease in the transformation-start temperature. As a result these products, which form at a higher temperature (such as allotriomorphic or primary ferrite) will be surpassed while those that form at a lower temperature (such as bainite and martensite) will be promoted. However other features that can be observed in the microstructure of a weld are discussed below [97].

2.6.7 Weld Microstructures and Nomenclature and Development

2.6.7.1 δ -Ferrite to Austenite Transformation

During solidification low-alloy steels undergo numerous multi-phase transformations and subsequent cooling. Dependant on the cooling rate, carbon or substitutional alloy content, the primary solidification product will be either austenite, γ , delta ferrite, δ or a mixture of both.

Delta ferrite will be the first phase to form when a low-alloy steel weld metal is cooled slowly to below the crystallisation temperature [85]. As previously discussed in Chapter 2.6.3.4 delta ferrite grains reveal a anisotropic columnar morphology, with major axis in the direction of the steepest temperature gradient within the weld pool, generally with large inclusions delineating the grain boundaries [85]. As shown in Fig. 2.26, cooling below the peritectic temperature, austenite nucleates epitaxially at the primary delta ferrite grain boundaries, as these sites provide the lowest energy barrier for heterogeneous nucleation. At elevated temperatures, once nucleated γ grains grow quickly by diffusion of carbon into the austenite, and this has been well documented for γ -Widmännstätten sideplates growth within duplex stainless steels, Fig. 2.27. If we consider the primary precipitation of δ ferrite, austenite cannot grow across primary delta ferrite solidification boundaries, because austenite is bound by an orientation relationship with delta ferrite, Fig. 2.28 and Fig. 2.29 [87-89, 98-102].

Nevertheless, in certain low-alloy steel weld metals, austenite grain boundaries will cross the original delta ferrite solidification boundaries due to the shift in the mechanism of the peritectic transformation, shown in Fig. 2.26 and Fig. 2.30 it can be seen there is no matching between the two types of boundaries in this case [84, 87, 89, 103-105]. It was observed that the shift in mechanisms of peritectic transformation can be linked to heterogeneous nucleation of austenite at inclusions (e.g. Al_2O_3), this is more energetically favourable than nucleation at δ/δ grain boundaries [78], it can be suggested that there is more than one nucleation event pre δ -ferrite grain size and the nucleation rate is high. It has also been shown that the columnar structure of γ grain boundaries do not match with the original δ -ferrite boundaries [106]. It

can be seen under these conditions that the austenite is not bound by orientation with the delta ferrite and can grow freely across the original delta ferrite columnar grain boundaries shown in Fig. 2.31, therefore austenite grains will adopt a morphology different from columnar grains [105, 107].

2.6.7.2 Austenite Decomposition

Microstructural changes take place during the welding process, both within the fusion boundary region and the HAZ, in turn this affects the mechanical integrity of the weldment. Microstructural solid state transformations of steel weld deposits are characterised by the volume fraction of non-metallic inclusions, which are considerably higher than those in normal cast steel products and strong non-isothermal localised behaviour. For instance in the HAZ, carbides and nitrides coarsen and dissolve, growth occurs to an extent that depends on the distance from the fusion boundary and the exposure time defined in the welding procedure. Hence, this may have a significant affect on the subsequent microstructure and properties of the weld region by the CCT curve being displaced by longer times, thereby producing more Widmännstätten ferrite, or increasing the possibility of martensitic and bainitic transformations on cooling [71, 73, 74]. As a consequence of these by-products the toughness of the weld may be reduced and there may also be an increased risk of hydrogen cracking [71].

Upon final solidification, the microstructure of the weld alloys usually consists of columnar delta ferrite grains with larger inclusions delineating the grain boundaries. This is occurring at approximately 1500°C, as cooling continues to 1300°C the delta ferrite transforms into austenite, otherwise known as γ delta ferrite. It has been shown that prior δ grain boundaries did not correspond with the new formed γ grain boundaries as a result of this transformation, also more than one γ grain could nucleate per delta ferrite grain. Following nucleation rapid grain growth by diffusion along the prior delta grain boundaries occurs until the whole microstructure is γ grains. Austenite goes through further decomposition as a result of further cooling, starting at ~1000-750°C Fig. 2.28 and 2.29.

As the transformation between austenite to ferrite occurs, there are a large number of microstructures that can develop, by a mixture of displacive and diffusion mechanisms, shown in Fig. 2.28. These depending on the weld chemical composition and the cooling rate of the steel weld. The microstructure normally forming within a single austenite grain after transformation will be a complex mixture of two or more of the following, arranged in decreasing transformation temperatures [78]:

- I. Grain boundary (allotriomorphic) ferrite (α_{all});
- II. Polygonal (equiaxed) ferrite (PF);
- III. Widmånstatten ferrite (α_{W});
- IV. Acicular ferrite (α_{C});
- V. Upper bainite (α_{ub});
- VI. Lower bainite (α_{lb});
- VII. Martensite (α');
- VIII. M-A-C Martensite-austenite-carbide microphases retained on cooling from the γ phase.

Grain boundary α is the first phase to form during decomposition of the austenite. Various authors have reported different temperatures ranging from 1000-600°C for the start of this reaction, the reason for this discrepancy could be the effect of composition of the weld metal, e.g., alloying elements such as manganese, which will lower the temperature at which the transition takes places, as this is an austenite stabiliser. Grain boundary α nucleates and grows along the prior γ grain boundaries via a reconstructive diffusional process (iron atoms diffuse to minimise lattice strain) [108]. Growth is occurring by the progression of planar incoherent γ/α interface. Growth of α_{all} continues until all the grain boundaries are consumed and growth perpendicular to the grain boundary must occur. Due to the diffusion of iron atoms as well as carbon, the mechanism of α growth, as a result of undercooling becomes kinetically unfavourable. At temperatures below 650-600°C the diffusion of iron becomes slow and Widmånstatten ferrite (α_{W}) begins to grow, the morphology of this is of parallel

plates which have nucleated on either the prior γ grain boundaries or on the α_{all} ferrite. These plates have grown via a displacive process whereby iron atoms no longer diffuse [109, 110]. The wedge shaped plate allow for a more efficient method for carbon rejection into austenite retained between the plates due to multi-directional diffusion compared to the planar diffusion of α_{all} . The side plate edge consists of small low energy ledges with a Kudjmov-Sachs orientation relationship [111]:

$$\gamma_{FE}\{111\} // \alpha_{FE}\{110\} \text{ and } \gamma_{FE}\langle 110 \rangle // \alpha_{FE}\langle 111 \rangle \quad \dots (2.5)$$

Carbon is rejected at the interface of α/γ and leads to regions enriched by γ phase, these can be retained at room temperature forming a M-A-C constituent or it can be partially transformed to martensite. Eventually undercooling is such that α_{w} becomes kinetically unfavourable and the remaining austenite phase is transformed into the acicular ferrite, bainite, or in extreme cases of undercooling; martensite. Research is still being carried out into the formation of acicular ferrite, and arguments remain over the formation and exact nature of this phase [112]. There is however general agreement that it is a fine form of Widmännstätten ferrite or a form of bainite, it is also agreed that in both cases it forms intergranularly on inclusions. The morphologies of bainite and acicular ferrite and similar occur via a displacive reaction with carbon diffusion as is the case with α_{w} whilst martensite is purely a displacive transformation. α_{c} , α_{w} and α' form at a rapid rate, such that the final transformation occurs in less than a second. Therefore they are thought of as isothermal transformations, Fig. 2.27 [111]. Acicular ferrite is associated with the optimum welding mechanical properties [71, 79, 113], both in terms of strength and toughness, this is a result of the “basket-weave” morphology, characterised by high dislocation density and very small laths. Numerous studies [78, 103, 114-121] have been carried out in recent years, in low-alloy steel welds metals the acicular ferrite transformation is still subject to considerable controversy. It is widely accepted however that acicular ferrite is a very fine form of Widmännstätten ferrite or a form of bainite. It is also well established that acicular ferrite nucleates in the transformation temperature range between Widmännstätten and lower bainite. The bainite and acicular ferrite morphologies are very similar and occur via a displacive

mechanism with carbon diffusion as for Widmånstatten [78, 122]. Several researchers [111, 114, 123-125] have suggested that the growth of acicular ferrite happens by pure shear transformation or a ledge mechanism similar to upper bainite in steel.

Microstructure quantification in steel welds is most commonly carried out by using an optical microscope. Numerous systems [71] have been introduced for the classification of the various constituents of the microstructure; each of the systems reflects the investigators views and discretion in relations to the mechanisms of transformations rather than just the morphologies [13]. Abson and Dolby [121, 126] originally proposed a scheme for the classification and quantification of the weld microstructure, based on this the International Institute of Welding (IIW) [104] have developed guidelines to aid this process. The IIW scheme involves a simplified classification procedure for the distinction between acicular ferrite and the different sideplate structures, based on features such as relative lath size, aspect ratio and number of parallel lathes. Difficulty has been noted in optically determining the difference between upper bainite and Widmånstatten ferrite, therefore the Welding Institute introduced a terminology which would encompass both phases, α_{FS} (ferrite with aligned second phase).

2.6.7.3 Microphases

As described and shown in Fig. 2.29, all ferrite transformations are accompanied by carbon diffusion thorough the remaining austenite (γ decomposition to α_{all} , α_C and α_W). Hence, carbon enriched austenite regions occur at the junction of equiaxed allotriomorphic ferrite grain, between acicular ferrite and Widmånstatten ferrite planes. For the duration of cooling these regions of enriched austenite may transform to bainite, carbides, martensite or remain as austenite [22, 106, 108, 109, 118, 119]. Without the use of TEM it is difficult to define these phases, thus they are generally known as “microphases”. Formation of microphases may be associated with disproportionate hardenability in alloys which have insufficient time to form ferrite phases, resulting in bainite and/ or martensite formation. With large amounts of γ phase stabilisers added, austenite can then be retained at room temperature. Low heat input

during the welding process can also assist the development of microphases, consequently this results in fast rates of cooling, leading to the formation of bainite and/ or martensite [122, 127]. Also if the inclusion size and distribution are insufficient, and/ or of an incorrect type, the nucleation of ferrite becomes much more difficult and this means more γ phase is available for transformation to bainite and or martensite. Measuring the microphase fraction accurately is difficult, thus it tends to be included in the volume fraction of acicular and Widmännstätten ferrite.

2.6.7.4 Effect of Alloying Elements on Weld Microstructures

The microstructures of the weld deposits are influenced by additional alloying elements increasing hardenability by inhibiting the transformation of allotriomorphic ferrite, and by controlling the oxygen content. This affects composition and distribution of non-metallic inclusions. For notch impact toughness specimens both coarse grain ferrite and lamellar structures are undesirable, whereas high levels of acicular ferrite are associated with good notch ductility of the fuse zone in low-alloy steel welds. Hence, there has been a considerable amount of research and work investigating the optimum chemical composition levels and welding parameters to promote the formation of a beneficial factor. Due to multiple interacting factors involved during the cooling process, it is difficult to address this influencing element directly [22].

The effect of alloying combinations on toughness and strength of weld deposits has been studied in great detail. It is widely known that the addition of large amounts of carbon can strongly effect the hardenability of steel, [84, 98, 99, 114, 128, 129] thus the levels of carbon are kept low and within a narrow range, usually 0.05-0.12wt%. This level of carbon produces the best combination for fracture toughness and cracking resistance. Increasing the carbon content of the weld metal increases strength and hardness, it may also reduce the upper-shelf energy level. For the AD microstructure carbon influences the microstructure by increasing amount of acicular ferrite at the expense of allotriomorphic ferrite. Within the RH regions

carbon causes grain refinement and increases the amount of second phase particles within the fine grained reheated regions [130-135].

Manganese is probably the most important element after carbon that is commonly used to increase hardness and the strength of the steel and therefore they complement each other. Manganese also reduces the solubility of sulphur in austenite and particularly at high cooling rates; manganese promotes the formation of spherical rather than angular intergranular precipitates. An added benefit is the ability of manganese to reduce embrittlement due to overheating. Manganese is also known to lower the transformation temperature of austenite to ferrite; this inhibits the formation of allotriomorphic ferrite, thus leading to an increase in the proportions of acicular ferrite, in addition to refining both fine-grained and coarse-grained ferrite in the reheated region. Evans [132, 136] found the optimum impact toughness properties were achieved with alloying combinations of 0.07wt%C and 1.4wt%Mn, the reason for the decrease toughness of high alloy content welds was associated with an increase in yield strength. However, research carried out by Svensson and Grefot [129] disagreed with Evans findings, and remarked that increasing yield strength in high alloy steel metals does not decrease impact toughness of the material, because the increase can be related to fineness of the grains, which may actually improve the impact toughness. The positive effects of grain refinement by increasing alloying content can be offset by the formation of segregated bands of brittle microphases (bainite and / or martensite).

The flux used during the welding process transfers silicon into the weld pool, due to the large amounts of silicates and SiO_2 used as flux constituents. With increasing Si content the oxygen in the weld metal decreases while the amount of acicular ferrite increases. Evans [131] noted that for low Mn weld metals (0.6%wt.) increased Si content promotes acicular ferrite at the expense of both Widmännstätten and allotriomorphic ferrite. At high contents of Mn (1.4%wt), the volume fraction of acicular ferrite remains constant. Manganese, nickel and copper austenite stabilisers and believed to have similar effects on steel transformation behaviour, they also increase hardenability [105, 133]. Nickel, provides powerful solid solution hardening and high levels in the weld bead can result in changes of morphology

within microphases and acicular ferrite. Evans showed that increasing nickel content reduces the proportion of allotriomorphic ferrite and increases the amount within the AD regions. With manganese at high levels, nickel can also promote the transformation to martensite at the expense of acicular ferrite [78, 137].

In C-Mn weld metals molybdenum and chromium have similar effects. Within the AD region, increasing amounts of Mo initially increases the acicularity and reduces the volume fraction of the allotriomorphic ferrite. The volume ferrite of acicular ferrite was found to reach a maximum and the amount of the remaining microstructure, “ferrite aligned with second phase” increased both the molybdenum and chromium concentrations, this is a result of a decrease in the Widmännstatten ferrite as there is increasing Mo additions, and bainite replacing acicular ferrite. Kayali [138], noted that increasing Mo content from 0.24 to 0.48 wt.% generally increased the toughness of a submerged arc weld metal tested at low temperatures. This improvement was a result of a decrease in the fraction of M-A plus carbides, and an increase in the fraction of acicular ferrite. As previously discussed there is evidence, although circumstantial that titanium oxide (TiO and TiO^2) assist the formation of acicular ferrite, although the specific role of titanium has yet to be made clear. Research carried out by Evans [134, 139] found that 20ppm of Ti was enough to modify the microstructure from 80% Widmännstatten ferrite to almost 70% acicular ferrite, using the same welding conditions and parameters. Also with increasing Ti content refinement of ferrite grains and changes in the morphology of microphase was noted in the RH weld metal regions. Evans [131, 133] found the best values for Ti was 30 ppm, as toughness values are directly linked to the amount of acicular ferrite. Titanium has also been found to decrease the amount of soluble N content, it has been suggested that TiN particles insoluble in austenite provide intergranular nucleation sites during the austenite-ferrite formation [140]. Evans found that TiO may assist in the intragranular nucleation of ferrite by improving the size and distribution of inclusions. With TiN, TiO this has lower formation free energy than MnO and SiO^2 . If there was no titanium present within the weld pool, the inclusion composition would mainly be formed from manganese silicate, which form at low temperatures ($\approx 1350^\circ\text{C}$) thus leading to the formation of small inclusions with reduced nucleating potential. Nevertheless small amounts of Ti are added into the weld, TiO will form at much higher temperatures in the

liquid metal ($\approx 1800^\circ\text{C}$) and provide nucleation sites for other inclusion phases. This leads to the formation of precipitation and subsequent coalescence. Hence the capacity for acicular ferrite nucleation would be increased due to the formation of larger inclusions [78, 116, 117, 137, 139, 141].

To protect the weld metal from boron oxidation during transfer across the arc titanium is added, it also helps with the prevention of boron nitride formations. Boron is only effective in improving hardenability of the metal if it remains in solid solution in austenite and is known to be detrimental to toughness [22]. If it combines with nitrogen or carbon and forms nitrides or carbides in austenite grains, then a reduction in the hardenability occurs, as these particles induce the nucleation of ferrite. Aluminium may have the same effect as silicon and titanium on the inclusion population. Evans [134, 135] found that when adding aluminium and titanium together, the aluminium serves mainly to modify the role of titanium. A disadvantage of excessive aluminium is that it can tie up available oxygen and thus prevent titanium from forming oxides. Grong [142] showed the nucleation of acicular ferrite at titanium oxides and nitrides is more efficient than aluminium oxides (Al_2O_3 and MnAl_2O_3), this is due to the lower energy levels to nucleation of the former inclusion constituent phases. As a result there is a general reduction in the nucleation capacity of inclusions and a decrease in the oxide number density is associated with the precipitation of Al_2O_3 at high weld metal aluminium levels. Al_2O_3 has more affinity to oxygen than Ti_2O_3 , thus the optimum content of aluminium should be a function of the weld metal concentrations of silicon, titanium and oxygen [98].

2.6.8 Multi-pass Welds and Reheated Microstructure

Welding is a process that generates a surface heat source and produces a weld pool with a semicircular cross section. The size of the weld pool can be controlled in theory simply by changing the heat input rate. However, it may become more difficult to control the microstructure, i.e. the grain size may become larger than desirable and properties of the fused weld region as it becomes larger. Therefore in practice it is customary to reduce the size of

penetration of the weld bead size to approximately less than 20 mm and as a result of this larger joints have to be completed by multi-pass or a multi-run technique, where layers of weld passes are built up from the bottom to the top of the joint, Fig. 2.32 [71]. As subsequent layers are deposited, part of the previously deposited weld metal and HAZ will be reheated to temperature high enough to promote solid state transformations to austenite and then different microstructures upon cooling, whilst other regions may become slightly tempered. The weld metal will consist of two bead microstructures as-deposited (AD) and reheated (RH), Fig. 2.32(b).

Multi-run welding helps to increase notch ductility and decrease hardness, therefore proving beneficial. The tempered bead technique may take advantage of this, where the final capping run is made and then ground off, hence avoiding the problem of leaving the final run in the as-welding condition. The larger the number of weld beads, the greater the volume fraction RH weld metal that is produced. An advantageous benefit of this technique is annealing out of residual stresses caused by the previous runs, this provides certain preheat and tends to extend cooling times. Total heat input into the weld metal is decreased and this reduces grain coarsening [71].

Both peak temperature and cooling rate decrease the greater the distance away from the weld centreline, as a result the grain refined region may have distinctive microstructures, this depends on the maximum temperature level to which it has been subjected too. The RH region has three regions: intercritical, subcritical and supercritical regions.

The intercritical region is relatively narrow and partial transformation may take place, Fig. 2.32(c). Prior to welding carbon steels, which have a ferrite-pearlite microstructure, the eutectoid pearlite islands may transform to austenite on heating, and then on cooling to bainite or martensite. In the “as-welded” condition, this region may consist of hard grains which are embedded in an untransformed, relatively soft ferrite matrix. The subcritical region does not experience any observable microstructural changes, but strain-ageing is a possibility, this is

where the material has been strained and heated to a temperature range of 100 to 300°C, this is known as dynamic strain ageing.

The supercritical region has been reheated to a temperature such that full austenite transformation occurs; and this can then be subdivided into coarse and fine grained regions depending on temperature to which the reheating occurred. The fine grained region experience temperatures just above the $\alpha \rightarrow \gamma$ transition, thus resulting in small equiaxed ferrite grains, with restricted amounts of microphases inbetween, compared with the coarse grained ferrite which is located close to the fusion boundary where the peak temperature is sufficient to promote grain coarsening (grain recrystallisation and growth). It should be noted that large areas on austenite grain boundary (small prior austenite grains) mean that grain boundary ferrite easily nucleates and grows rapidly to consume the grains. This, in turn depresses the formation of the other constituents that normally occur at lower temperatures. Lath-like microstructures (e.g. high hardenability) and low transformation $\alpha \rightarrow \gamma$ temperature, during heating, results in a final RH microstructure which is more homogeneous, and similar to the AD microstructure, due partly to the fact that high hardenability allows enough time for the transformation of the re-austenitised region into a microstructure similar to the AD region. Several authors and previous research has noted that the RH region has higher toughness values than that of the AD microstructure in C-Mn and low-alloy ferritic steel welds; it is therefore desirable to increase the area of RH region at the expense of the AD area.

2.6.9 Previous work on the toughness of C-Mn weld metal

2.6.9.1 Introduction

Researchers have been interested in the toughness of C-Mn weld metal for many years, due to the widespread application of such welds in engineering structures. Frequently, the welds come under scrutiny, as they are often the regions of engineering structures where failure occurs or initiates.

2.6.9.2 Micromechanisms of cleavage fracture in C-Mn weld metals

The fracture micromechanism of C-Mn welds was investigated by Tweed and Knott [143], and found brittle fracture initiated from inclusions, unlike brittle fracture in wrought iron which generally initiates from carbides. Cleavage fracture initiation sites were located by tracing the river lines associated with the brittle fracture back across the fracture surface to their source. Research carried out by McRobie and Knott [52], Bose [22], Novovic [13] and do Patrocinio [15] have identified inclusions to be the cause of cleavage fracture with C-Mn welds. Investigations have been carried out to investigate if a crack inclusion, from which a sharp crack can propagate into the surrounding ferrite matrix was more detrimental to fracture toughness than a decohered inclusion from which the crack has blunted. Although after numerous results and analysis from both fracture toughness and blunt notched bend specimens no obvious difference were observed.

Tweed and Knott [7] carried out extensive hardness measurements of the constituents of α_{all} , α_W and α_C of the AD microstructure of a C-Mn, and found that α_{all} was softer than the other constituents of the weld. It was therefore hypothesized that an inclusion within the grain boundary allotriomorphic ferrite initiated fracture, due to local plasticity being concentrated in these softer regions. Also it was thought that the large size of these regions of grain boundary allotriomorphic ferrite allowed for larger dislocation pile-up lengths to form against the inclusion, thus making these sites more likely for cleavage fracture nuclei. Initiating cleavage fracture inclusions were found to be in the top 1% of distribution of inclusion size, as measured from the ductile fracture surface. However, the model did not take into account the effect of the inclusion chemistry or residual stresses. An overview of fracture in C-Mn weld metals was carried out by Tweed and Knott [143], which suggested that inclusions might induce tessellated stresses as a result of the differential thermal contractions between the matrix and the inclusion on cooling. These stresses are described by the following equation:

$$\sigma = \Phi[(\alpha_m - \alpha_i)\Delta T] \dots (2.6)$$

where α_m and α_i are coefficient of thermal expansion for the matrix and inclusion respectively, ΔT is the positive temperature change and Φ is a function of the elastic properties of the matrix and the inclusion and its size, shape and distribution.

1. If $\alpha_m < \alpha_i$ a void will form between the inclusion and the matrix, if the bonding of the interface between them is weak.
2. If $\alpha_m > \alpha_i$ on cooling the inclusion will be subject to radial compressive and tensile circumferential stresses which reduce as a function of the reciprocal radius cubed.

Values of α_m and α_i suggested that manganese silicate inclusions commonly found in welds case (1), and that from manganese sulphide case (2) would both be true. Suggesting that not only does inclusion chemistry affect the surrounding microstructure, but it also effects the stress field surrounding the inclusion. The estimated maximum values of the circumferential stress σ_{cm} is related to the matrix yield stress σ_{my} by the following expression:

$$\sigma_{cm} = \frac{\sigma_{my}}{3} \quad \dots(2.7)$$

2.6.9.3 Microstructural differences in toughness of multipass welds.

Tweed and Knott [7] investigated differences in toughness of a multipass weld. Due to the nature of multipass welding, two microstructures are created AD and RH within the weld metal. The work simulated regions of the RH microstructure by radio-frequency induction coil heating and water cooling; it was noted that the RH microstructural regions exhibited a significant increase in toughness compared to the AD microstructure. Novovic [13] confirmed this in a recent study, using C-Mn weld metal, and carefully positioning notches

(Charpy tests) and pre-cracks in fracture toughness testing in real AD and RH microstructures, therefore sample one on microstructure. The results from the Charpy tests showed the ductile-to-brittle transition was lower for the RH microstructure compared to the AD microstructures within the same weld metal; a difference was also noted in the upper shelf energies of the Charpy tests, with the RH microstructure showing lower upper shelf energies than those of the AD microstructure. Similar differences were also noted in fracture toughness experimental results.

Chapter 3 - Fracture Mechanics.

3.1 Linear Elastic Fracture Mechanics

3.1.1 The Griffith Theory

In order to explain the reasons for differences between the predicted and actual experimentally obtained values of fracture strengths of glasses and crystals (i.e. two orders of magnitude lower than the theoretical fracture strength of a solid, of the order of $E/10$), Griffith [144] considered propagation of brittle cracks in glasses and postulated that a crack would extend under the applied stress only if the total energy would be decreased. Thus comparing the decrease in elastic strain potential energy with energy needed to create new crack surfaces.

Griffith [145] derived the fracture stress, σ_F , for an infinite plate of unit thickness, with a through-thickness crack of length $2a$, and the crack is lying normal to the direction of the applied stress, σ , at infinity, Fig. 3.1, considering thermodynamic energy balance between surface energy required and strain energy released for the crack to advance. The fracture process was not focussed at the crack tip, fracture stress can be defined as:

$$\sigma_F = \left(\frac{2E\gamma}{\pi a} \right)^{\frac{1}{2}} \quad \dots (3.1)$$

in the case of plane stress, where E is Young's Modulus. The equivalent expression for plane strain loading is:

$$\sigma_F = \left(\frac{2E\gamma}{\pi(1-\nu)a} \right)^{\frac{1}{2}} \quad \dots(3.2)$$

where ν is Poisson's ratio (0.27-0.30).

The Griffith's approach allowed for the consideration of the sample as a whole, therefore not considering the highly strained region surrounding the crack tip and yet obtaining a useful fracture stress expression.

Equation 3.1 can be rewritten as:

$$\frac{\sigma^2 \pi a}{E} = 2\gamma \quad \dots(3.3)$$

The strain energy release rate, G , is defined by the left hand side of the equation and can be considered that the potential energy release rate represents graphically the slope of change in energy with respect to crack length ($\delta U/\delta a$). It also represents the surface energy increase and may be designated as crack resistance, R , with fracture occurring when G exceeds the critical value, G_c , and must be at least equal to R .

$$\frac{\pi \sigma^2 a}{E} = \frac{\pi \sigma_c^2 a}{E} = G_c = R \quad \dots(3.4)$$

Although the Griffith theory in its original forms exhibits poor agreement when there is plastic deformation occurring ahead of the crack tip, this is the case for most ductile materials

when fracture is being considered. For example, assuming the crack size, a , and the surface energy γ , the predicted fracture stress values through equations 3.1 and 3.2 were considerably lower than those seen experimentally.

The general rule of defects with decreasing fracture strength consists of the inverse square root relationship between the fracture stress and crack length. Irwin [146] and Orowan [147] independently suggested the Griffith theory for ideally brittle materials could be modified and applied to metals that exhibit some degree of plasticity if the work completed is close to the crack tip and completed during plastic deformation is considered in calculations, Fig. 3.2.

$$\sigma_F = \left(\frac{E(2\gamma_e + \gamma_p)}{\pi(1-\nu^2)a} \right)^{\frac{1}{2}} \quad \dots(3.5)$$

where γ_p represents the energy exhausted in the plastic work necessary to produce unstable crack propagation, thus prior to the onset, for relatively ductile materials $\gamma_p \gg 2\gamma_e$ becomes:

$$\sigma_F = \left(\frac{E\gamma_p}{\pi(1-\nu^2)a} \right)^{\frac{1}{2}} \quad \dots(3.6)$$

This equation although modified is still limited to defining conditions required for stability of an ideally sharp crack, this presents problems for practical applications, as the linear elastic approach relates fracture stress to crack length, even through crack-tip plastically was preceding fracture.

3.1.2 The Stress Intensity Factor Approach

Following on from the solutions of Westergaard [148] and using linear elastic theory Irwin [146] developed the stress intensity approach. He showed that the elastic stress field in the region of a crack tip takes the form:

$$\sigma_{ij} = \frac{K}{\sqrt{2\pi a}} f_{ij}(\theta) + \dots \quad \dots(3.7)$$

where σ_{ij} is the stress component;

f_{ij} is a geometrical factor in the direction of ij ;

K is the stress intensity factor;

θ and r are the cylindrical polar co-ordinate of a point with respect to the crack tip.

Equation 3.7 is only valid for a singular elastic stress field; any plasticity disturbs this stress singularly.

Within the vicinity of a crack tip all stress systems may be derived from three simple modes of loading, Fig. 3.3. For these cases, the stresses in the vicinity of the crack tip for a crack length $2a$, in a biaxially loaded infinite plate (Fig. 3.4) are given by:

Mode I

$$\begin{aligned}
\sigma_x &= \frac{\sigma\sqrt{\pi a}}{\sqrt{2\pi a}} \cos \frac{\theta}{2} \left(1 - \sin \frac{\theta}{2} \sin \frac{3\theta}{2} \right) \\
\sigma_y &= \frac{\sigma\sqrt{\pi a}}{\sqrt{2\pi a}} \cos \frac{\theta}{2} \left(1 + \sin \frac{\theta}{2} \sin \frac{3\theta}{2} \right) \quad \dots(3.8) \\
\tau_{xy} &= \frac{\sigma\sqrt{\pi a}}{\sqrt{2\pi a}} \sin \frac{\theta}{2} \cos \frac{\theta}{2} \cos \frac{3\theta}{2} \\
\sigma_z &= \nu(\sigma_x + \sigma_y)
\end{aligned}$$

Equation 3.8 shows that all the stresses tend towards infinity at the crack tip (e.g. $a = 0$), these are the products of the geometrical position $2(\pi a)^{\frac{1}{2}} f(\theta)$ and a factor of $\sigma(\pi a)^{\frac{1}{2}}$. This factor determines the magnitude of elastic stresses in the crack tip field, in the case of Mode I the stress intensity factor K_I is:

$$K_I = \sigma\sqrt{\pi a} \quad \dots(3.9)$$

Mode II

$$\begin{aligned}
\sigma_x &= \frac{K_{II}}{\sqrt{2\pi a}} \sin \frac{\theta}{2} \left(2 + \cos \frac{\theta}{2} \cos \frac{3\theta}{2} \right) \\
\sigma_y &= \frac{K_{II}}{\sqrt{2\pi a}} \sin \frac{\theta}{2} \left(\cos \frac{\theta}{2} \cos \frac{3\theta}{2} \right) \quad \dots(3.10) \\
\tau_{xy} &= \frac{K_{II}}{\sqrt{2\pi a}} \cos \frac{\theta}{2} \left(1 - \sin \frac{\theta}{2} \sin \frac{3\theta}{2} \right) \\
\sigma_z &= \nu(\sigma_x + \sigma_y), \tau_{xz} = \tau_{yz} = 0
\end{aligned}$$

where for an infinite cracked plate with uniform plane shear τ at vicinity:

$$K_{II} = \tau\sqrt{\pi a} \quad \dots(3.11)$$

Finally for Mode III

$$\begin{aligned} \tau_{xz} &= \frac{K_{III}}{\sqrt{2\pi a}} \sin \frac{\theta}{2} \\ \tau_{yz} &= \frac{K_{III}}{\sqrt{2\pi a}} \cos \frac{\theta}{2} \quad \dots(3.12) \\ \sigma_x = \sigma_y = \sigma_z = \tau_{xy} &= 0 \end{aligned}$$

where

$$K_{III} = \tau\sqrt{\pi a} \quad \dots(3.13)$$

The above equation shows the stress intensity factor, however it is not suitable for practical applications as it's obtained for an infinite plate. The expression has to be modified for practical applications, with a finite size, by adding correction factors. Mode I loading (pure tension) whilst under plane strain (triaxial stress state) conditions is most important to consider in metals for practical cases, and thus analysis is focused on this mode. The general form of the modified expression is:

$$K_I = C\sigma\sqrt{\pi af\left(\frac{a}{W}\right)} \quad \dots(3.14)$$

where C and $f\left(\frac{a}{W}\right)$ have been determined for each case by the stress analysis, and W is the width of the specimen. For Charpy size specimens (10x10x55mm), K_I is defined by the following equation, considering all limits are satisfied [149]:

$$K_I = \frac{PS}{BW^{\frac{3}{2}}} f\left(\frac{a}{W}\right) \quad \dots(3.15)$$

where

$$f\left(\frac{a}{W}\right) = \frac{3\left(\frac{a}{W}\right)^{\frac{1}{2}} \left[1.99 - \left(\frac{a}{W}\right) \left(1 - \frac{a}{W}\right) \left(2.15 - \frac{3.93a}{W} + \frac{2.7a^2}{W} \right) \right]}{2 \left(1 + \frac{2a}{W} \right) \left(1 - \frac{a}{W} \right)^{\frac{3}{2}}} \quad \dots(3.16)$$

From the application of virtual work principle (e.g. calculating work by surface forces acting across length δa when the crack increases in length from a to $a+\delta a$ [146]) it can be seen that K is associated to the strain (or potential) energy release rate, G in plane stress conditions by:

$$G = \frac{K_I^2}{E} \quad \dots(3.17)$$

and in plane strain

$$G = \frac{K_1^2}{E}(1-\nu^2) \quad \dots(3.18)$$

where ν is Poisson's ration, thus at fracture (plane strain):

$$G_{IC} = \frac{K_{IC}^2}{E}(1-\nu^2) \quad \dots(3.19)$$

Where the fracture toughness of the material, K_{IC} is critical stress in Mode I loading subjected to tensile stress. It can also be considered a materials parameter and represents the material's resistance to brittle fracture. Unstable crack propagation can be defined using both K_{IC} and G_{IC} , although K_{IC} is generally used to characterise the fracture resistance of the materials due to the difficulties in calculating G_{IC} . K_{IC} is used in linear elastic fracture mechanics and can be either numerically or mathematically determined by the technique of elastic stress analysis for various kinds of geometries and stress systems. The method by which K_{IC} is determined has been standardised a British Standard BS 7448: Part 1: 1991 [149] using testpieces of varying geometries and that have been fatigue pre-cracked.

Combining equation 3.9 for perfectly brittle (elastic failure) and rearranging with equation at failure in Mode I loading and in plane strain conditions, gives:

$$\sigma_F = \sqrt{\frac{EG_{IC}}{\pi(1-\nu^2)a}} \quad \dots(3.20)$$

Thus placing $G_{IC} = 2\gamma_p$ in to the above equation gives the original Griffith relationship. It should be emphasised that values obtained experimentally from fracture stress tests of critical

strain energy release rate, G_{IC} , and “effective surface energy”, γ_p are distinct parameters. Using equation 3.6 for a given microcrack with size half-length $1\mu\text{m}$ and known cleavage fracture values, usually ranging from 2-14 Jm^{-2} , experimental values for γ_p can be obtained. However, using typical values for ferritic steels at low temperature of $E = 206\text{MPa}$, $\nu = 0.33$ and $K_{IC} \approx 50\text{MPam}^{1/2}$ into equation 3.19, values of G_{IC} are obtained in the order of 10^4Jm^{-2} . The reason for the difference in results is because σ_F and therefore γ_p are related to the local tensile stress in the process zone of the crack tip and therefore only consider events at instant infinitesimal crack extension (δa).

3.1.3 Critical Tensile Fracture Stress, σ_f^*

Using blunt-notched bend specimens Knott studied the local critical tensile stress, σ_f^* , for transgranular cleavage fracture [150, 151]. It was established that this parameter depended weakly upon the test temperature if cleavage was slip-induced. Many other researchers have ascertained similar results for a selection of steels with different microstructural conditions over a low temperature range, mainly quenched and tempered steels [9-11, 152, 153], weld metals containing lath-microstructure [22], C-Mn weld metals [7, 13, 52], C-Mn bainitic steels [154] and MnMoNi weld metals [14, 15]. These assumed that cleavage fracture stress σ_f^* was inversely proportional to the square root of the corresponding initiating feature within the microstructure, e.g. second phase particles and non-metallic inclusions. A modified Griffith equation was used to predict values of the effective surface energy, γ_{eff} , as shown in equation 3.6.

3.1.3.1 Effective Surface Energy, γ_{eff}

Cleavage fracture was analysed by Curry and Knott [155] in spheroidised plain carbon steels, given that the statistical distribution of carbide particles for these steels is less complicated than that of grain boundary carbide films in a ferritic matrix. The model was based on the

propagation of a penny shaped crack forming from the cracking of carbides and considering this as Griffith type defects. The Griffith crack propagation is slightly different for this geometry compared with through-thickness cracks and is given by:

$$\sigma_F = \left(\frac{E \gamma_p}{\pi(1-\nu)d} \right)^{\frac{1}{2}} \quad \dots (3.21)$$

where d is the diameter of coarsest carbide particle in the region ahead of the crack tip. Good agreement was found between experimental and predicted σ_F^* cleavage strength values. There have been considerable attempts made for the estimation of γ_p values, with little agreement from different authors. A lower bound value of γ_p is usually considered to equate to 2Jm^{-2} [156], this value has been inferred from extrapolation of the measurement of the “true” surface energy of delta ferrite at 1400°C , where zero-creep experiments were used and no contribution of dislocation movement is considered. γ_p values as high as 180Jm^{-2} have been suggested [157], it should be noted, however that a critical size defect must be assumed or measured to estimate a reasonable values for γ_p , thus estimates for γ_p should be carefully considered. Curry and Knott [155, 158] showed values of 14Jm^{-2} in spheroidised carbide microstructures for γ_p values, the increase from the lower bound values of 2Jm^{-2} was considered to be due to the plastic work contribution of the creation and limited dislocation movement necessary at the crack tip in the fracture process. Bowen [9] used a quenched and tempered A533B steel and observed best fit γ_{eff} values of 9Jm^{-2} , based on measured cleavage fracture stress and the coarsest observed carbide size. Similarly, McRobie [52, 159] found γ_{eff} values of approximately 9Jm^{-2} for cleavage fracture stress in C-Mn weld metals through notched bars. Curry and Knott have observed a range of values from 2 to 25Jm^{-2} for γ_p values by compiling data from literature [158]. It has been revealed that the cleavage fracture stress is strongly dependant on the grain size, with it being higher in fine grain steels.

Bowen and Knott [9, 11] observed no dependence of cleavage fracture stress on martensitic packet size, prior austenite grain size or martensitic lath width and concluded that carbide

width was the only microstructural controlling feature. It was also suggested [7, 52] that non-metallic inclusions are responsible for initiation of cleavage fracture in C-Mn weld metals under certain circumstances. This theory which was supported by microstructural information, gave rise to the proposal for the model for C-Mn weld metals, which was developed by analogy from previous models in wrought mild steel for cleavage. The model carefully considered that plasticity was confined to grain boundary ferrite. Encouraging the inclusion to crack, which in turn would act as a cleavage initiation site, if a critical diameter and tensile stress level were attained. Thus cleavage would then propagate through grain boundary ferrite.

3.1.4 Linear Elastic Fracture Mechanics (LEFM)

3.1.4.1 Fracture Toughness Testing

Linear elastic fracture mechanics can be used to describe the condition of unstable crack growth when the extent of the crack tip is limited plastically, even though structural materials do not behave in a purely elastic manner during fracture. Plane strain fracture toughness, K_{IC} , can be considered a materials property that is dependent upon temperature and loading rate of the test. According to the standards ASTM E399-90 and BS5447:1977 two types of samples can be used; the single edge notched bend testpiece (SEN) and compact tension testpiece (CT), Fig. 3.5 and 3.6.

The specimen size required to give a valid K_{IC} has to fulfil plane strain conditions, so triaxial stress state is obtained and the stress intensity analysis is unaffected by the plastic zone size and high constraints can occur around the crack tip. After extensive experimental work the following empirical minimum size of specimen was derived:

$$B \text{ and } a \geq 2.5 \left(\frac{K_{IC}}{\sigma_{ys}} \right)^2 \quad \dots (3.22)$$

and

$$W \geq 5.0 \left(\frac{K_{IC}}{\sigma_{ys}} \right)^2 \quad \dots (3.23)$$

where a is the initial crack length of the specimen, B is the thickness of the specimen and σ_{ys} is the yield stress at test temperature. Low alloy ferritic steels normally have a low yield strength ranging from 400 to 500 MNm⁻², consequently elevated toughness, meaning the size of the test piece required to satisfy the valid K_{IC} criteria in equation 3.22 would be very large indeed.

Wessel [160] used compact tension specimens of different sizes, up to 300mm thick, shown in Fig. 3.7, also shown are the results obtained for an A533B Grade B Class 1 steel (1.35%Mn, 0.5%Ni, 0.23%C, 0.5%Mo) heat treated to a yield stress of 500 MNm⁻² at room temperature.

For SEN specimens the stress intensity factor is given by the following equation:

$$K_1 = \frac{PS}{BW^{\frac{3}{2}}} f\left(\frac{a}{W}\right) \quad \dots (3.24)$$

and for the CT specimen by the following equation:

$$K_I = \frac{P}{BW^{\frac{1}{2}}} f\left(\frac{a}{W}\right) \quad \dots(3.25)$$

For a valid test K_{IC} it is first necessary to compute a tentative value of K_Q based on a graphical construction of a load-displacement test record. If K_Q satisfies the condition of equation 3.22 then $K_Q=K_{IC}$. Most structural materials present considerable toughness, thus the size of the testpiece is large for a valid K_{IC} test and awkward to test with conventional equipment. It should be considered that the amount of material necessary to obtain a virtually constant toughness value is also a drawback, mainly when considering the testing of reactor pressure vessel steels. Thus the determination of K_{IC} of structural materials is not always practical and other testing methods need to be considered, as well as the effects of the plastic zone size of the stress intensity approach which have to be limited to quantify the fracture toughness properties of these materials, but plane strain fracture toughness represents the lower limiting critical toughness of a material.

3.1.4.2 The Crack Growth Resistance Curves Concept (J-R and δ -R Curves)

When both ductile and brittle fracture occurs in the same testpiece the R -curve concept can be used to address this problem. This method is used to make quantitative estimates of the increase in resistance to fracture as the crack is growing by “resistance curves” or “ R -curves” and can be defined as:

$$R = \frac{d(U_\gamma)}{da} \quad \dots(3.26)$$

where U_γ is change in elastic energy of the loaded uncracked plate, U_0 is a result of the formation of crack surfaces. Crack instability will occur when the elastic energy release rate is greater than crack resistance:

$$G \geq R \quad \dots(3.27)$$

The crack resistance R is considered to independent of crack extension Δa , if the plane strain condition is satisfied (Irwin's analysis). But a rising R -curve may develop as crack length increases in plane stress or intermediate plane stress-strain conditions, thus on loading a thin sample containing a crack, stable crack growth will occur up to the point of plastic collapse of general yielding of the sample or before instability and fracture.

Various standards detail how to obtain crack extension resistance curves, for example the British Standard BS7448-4:1997 [161] and GKSS 94/E/60 [162]. As there are two specimen designs that can be used of the K_{IC} test, choice will be dependent upon crack orientation and quantity of available material. There are also two techniques available to determine crack extension; multiple and single specimen methods. In the single specimen approach the crack extension is monitored via an unloading compliance technique where loading slopes are produced at specific intervals during the tests, these can be used to estimate the crack length at each unloading interval. The multiple specimen method as regarded is the definitive approach

3.1.4.3 Slow Notched Bend Testing

Slow notched bend testing is mainly utilised to distinguish both mechanical and microstructural effects on the micromechanisms of cleavage fracture. There is a large amount of research relating to the behaviour in slow blunt notched test specimens, meaning there is more known about the plastic-elastic stress distributions ahead of the notch in the process

zone of interest, than in pre-cracked specimens (Knott [144]). The elastic-plastic stress distribution around a notch, as analysed by Griffith and Owen [163] using finite element methods, predicted the variation of tensile stress, σ_{11} , ahead of the notch as a function of the applied load (general yield stress). The maximum tensile stress, at failure $\sigma_{11(\max)}$, is defined as the microscopic or local cleavage fracture stress, σ_F^* , this was related to the size of the microcrack through a modified Griffith equation of the form [164]:

$$\sigma_F^* = \sqrt{\frac{4E\gamma_p}{\pi(1-\nu^2)d}} \quad \dots(3.28)$$

Where d is the size of defect and γ_p is the “effective surface energy”.

Curry and Knott [155] studied cleavage fracture in a spheroidised plain carbon steel relating σ_F^* to the size of a microcrack through a modified Griffith equation for a penny-shaped crack Equation 3.21. Both of these equations can be used to estimate the value for γ_p from the linear relationship between the reciprocal square root of the microcrack sizes (crack initiation) and the measured values for σ_F^* . It should be noted that γ_p values are an estimate, as the intrinsic cleavage fracture stress is inconsistent and depends on local characteristics of the material.

3.1.5 Elastic Plastic Fracture Mechanics (EPFM)

As discussed the Linear Elastic Fracture Mechanics approach (LEFM) is useful when used to analyse a material with intrinsic brittle behaviour, where plane strain conditions can be satisfied. LEFM can be applied to modifications to materials that exhibit limited crack plasticity. However, structural materials are usually too ductile, because of their high toughness to be dealt with using such principles; hence the Elastic-Plastic Fracture Mechanics

(EPFM) approach extends the description on fracture behaviour beyond the elastic regime. Two approaches can be used to predict the crack initiation behaviour of the material; Crack Tip Opening Displacement (CTOD) [165, 166] principally developed in the UK, and the J-integral [165-167] energy balance developed in the USA.

3.1.5.1 Crack-Tip Opening Displacement (CTOD)

The concept of CTOD was introduced by Wells [166-168] as an alternative idea to Irwin [146]. Wells assumed that crack opening displacement (COD) was directly proportional to tensile strain after general yielding had been achieved, Fig. 3.8. Under general yielding conditions, plastic flow is not constrained: the plastic zone spreads over the entire cracked section. The crack was expected to propagate when the plastic strain at the tip exceeded a critical value. The measure of strain is COD and the fracture criterion is critical COD.

Wells attempted to explain why small scale test specimens, which had been removed from a large section ship-plate, fracture after generally yield with fibrous fracture appearance compared to the ship-plate which had fractured before general yielding. In the latter case the fracture surface showed a crystalline appearance of more than 90%, when tested at the same temperature. Wells evaluated COD by using Irwin's estimate of the plastic zone size and employing an elastic solution for the displacement of a centred crack in an infinite body, Fig. 3.9.

$$COD = \frac{4\sigma}{E\sqrt{(a+R)}} \Rightarrow CTOD = \frac{4}{E} \sqrt{2aR} = \frac{4}{\pi} \frac{k_I^2}{E\sigma_{YS}} \quad \dots(3.29)$$

It can be seen from the above equation that CTOD is equivalent to K_{IC} when linear elastic fracture mechanics criteria are applied. As a result, small scale tests could be performed to overcome the dimensional limitations imposed by the K_{IC} test from measuring fracture toughness of ductile materials.

Measurement of this distance Δ or COD can be referred to as δ_c , the critical CTOD at the point of fracture, this is expressed as:

$$COD = \Delta = \frac{4\sigma}{E} \left(a^2 - x^2 + \frac{E^2}{16\sigma^2} \delta^2 \right)^{\frac{1}{2}} \quad \dots(3.30)$$

Alternative models for CTOD were developed by Burdekin and Stone [169], which were based on the Dugdale model, shown in Fig. 3.10. This model described the crack-tip opening displacement for a crack of length $2a$, in an infinite thin plate which is subjected to uniform tension (σ) in a material, where plastic deformation occurs at the crack tip, this is given by [40]:

$$\delta_t = \frac{8\sigma_{ys}a}{\pi E} \ln \left[\sec \left(\frac{\pi\sigma}{2\sigma_{ys}} \right) \right] \quad \dots(3.31)$$

Equation 3.31 was obtained for tensile loading allowing for the measurement of critical COD, δ_c for small scale testpiece which fractures after general yielding. This can be used to predict fracture stress σ , of a large scale structure fracturing before general yield. Crack tip opening displacement, CTOD can be applied to the assessment of the integrity of structures, under linear elastic fracture mechanics, δ_t and can be directly related to K_I :

$$\delta_t = \frac{K_I^2}{E\sigma_{ys}} \quad \dots(3.32)$$

CTOD can be defined as the opening distance between the intercept with the deformed crack profile of two lines drawn back from the crack-tip at 45° , Fig. 3.11 [170]. However it can only be validated in a quantitative manner for an infinite plate. Measuring of CTOD is calculated by loading a pre-cracked specimen in three-point bending configuration and measuring the load versus notch opening displacement curves (V_p). CTOD is evaluated using:

$$\delta = \delta_e + \delta_p = \frac{K_I^2(1-\nu^2)}{m\sigma_{ys}E} + \frac{r_p(W-a)V_p}{r_p(W-a) + a + Z} \quad \dots(3.33)$$

where δ_e is the elastic component, δ_p is the plastic component, m is a dimensionless constant (≈ 2.0 for plane strain), a is crack length, r_p is the plastic rotation factor and Z is the distance of the knife edges above the notch.

3.1.5.1.1 Effect of Specimen Size and Geometry on CTOD

δ_i is the value of the initial crack tip opening displacement and appears to be a characteristic of the material, which is independent of thickness and geometry as shown in Fig. 3.12 and Fig. 3.13 [144, 171]. It can be seen from the figures that similar results are obtained for both the four and three-point bend specimens, there were equivalent results obtained for four-point bend and compact test specimens. Fig. 3.14 depicts the effect of thickness of specimen; it can be seen that regardless of differences in the rate of COD fibrous crack growth and the point of maximum load, good agreement between δ_i values is found [144]. For specimens greater than 2mm, δ_i is independent of specimen thickness, therefore changes leading to an increase in constraint would cause a reduction in COD, e.g. for thick specimens or if the specimen was loaded in four rather than three-point bend.

Effects of constraint are more important in terms of cleavage fracture initiation, for example if general yield is attained before the critical COD value at the crack tip (the piece is brittle) or if the specimen is big enough that the δ_{crit} is attained by general yielding (the piece is ductile) [144, 172]. As a consequence cleavage fracture depends on the maximum attainable stress ahead of the crack tip and hence on the test piece constraint, while the maximum load failure depends upon plastic collapse of the ligament [173]. These such size effects on CTOD are summarised in Fig. 3.14 [172], also it should be noted that using side-grooves to inhibit through-thickness yield can increase the constraint.

3.2 Microscopic Models For Cleavage Fracture

Griffiths proposed a theory for brittle fracture considering the presence of sharp crack like defects within the material. Except, materials always contain some microscopic flaws but not all will be of sufficient size to produce catastrophic failure. It should be noted that cleavage fracture initiation is always preceded by some local deformation or plastic yielding, as shown by Low [174]. In this experiment, Low used iron tensile specimens, for a given grain size fracture in tension and yield in compression were at the same stresses, as shown in Fig. 3.15. It was also demonstrated by Knott [144], that cleavage fracture is preceded by local yielding because twinning or slip is necessary to initiate a microcrack. Hence the following sections consider cleavage fracture to be initiated by slip.

3.2.1 Stroh's Theory

Zener [175] first discovered the concept that cracking initiates from a dislocation pile-up against a barrier, it was proposed that a pile-up was a potential stress raiser and concentrated tensile stress ahead of it might be high enough to initiate a crack. Stroh [176, 177] later used Zener's theory to analyse the conditions required to nucleate and propagate a crack in front of a dislocation pile-up, shown in Fig. 3.16. Using a presumption similar to the Petch [178]

model for yielding, both models are based on the process by which mobile dislocations are produced in the unyielding grain, a relationship was obtained between the materials grain size and cleavage fracture stress:

$$\sigma_F = \sigma_i + k_F d^{\frac{1}{2}} \quad \dots(3.34)$$

where k_F refers to critical value of tensile stress required to fracture the second grain with a diameter of d . This predicts in fine-grained materials the increase in cleavage fracture stress, but gives no clear indication of the meaning of k_F and does not explain why there is variation of fracture stress in grain size from experimental results as shown in Fig. 3.17. Stroh [176, 177] investigated the meaning of k_F . He calculated that the magnitude of the maximum local tensile stress, ahead of a pile-up of dislocations, $\sigma_{\theta\theta}$, where θ is equal to 70.5° to the direction on the slip-band propagation, necessary to propagate a Griffith like microcrack nuclei, is expressed as:

$$\sigma_{70.5} = \frac{2}{\sqrt{3}} \left(\frac{d}{2r} \right)^{\frac{1}{2}} (\tau - \tau_i) \quad \dots(3.35)$$

where r is the distance from the pile-up, d is the grain diameter, τ is the shear stress and τ_i is the friction stress, thus substituting this stress into the Griffiths equation, the conditions influencing the spread of the nucleus can be written as:

$$\tau_{eff} = \tau - \tau_i \geq \left[\frac{\pi\mu\gamma}{2(1-\nu)d} \right]^{\frac{1}{2}} \quad \dots(3.36)$$

where ν is Poisson's ratio, d is the slip-band length (grain diameter), μ is the shear stress modulus, γ is the surface energy, and τ_{eff} is the effective shear stress. If a crack nucleus can form, there is a decrease in the total energy of the system with increasing nucleus length; this is assuming that the total surface energy created by the growing crack is constant throughout the fracture process. It also assumes that the cleavage is nucleation controlled, that the number of dislocations present is enough to nucleate a crack and may be squeezed together at the end of a slip band. The critical number is given by [144]:

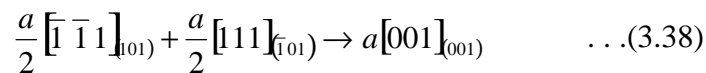
$$n = \frac{\pi^2 \gamma}{2\tau_{\text{eff}} b} \quad \dots (3.37)$$

where b is the Burgers vector of the dislocation. It can clearly be seen from the above equation that assuming there is constant effective shear stress, fewer dislocations, e.g. short slip-band lengths, are required to nucleate a microcrack in a material which has a low surface energy. If tensile stress is made the most important parameter, fracture should be growth-controlled rather than nucleation controlled, as shown experimentally by Orowan [147, 179] and Parker [180], Fig. 3.18. However equation 3.44 shows this is impossible, but Stroh's theory can be applied to the cleavage fracture of steels if some brittle second phase provides a low surface energy region and the fracture is controlled by nucleation. However Cottrell [41, 42, 165] argued that crack propagation is the most difficult step rather than its nucleation [22, 181], therefore the process is growth controlled, as explained in the following section.

3.2.2 Cottrell's Theory

An easy nucleation process was proposed by Cottrell [42], a different dislocation mechanism for crack nucleation in cleavage fracture, allowing the growth to be the influencing factor. This mechanism of cleavage is based on an energetically favourable dislocation reaction in bcc materials as shown in Fig. 3.19. Consider a dislocations in bcc iron, with Burgers vectors

$a\langle\bar{1}\bar{1}1\rangle/2$ moving on a slip plane of (101) and Burgers vectors $a\langle 111\rangle/2$ is gliding on the intersecting $(\bar{1}11)$ plane, the leading dislocation can coalesce to form a new edge dislocation as given by:



As a result a dislocation is formed with the reduction in energy, a sessile edge dislocation (the line of intersection of the planes is [010] with a Burgers vector normal to the cleavage plane of (001) [144]), and thus the first stage of micro-crack initiation. If this reaction is repeated with corresponding decrease in dislocation energy then a wedge-shape crack can nucleate.

Once the crack nucleus initiates it will propagate under an applied load, so cleavage fracture can not be propagation controlled with cleavage stress, σ_F :

$$\sigma_F \geq \frac{2\gamma\mu}{K_y^s} d^{\frac{1}{2}} \quad \dots(3.39)$$

where K_y^s is the yielding constant in the Hall-Petch equation and d is the grain size. This model explains the effect of yielding parameters and grain size, but also emphasises the important of tensile-stress on cleavage fracture. Nevertheless it does not take into account the possible influence of other microstructural parameters, such as the influence of second phase particles [182].

3.2.3 Smith's Theory

The initial model of complementary growth controlled cleavage fracture that incorporated the effects of carbides was proposed by Cottrell [42, 165]. Latter research observed in tensile specimens that grain boundary carbide and pearlite lamellae cracked prior to cleavage fracture [183, 184], McMahon and Cohen [182] studied tensile specimens made from very low carbon steels, over a low temperature range and observed the occurrence of cleavage micro-cracking, the results showed that coarse carbides promoted cleavage, whilst fine carbides allowed the material to behave in a ductile manner. On the basis of these experiments, Smith [185] proposed a theoretical cleavage model for mild steel, this included the effect of the stress field from the dislocation pile-up required to nucleate a microcrack, shown in Fig. 3.20. Based on Stroh's analysis for steel, the fracture stress σ_F required for a micro-crack to propagate from a grain-boundary carbide of thickness C_0 with a grain-size d is given by:

$$\left(\frac{C_0}{d}\right)\sigma_F^2 + \tau_{eff}^2 \left[1 + \frac{4}{\pi} \left(\frac{C_0}{d}\right)^{\frac{1}{2}} \frac{\tau_i}{\tau_{eff}}\right]^2 \geq \frac{aE\gamma_{eff}}{\pi(1-\nu^2)d} \quad \dots(3.40)$$

where σ_F is the critical values of tensile stress to propagate the nucleus, τ_{eff} is the effective shear stress (τ_{app} , applied shear stress minus the lattice friction stress, τ_i), γ_{eff} is the effective surface energy concerned in propagating the microcrack nucleus into the ferrite matrix. From the above equation it can be seen that both the first term, known as a "Griffith's term" and the second term are related to the stresses that arise from dislocation pile up. For annealed mild steel, researchers have approximated that the overall effect of stress arising from the dislocation pile up on crack propagation is less than 10% [186, 187]. This is even smaller in the case of spheroidal carbides, because the dislocation arrays are not in the form of grain-diameter length pile-ups but as loops twisted around individual particles [187]. Thus, the contribution of the dislocation pile-up can be discounted; the criterion reduces the Griffith relationship for grain-boundary carbide microcrack of length C_0 :

$$\sigma_F > \sqrt{\frac{4E\gamma_p}{\pi(1-\nu^2)C_0}} \quad \dots(3.41)$$

Rewriting τ_{eff} as $K_y^s d^{-\frac{1}{2}}$ in terms of the Hall-Petch relation [178, 188, 189] (Equation 3.42), means equation 3.40 can be re-written as:

$$C_0\sigma_F^2 + (K_y^s)^2 \left[1 + \frac{4}{\pi} (C_0)^{\frac{1}{2}} \left(\frac{\tau_i}{K_y^s} \right) \right]^2 \geq \frac{4E\gamma_{\text{eff}}}{\pi(1-\nu^2)} \quad \dots(3.42)$$

From this equation it can be seen that cleavage fracture stress is independent of grain size d . However, as Curry and Knott [155] pointed out carbide thickness is often related to grain size, thus from this theory it is easier to predict that finer grain size may promote a higher fracture resistance.

3.2.4 Measurement of the Microscopic Cleavage Fracture Stress

Tensile specimens were used to evaluate fracture stress as presented in previous research [182-184]. Tensile testing has numerous disadvantages, with the main influence being the testing machine, whether this is in displacement or load control. Also the temperature range at which cleavage fracture occurs prior to necking, this is very limited or nil, in some cases low alloy ferritic steels tested at liquid nitrogen temperature (-196°C) exhibited some degree of yielding prior to catastrophic failure. Knott [150, 151] applied slip-file theory to notched bend specimens to evaluate fracture stress when it was coincident with yielding, but this method has limitations as the notch geometry needs to be varied to determine cleavage fracture stress over a wide range of temperatures.

Griffiths and Owen [163] used a four-point bend testpiece to analyse the elastic-plastic stress distribution around a blunt notch, using finite element analysis and calculated the maximum principal stress, σ_{yy} , as a function of the distance below the notch, Fig. 3.21 and 3.22. Maximum tensile stress is defined as microscopic cleavage fracture stress, which is located within the plastic zone. At low loads distribution is similar to that predicted by slip-field theory, whereas at high loads, in a strain-hardening material the maximum σ_{yy} occurs at a great distance away from the plastic/ elastic interface. More recent research in to ferritic steels and weld metals, Bowen [9-11, 152, 153] and McRobie and Knott [7, 52], established that cleavage fracture is controlled by microscopic cleavage, furthermore microscopic cleavage fracture stress is expected to be independent of notch geometry and test temperature.

3.3 Fracture Criteria for Precracked Specimens

3.3.1 Microstructural Effects on Cleavage Fracture

When designing engineering structures, great emphasis is placed on brittle fracture of metals, where it is assumed that cleavage occurs when the stress intensity factor exceed a “macroscopic” or “engineering” value of fracture toughness, K_{IC} . Techniques have been developed that collate metallurgical features to microscope applied fracture stress, such as the size of any defect within the material. Many researchers have investigated if a crystal cleavage event could be defined as an extension of cracked carbide, an inclusion, a M-A-C constituent, or pearlitic carbides.

Fracture of mild steels is believed to occur when a microcrack occurs at brittle grain-boundary carbide and propagates at the critical tensile stress into the ferrite matrix. Smith's [190] model predicts cleavage fracture stress is mainly affected by the carbide precipitates in contrast to experimental results that demonstrate that σ_F is dependent on grain size. However Curry and Knott showed [155, 191] that in normalized and annealed mild steels there is a

general relationship between grain size and the largest grain-boundary carbide width. Confirming that lack of grain size dependence on Smiths model is overcome by an increase in the carbide thickness with increase in grain size. Okumura [192] measured σ_F values of steel where carbide and grain sizes variations are independent, thus concluded that regardless of increasing fracture resistance for fine-grain sizes, the effects of grain-boundary carbide size on cleavage fracture is the principal factor controlling the fracture stress.

Weld metals have different initiators for cleavage than those in wrought steels. A model was proposed by Tweed and Knott [7] for cleavage fracture in the AD microstructure of C-Mn weld metal after non-metallic inclusions were found to act as a cleavage microcrack initiator within this microstructure. McRobie [52], Novovic [13], Wenman [14] and do Patrocinio [15] showed that a large variety of inclusions are responsible for cleavage fracture initiation. Research carried out on pearlitic steel [193-195] showed that the nuclei for cleavage fracture could be a microcrack or small oxide inclusion, nucleating across numerous pearlitic carbides. Also different variations in toughness within the weld metal are known to occur due to inclusion population, which contains oxides formed during the deoxidation process. More recent studies have shown that the most important factor influencing toughness [7, 10, 13-15, 52] is the microstructure. Within weld metals inclusions are associated with initiation which is fibrous in nature through the coalescence of voids around them. Detailed examination of these inclusions could not find any clear differences in the chemical composition of the “void-initiating” and “crack-initiating” inclusions. Knott [113, 196] rationalised that there could be subtle differences and these could be associated with a sulphide shell around the inclusion. More recently, Miao [76] showed that C-Mn weld metal contained large “patches” of sulphide, resulting from the application of different cooling rates, these generally seem to have higher fracture toughness than the same material with fewer patches, it was also noted that there were differences in the cleavage initiation modes, these may have arisen from different inclusion surface features.

Weld metals are treated with warm prestressing (WPS), because after this operation the distribution of cleavage fracture initiators changes. Reed and Knott [113, 197, 198] used

A508 weld metal and showed that after WPS treatments the low-temperature fracture load/fracture toughness increase, this was primarily due to the compressive residual stress distribution generated during the WPS, also it is associated with the change in nature of the fracture initiation sites. When looking at specimens that were not treated with WPS, initiation sites corresponded to the largest inclusion in a “well-behaved distribution”, whereas for WPS specimens they are associated with inclusions with a size close to the mean of the size distribution, large inclusions were observed to have voids around them. It was concluded that during WPS treatments the inclusion matrix interface for large inclusions was decohered at low levels of strain, thus they could not act as cleavage initiation sites following low temperature fracture. Under these condition fracture need to be initiated by a smaller inclusion without interface decohesion so that statistically determined critical distance X_0 in the Ritchie, Knott and Rice (RKR) [199] model is also changed in comparison to the non WPS specimens.

As shown in Fig. 3.23 if cleavage fracture occurs after ductile crack growth, the inclusions in the weld material may not be the cleavage initiator. This is due to the fact that local conditions under which cleavage fracture begins, ahead of a blunted crack tip are not the same as those ahead of a sharp crack at low temperature because the plastic strain distribution ahead of the crack-tip is different in both cases. In the former case the plastic strain over a large distance is very high so that any likely inclusion microcrack nucleus produced near the yield-point strain would be blunted to become a non-virulent crack nucleus for cleavage fracture, see Fig. 3.23(c) and 3.23(d). Knott [113] therefore suggested that any microcrack nucleus would have to be newly formed in a conceptually different set of particles. Zhang and Knott [200-202] also demonstrated that ahead of a fibrous growing crack, voids formed around inclusions and cleavage is nucleated between inclusions, probably on MAC products.

3.3.2 The Ritchie-Knott-Rice Model

Ritchie-Knott-Rice (RKR) [203] used experimental data from blunt notched four-point bend specimens for values of σ_F and combined these with crack tip stress fields obtained from a finite element solution (i.e. stress-strain distribution ahead of a sharp crack [204] or blunt notch [163]). The objective was to incorporate micro-scale fracture properties, e.g. cleavage fracture stress σ_F and the characteristic distance X_0 , into the prediction of fracture toughness parameters (J, CTOD and K_{IC}) has been made as cleavage fracture is stress controlled. Measurements were obtained for K_{IC} for high-nitrogen mild steel, using conventional fracture toughness methods. Consistency among the results was obtained for a characteristic distance, equal to two grain-diameter, Fig. 3.24. The RKR fracture criteria model can be combined with fracture mechanics analyses to derive a general expression for cleavage fracture toughness, K_{IC} :

$$K_{IC} = \beta^{-\left(\frac{n+1}{2}\right)} X_0^{\frac{1}{2}} \left[\frac{\sigma_F^{\frac{(n+1)}{2}}}{\sigma_{ys}^{\frac{(n+1)}{2}}} \right] \dots (3.43)$$

where β is the amplitude of the RKR stress singularity

σ_{ys} is the yield stress

n is the strain hardening exponent.

Therefore from the knowledge of microscopic parameters, X_0 , n , σ_F and σ_y and considering these are temperature independent, the microstructural, temperature and strain rate dependence of the fracture toughness in steels can be estimated. X_0 should be empirically determined.

3.3.3 Statistical Approach (RKR) model

Curry and Knott [158, 191] investigated the grain size dependence of the characteristic distance X_0 . There was no simple relationship of significance found between the two parameters, as shown in Fig. 3.25, it can also be seen that the characteristic distance is about four times the grain size, this applies to grain diameters greater than $40\mu\text{m}$. Based on carbide size, Curry and Knott proposed a probabilistic model to predict fracture toughness, K_{IC} , this followed on from their modification on the RKR model:

$$K_{IC} = \sigma_{ys} \bar{r}^{\frac{1}{2}} Y \quad \dots (3.44)$$

where \bar{r} is the mean particle radius and Y is dimensionless number derived from carbide particle and crack - tip stress distribution. Curry and Knott's [158, 191] modification and the RKR model are of the same form.

In order to find a particle larger than the critical size that will nucleate cleavage the characteristic distance is used as a measure of the material volume. In a testpiece containing a sharp crack, the critical size of the cracked carbide varies with the distance from the crack-tip due to the stress gradient ahead of the sharp crack, in other words larger particles will need lower stresses to nucleate cleavage and vice versa. Thus fracture is controlled by a statistical competition among crack nuclei of varying frequencies and sizes. It has been suggested for blunt notched testpieces, the largest cracked carbide particles will define the microscopic fracture stress because of the absence of a microstructurally significant stress gradient and large sampling volume. From the carbide size distribution and the relationship with carbide size and the microscopic cleavage fracture stress, they predicted fracture toughness values

which displayed good agreement with the experimental results obtained for quenched and tempered steel.

As a consequence of the work carried out by Curry and Knott into the effects of carbide size distribution on temperature dependence of fracture toughness many researchers have looked into the influence of cleavage crack initiators, which have found non-metallic inclusions or carbides to be the source, there has been a lot of research carried out into weld metals. Bowen used an A533B pressure vessel steel to examine the dependence of cleavage fracture stress, σ_F and fracture toughness K_{IC} for a wide range of microstructural conditions, it was noted that the experimental values obtained for the K_{IC} model were in poor agreement with those predicted for the RKR model.

3.3.4 The relationship between microscope cleavage fracture stress (σ_f^*) and macroscopic toughness parameter K_{IC}

Ritchie, Knott and Rice [203] first discovered the relationship between the microscopic parameter of cleavage fracture stress (σ_f^*) and fracture mechanics methodology. Rice and Johnson [204] had published a paper similar to Griffith and Owen concerning finite element analysis of a stress field ahead of a blunting crack, where as Griffiths and Owen [163] had used a blunt notch. It was postulated that unstable fracture happened when the stress intensification at the crack tip increased the value of the maximum principal tensile stress ($\sigma_{yy\max}$) to above that of microscopic cleavage fracture, σ_F . Also it was noted that the distance had to be included for the model to be dimensionally correct. “Characteristic” distance was thought to be microstructurally dependant and determined approximately by two grain diameters. The RKR model suggest both the fracture stress and the critical distance were independent of test temperature and thus temperature dependence of K_{IC} could be calculated from the materials variation of yield stress and working hardening rate in relation to test temperature.

3.4 Ductile Fracture

Ductile fracture has not been investigated as much as brittle fracture, as brittle fracture is generally regarded more potentially dangerous in engineering practice. The mechanism for ductile fracture is characterised by a rough fracture surface, showing cup-like depressions which are called microvoids, these are characterised by equiaxed, parabolic or elliptical in shape [40]. The mechanism of fracture is whereby the microvoids form and grow which then proceeds by localized internal necking of the material between the microvoids Fig. 3.26 [205]. As the load increases, necking continues and allows the ligaments between voids to fail linking up the microvoids (coalescence) such, the remaining ligament of material cannot support the applied load and thus final failure occurs [206-208]. Microvoids nucleate heterogeneously on hard second phase particles or at the grain boundary triple points in high purity metals. Generally, voids occur around particles which have very weak interfacial bonds, this occurs at strains close to zero, although well bonded particles may crack, thus forming void nuclei. Numerous authors have defined critical void nucleation stress (σ_c) as the sum of the mean local stress (σ_{loc}) and hydrostatic stress (σ_m) due to strain hardening in the vicinity of a second phase particle.

$$\sigma_c = \sigma_m + \sigma_{loc} \quad \dots(3.45)$$

this can be expressed as an average strain for void nucleation of ϵ_N

$$\epsilon_N^2 = H(\sigma_c - \sigma_m) \quad \dots(3.46)$$

where H is a constant

Conversely, it was concluded that the average nucleation strain, ϵ_N , did not describe accurately the real nucleation events, it was Iricibar [206] whom suggested that nucleation could be more accurately modelled by the knowledge of particle size and spatial distribution rather than an average strain level.

The mechanism of ductile failure combines both nucleation and growth of voids. Numerous researchers [205, 209, 210] have modelled the growth of voids during ductile failure, but it is the model by Rice and Tracey [211], which is mostly widely accepted and used. Their research modelled a single isolated void growing under the action of a triaxial stress state. The effects of work hardening on void growth by the replacement of yield stress by effective stress were included in the model. This model for void growth has been used and modified by many authors, except it does not describe failure where voids interact and coalesce. Ductile failures occur when plastic instability initiates localised bands of deformation between voids, these tend to be regions of high strain. A model for ductile failure was developed by Thomason [212], in which it was assumed that fracture occurs when the net section between the two voids reaches a critical stress level $\sigma_{n(c)}$.

Ductile crack is stable if:

$$\sigma_{n(c)} \frac{d}{d+b} > \sigma_1 \quad \dots (3.47)$$

thus fracture occurs if

$$\sigma_{n(c)} \frac{d}{d+b} = \sigma_1 \quad \dots (3.48)$$

where $2d$ is the distance between voids
 $2b$ is size of void in the direction of the stress,
 σ_1 maximum principal stress

3.5 Ductile-to-Brittle Transition Region (DBTT)

The ductile-to-brittle transition region is of major importance when selecting materials for engineering use. The philosophy of design is to select a material which exhibits sufficient notch toughness when subjected to rigorous service conditions so that the load-carrying ability of the structural member can be calculated by standard strength of materials criterion without considering the fracture properties of the material or stress concentration effects of cracks or flaws [40]. In the case of low and medium-strength BCC materials the transition region is very important, as notch toughness is strongly dependant on temperature. BCC metals show a strong temperature dependence of yield and shear stresses and this is reflected in ductile-to-brittle temperature.

Specimen geometry and hence stress also influence the DBTT greatly. For instance, a reduction of the specimen dimension significantly reduces the transition temperature due to the absence of a triaxial stress state. Conversely, the addition of a stress raiser (notch) significantly increases the transition temperature as the root of the notch introduces triaxial stress state.

In the previous section it has been extensively discussed that a critical value of principal tensile stress σ_F must be achieved at the critical distance ahead of the advancing stable crack for cleavage then to occur. Thus, if the stress level is not attained in the process zone the testpiece fails by plastic collapse or general yielding.

For Charpy impact tests, the transition region is characterised by “ductile thumbnail”, the initial growth of stable fibrous crack growth, before cleavage fracture occurs. The cleavage brittle to fibrous ductile transition behaviour in BCC metals can be explained by numerous reasons [113, 144, 213]:

1. Increase in the strain rate caused as a consequence of increasing the rate of ductile crack growth would be sufficient to increase the local tensile stress ahead of the crack tip above the critical cleavage fracture stress and hence cleavage fracture proceeds.
2. In the situation of heterogeneous materials such as weld metals, the ductile crack grows across different microstructures within the weld material. Therefore the process zone ahead of the crack samples regions with different toughness, therefore a region of low toughness is within the process zone. Thus the critical tensile stress for cleavage failure may then be exceeded for this brittle region and a crack could appear. Although, if the tougher material surrounding the crack is not able to arrest, then catastrophic failure will ensue. The brittle region within the weld could be characterised by a region of large grains, coarser hard cracked particles or any discontinuity, making cleavage fracture in heterogeneous materials a statistical process.
3. If we consider a testpiece with a stress-raising defect in it, or a notch, under applied tensile stress, the notch begins to open and ductile tearing begins at the root. This region just below the notch can form a crack, and therefore sharpen the crack, thus increasing the levels of stress in the specimens. The sharpening of the notch root depends strongly on the strain hardening coefficient of the material, n . Low values of n result in a sharpened fibrous tip, whereas high values of n lead to a blunted ductile crack tip. Cleavage fracture of a catastrophic nature is more likely to occur and be aided by the first situation.

3.6 Intergranular Failure

When considering the transition region it is important not to ignore fracture that occurs by intergranular micromechanisms. Both brittle fracture and fibrous microvoid coalescence can occur intergranularly in a manner similar to transgranular crack growth. Intergranular failure is associated with alloy element segregation to grain boundaries, thus reducing the cohesive strength of the material. In high-strength forging steels intergranular fast fracture has been known to occur down the prior austenite grain boundaries due to their embrittlement by minor impurity elements such as phosphorus and sulphur, this segregation mechanism can lead to a low energy crack path for fracture to follow [214, 215].

Transition to intergranular fracture from transgranular fracture has been observed and often accompanied by a significant reduction in fracture stress. A modified Griffith equation can be used to explain the transgranular fracture as for transgranular cleavage fracture stress if γ_p is replaced by γ' :

$$\gamma' = 2\gamma_s - \gamma_B + \gamma_p \quad \dots (3.49)$$

where γ_p and γ_s are the same for cleavage fracture and γ_B is the negative term associated with separation of grain boundaries. Impurity segregation reduces both fracture stress and γ' values. The process of brittle intergranular fracture must include bond breaking, work hardening, dislocation motion and a description of how individual impurity elements reduce the strength of bonds, a greater understanding of this has been achieved through various models. It is possible for intergranular fracture to occur in a fibrous manner by the linking of voids around second phase particles, for this to occur the alloy must exhibit high density of weakly bonded second phase grain boundary particles, and show few particles intergranularly. Intergranular microvoid coalescence (MVC) is generally rare when operating at low temperatures, as MVC is a lower energy crack path that transgranular cleavage is not often

found. However occurrence of these failures can occur in “overheating” of low alloy steels, where a fine array of sulphide particles are distributed on the austenite grain boundaries leading to only local grain boundary plasticity, therefore low energy linkage of voids and particles.

Chapter 4 - Experimental.

4.1 Introduction

The Welding Institute (TWI) during the 1980's carried out an experimental programme for the Nuclear Installations Inspectorate (NII) to investigate the effects of several welding parameters: weld consumables (NiMo and NiCrMo), post weld heat treatments (both American and European practices) and the extremes of heat inputs of those envisaged in practice (lowest 2.6 kJ/mm and the highest 5 kJ/mm) [216]. Fracture toughness and Charpy impact tests were carried out using full thickness and small-scale COD specimens followed by metallographic examination. During the experimental procedure microstructural evaluation was only considered in notched COD specimens in the weld metal and HAZ regions. Recently extensive work has been carried out on C-Mn weld metal steel showing the microstructural effect on Charpy impact toughness in both an as-received and pre-strained condition [13]. Following on from this Wenmen [14] studied this effect on an as-received condition of an A533B weld and Patriocinio [15] studied the microstructural effect on Charpy impact properties of A533B Class 1 weld metal in the as-received, pre-strained, pre-strained and static strain aged conditions. As a result of these studies a programme was started to study the fracture toughness properties of MnMoNi weld metal, with similar composition to those use in the fabrication of Sizewell B, in the as-received and pre-strained and static strain aged conditions.

4.2 Experimental

4.2.1 Material

The material used in the study of this work was a MnMoNi weld metal produced by ESAB Group Plc and was commissioned by the Nuclear Installations Inspectorate Health and Safety Executive (NII HSE) in 2000. The weld was designed (i.e. base metal, welding process parameters and consumables where chosen) to produce a weld of similar characteristics to the start-of-life of the Sizewell B reactor pressure vessel (RPV). The composition of the weld material is presented in Table 4.1; however there are slight variations in composition, mainly in the copper content, due to the use of copper coated electrodes in the welding process and the welding parameters from the guiding procedures used during the construction of Sizewell B. The weld was accordingly deposited by a multipass submerged arc welding technique (SAW), using C-Mn parent plates. The welding parameters and post weld heat treatment are given in Table 4.2 and 4.3. The weld was supplied in the form of C-Mn plates, approximately 25mm thick and 150mm wide, in 500mm lengths. The weld preparation was “V” shaped with a 25mm base and a 60° bevel supported with a backing plate 12.5mm thick and 50mm wide. A digital camera image and a schematic diagram of an as-received (AR) weld metal piece are shown in Fig. 4.1. The macrostructure of the weld showing the welding sequence and size of the as-deposited beads and reheated regions are shown in Fig. 4.2 (Weld N°1) and 4.3 (Weld N°2). The macrostructure was revealed by taking transverse cross-sections which were ground sequentially on SiC papers to P1200 grade, polished on diamond wheels to 1µm and etched in a solution of 5% nitric acid and 95% ethanol. The weld microstructural regions after PWHT procedure are labelled AR here, Fig. 4.4.

4.2.2 Materials Plan

At the beginning of the project material was acquired from a previous experimental programme [15], therefore was limited in supply, and used for the initial assessment of crack-tip opening displacement (CTOD) values. An additional 10 meters of weld (20 pieces) were

fabricated (as the experimental programme expanded) to the same specifications as the initial weld metal. The batches were labelled as Weld N^o1 (for the original weld) and Weld N^o2 (for the New Weld). For the first weld batch, no attention was paid to individual weld piece labelling and therefore no record for individual specimen history exists. For the second weld batch, however individual pieces were coded and are referred to as Weld N^o2-I,, Weld N^o2-XX. Therefore the history of all specimens machined from this batch is known.

4.3 Thermo-Mechanical Heat Treatments

Mechanical and fracture toughness properties of the low alloy ferritic steel weld metal have been evaluated for both microstructures: as-deposited (AD) and reheated (RH) in two conditions, namely: as-received (AR) and 5% cold deformed and static strain aged at 300°C for 2h (5%SA). The thermo-mechanical heat treatments utilised in this study are described below.

4.3.1 Cold Deformation Procedure

Slices were removed from the as-received main weld run, and then subjected to a 5% nominal strain. These slices measured approximately 12mm in thickness. The cold deformation procedure was completed using a calibrated 3000 kN Dension Press, direction of the prestraining was perpendicular to that of the welding direction. The amount of plastic deformation was determined by measuring the thickness of the specimen both before and after the prestraining procedure at 3 different points. The samples are placed, one by one in between two anvils (extremely hard flat dies) with the top and lower surfaces lubricated with oil to reduce the frictional resistance between the surfaces which are in contact. The mean and standard deviation values were then calculated for each specimen, thus an average thickness measurement is quoted. The amount of plastic deformation was shown to be within

a constant range of $5\pm 0.6\%$. A schematic diagram of the cold deformation procedure is shown in Fig. 4.5.

This prestraining treatment was used on the weld metal to simulate potential effects of irradiation. It should be noted that the cold deformation process was applied to the weld blocks they and were subsequently machined into Charpy, crack-tip opening displacement and blunt notch test specimens works in compression. To avoid the Bauschinger effect [40, 41] the tensile specimens, were electro-discharge machined (EDM) from the weld blocks in the AR condition and plastically deformed in tension, then statically strain aged, before being tested at the desired temperature.

4.3.2 Static Strain Aged Condition

The pre-strained specimens from both the AD and RH microstructures were then thermally treated for 2 hours at $300\pm 15^\circ\text{C}$ using a Lenton vacuum tube furnace to protect the specimen surface from oxidation. The temperature of the heat treatment is similar to that of the normal operating inlet temperature of a PWR, which is approximately 290°C [6, 9]. The operating pressure of the Lenton vacuum furnace chamber during the treatment is $1.33 \cdot 10^{-4}$ Pa. These specimens are labelled as (5%SA).

4.4 Material Characterisation

4.4.1 Microstructural Analysis

The microstructure of the weld metal was examined by taking transverse cross-sections from the bulk material, Fig. 4.6. These were prepared according to a standard metallographic preparation route. Plane grinding of the samples was completed to remove damaged or deformed surfaces of the weld metal were plane ground on SiC papers to 1200 grit, fine

ground on 9 μ m diamond paste and then finally polished on 3 and 1 μ m diamond paste and etched in 2% Nital to reveal the microstructure of the weld. The microstructures were then photographed using a Carl Zeiss Axiolab optical microscope with digital image capture. Some of the micrographs taken were then used for grain size analysis by the linear intercept method, as well as using the KS-400 image analysis software to analyse phase area percentage [40, 217].

4.4.2 Inclusion Analysis

Inclusion analysis was carried out on both Weld N^o1 and Weld N^o2 for samples from each of the weld metal regions; AD and RH microstructures in the as-received (AR) and 5% strain aged (5%SA) conditions. The samples were mounted in resin, ground and polished. The unetched sections were observed and photographed using a Philips XL-30 scanning electron microscope (SEM) in the secondary electron mode using high contrast. Nine fields were sampled randomly without overlap for each sample; the pictures were analysed using KS-400 image analysis software. The inclusions appear as dark areas on a light grey background allowing the size and number to be measured for each photograph. An off-set inclusion diameter was used of 0.2mm; therefore inclusions under this size were not recorded. The spatial distribution of the inclusions were calculated using the following relationships [218]:

$$\frac{\bar{d}_v}{d_a} = \frac{\pi}{2} \quad \dots(4.1)$$

$$N_a = N_v \bar{d}_v \quad \dots(4.2)$$

$$N_v = \frac{6V_v}{\pi(\bar{d}_v)^3} \quad \dots(4.3)$$

$$S_v = \pi N_v (\bar{d}_v)^2 \quad \dots(4.4)$$

$$\lambda_v = 0.554 \left(\frac{1}{N_v} \right)^{\frac{1}{3}} \quad \dots(4.5)$$

Where \bar{d}_v is the arithmetic mean 3-D diameter

\bar{d}_a is the arithmetic mean 2-D diameter

N_a is the number of inclusions per unit of area

N_v is the number of inclusions per unit of volume

V_v is volume fraction

λ_v is the mean inclusion centre to centre volume spacing

S_v is the inclusion surface area per unit volume

Energy dispersive X-ray (EDX) was used to analyse the chemical composition of the inclusions, which was carried out using the Philips XL-30 SEM, using broken halves of the Charpy and CTOD specimens. During the qualitative chemical analysis, the electron beam was positioned at the centre of the inclusion. Working conditions were kept constant, i.e. accelerating voltage of 15 kV, 0° tilt and a working distance of 10mm.

4.4.3 Glow Discharge Spectrometry (GDS)

A LECO GDS-750 QDP Glow Discharge Spectrometer was used for GDS analysis. The machine, working a quantitative surface depth profile (QSDPA) programme, enables a rapid determination of the chemical composition profiles, i.e. composition in wt or at % vs. depth from the surface. The GDS machine has a depth limitation of approximately 100 μ m.

4.5 Hardness Tests

Both macro and microhardness testing were carried out to examine the effects of pre-straining and thermal ageing treatments (5%SA) compared with the as-received (AR) condition of both the AD and RH microstructures. Hardness measurement locations were chosen to correspond with the region of the weld sampled by Charpy, slow blunt notch tests and CTOD fracture toughness and tensile test specimens.

4.5.1 Macrohardness

An Indentec Hardness Testing machine was used for measuring macrohardness with an applied load of 20kg and a 10 second dwell time. Macrohardness profiles were taken to evaluate the effects of thermal cycles, from the multipass welding procedure. Three profiles were taken from both the AR and 5%SA conditions, starting from the parent plate material, crossed the heat affected zone (HAZ), as-deposited (AD) weld bead and reheated (RH) regions, shown in Fig. 4.7, the profiles were located according to where specimens are located in relation to the weld macrostructure. Hardness measurements were taken at intervals of 1mm and carried out on polished samples measuring 80x20x4mm, removed from the bulk material.

4.5.2 Microhardness

Microhardness measurements were performed using a Mututoyo MVK-H1 Microhardness testing machine, using an applied load of 50g and a dwell time of 10 seconds. Measurements were taken at 0.1mm intervals in the middle of the top weld bead in the AD microstructure, Fig. 4.8. A second trace was located close to the root of the weld within the RH microstructure. Microhardness measurements were taken in both the AR and 5%SA conditions.

4.6 Tensile Tests

Tensile testing was completed using a Zwick 1484 Screw Driven Machine with a 200 kN load cell, at a cross displacement speed of 0.5mm/min. Low temperature testing (-196 to -20°C) was completed using an insulated low temperature bath. Liquid nitrogen was used to achieve a temperature of -196°C. Temperatures -160 to -20°C were obtained by allowing liquid nitrogen to boil off. Specimens were “submerged” in the required medium or vapour until the necessary temperatures were reached and stabilised within $\pm 3^\circ\text{C}$. Test temperatures were monitored by attaching a thermocouple in the vicinity of the specimen gauge length. Except for the room temperature tests (where an extensometer was used), the elongation of the specimens was calculated from the cross-head displacement.

Load versus displacement curves were converted into engineering stress-strain curves and plotted for individual tests. An extensometer was attached to specimens tested at room temperature to achieve calculations of 0.2% yield stress, $\sigma_{y0.2\%}$ and Young’s Modulus of elasticity (E). Following testing these values were obtained through expressions of the type;

$$s = \frac{P}{A} \quad \dots(4.7)$$

and,

$$e = \frac{\Delta L}{L_o}, \quad \Delta L = L_f - L_o \quad \dots(4.8)$$

where s is the engineering stress.

P is the applied load.

A is the area under fracture.

e is the engineering strain.

ΔL is the increase in gauge length.

where σ_{TS} and $\sigma_{y0.2\%}$ can be obtained using maximum load and load at 0.2% strain respectively. True stress-strain values were achieved using the following relationships

$$\sigma = s(e + 1) \quad \dots(4.9)$$

and

$$\varepsilon = \ln(e + 1) \quad \dots(4.10)$$

where the work hardening exponent (n) values can be obtained using the simple power curves relationship (Holloman's equation) for strains up to the tensile strength [41];

$$\sigma = K\varepsilon^n \quad \dots(4.11)$$

where σ is true stress.

ε is true strain.

K is strength coefficient.

n is the work hardening exponent.

Due to the extent of the tensile testing programme a test matrix was required, this detailed orientation, microstructure geometry and test temperatures, shown in Table 4.4. Fig. 4.9 details the tensile test specimen geometry and Fig. 4.10 illustrates where specimens were removed from in relation to the microstructure. It should be noted that different tensile specimen geometry were used due to the size of the weld metal being sampled for Weld N^o1 and Weld N^o2 for the mixed microstructure condition only, Fig. 4.11 shows the specimens unbroken. Even so, the location of a tensile gauge length uniquely into a single microstructure is difficult.

4.6.1 5% Plastically Deformed and Strain aged at 300°C

For the 5% plastically deformed and strain aged tensile specimens, these were deformed in tension at room temperature up to a nominal plastic deformation of 5% and then unloaded. The elongation of 5% was measured using an extensometer attached to the tensile specimen. The specimens were then placed in the vacuum furnace at 300±15°C, the specimens were tested within one week to avoid the possible effects of natural ageing on the flow properties, previous research showed this could be an effect [15]. Also it should be noted that the new gauge length and area after the 5% plastic deformation procedure were used to determine the engineering stress-strain curves. These tensile specimens samples individual microstructures (AD and RH), were tested across the temperature range of -160 to -40°C.

4.7 Charpy Tests.

Ductile-to-brittle transition temperature (DBTT) curves have been established over a temperature range of -196 to 200°C in order to determine the ductile to brittle transition temperatures of the materials investigated based on two criteria; (i) the T_0 , transition temperature, which is a location parameter defined by fitting the obtained DBTT curve with a Tanh curve, and (ii) the transition temperature, T_1 , in relation to the onset of upper shelf (100% microvoid coalescence). The causes of failure have also been examined over the test temperature range.

Charpy impact testing was performed according to British Standard BS 131: Part 7: 1989 [219] using Charpy specimen with the dimension of 10x10x55mm³. A Charpy V notch inclusive angle of 45° a depth of 2mm and a root radius of 0.25mm was machined at the centre of the specimen, as shown in Fig. 4.12.

Charpy impact testing was completed using a 300 J Instron PW30 Charpy Machine calibrated accordingly to BS 131: Part 7: 1989 [219], at temperatures in the range of -196 to 200°C. The specimen was located on the anvil and impacted by a hammer where the difference in the potential energy before and after fracture was recorded as the energy absorbed, see Fig. 4.13. Different test procedures were employed for Charpy tests below room temperature and at elevated temperatures. Test temperature were achieved using mediums of liquid nitrogen (-196°C), and a mixture of methanol and liquid nitrogen (-100 to -20°C) ice water (0°C). These temperatures were measured using a thermocouple attached to the specimens so that the temperature could be monitored within $\pm 2^\circ\text{C}$, which was attached closely to the notch root of the specimen. Specimens were submerged in the medium for 15 minutes to ensure temperature stabilization throughout the whole section before testing, which was then carried out within 5 seconds of the specimen being removed from the medium. For tests carried out at elevated temperatures, a BLT (B. S. 2648) furnace with a Eurotherm temperatures

controller was used; transfer was carried out with 5 seconds in line with the standard procedure [219].

After fracture, the broken specimen halves were washed in acetone and later removed for fractographic examination. Fracture surfaces were measured and photographed using a Lecia VMZ 50 light microscope with attached measuring stage. In addition to the impact energy absorbed by fracture the specimens and several other properties were measured on the fracture surface, Fig. 4.14; including cleavage area (percentage of crystallinity) CA, lateral expansion on the compression side of the specimen, LE, ductile thumbnail size, DT and shear lip, SL:

- Ductile thumbnail size is defined as depth of ductile fracture area below the notch root;
- Cleavage area is defined as a total area of crystalline portions on the fracture surface, expressed as a percentage of the original cross-section area of the specimen below the notch (80mm^2);
- Lateral expansion is defined as a difference between the increased thickness (defined as the height in standard [117] -the vertical dimension of the specimen when placed in the testing position) due to distortion at the position of impact by the pendulum hammer and the original specimen thickness (10mm);
- Shear lip size is defined as the maximum dimension of the shear lip in the thickness direction. The average shear lip is the average measured for the two shear lips on the fracture surface.

Sigmaplot was used to plot the absorbed energy (J) values against the corresponding temperature ($^{\circ}\text{C}$). Hyperbolic tangent curves (Tanh) were weight fitted to these data using non-linear regression analysis. Values of ductile-to-brittle transition temperature (DBTT) for each of the microstructure and as-received and strain aged conditions were compared, hence temperature shifts were obtained. Hyperbolic tangent curves fitted to each set of data using an expression of the type:

$$E = A + B \tanh\left(\frac{T - T_0}{C}\right) \quad \dots(4.12)$$

where A,B are constants, (A+B equals the upper shelf energy and A-B equals the lower shelf energy)

T is dependant variable of test temperature

T₀ is a location parameter defining the curve on the temperature axis

C is a constant defining the shape of the curve in the transition region.

The main stages in the regression model are as follows:

- fitting Charpy impact energy data for specific combination of material (weld);
- determination of the temperature T_{40J}, for the as-received and strain-aged conditions (from individual fitted curves) and calculation of ΔT_{40J} for a particular combination of conditions.

Two potential drawbacks were identified with the above approach, one in relation to the methodology and the other to the choice of curve itself. The DBTT was then defined at the 40J energy levels in the evaluation procedure using the data obtained from the Charpy Impact tests.

Ductile thumbnail extensions (DT) in the DBTT can be estimated at the 40J energy level for the weld microstructural conditions in the AR and 5%SA conditions through the curve fitting

procedure of the ductile thumbnail versus absorbed energy data using linear regression of the general form:

$$C_{V(40J)} = y_0 + a(DT) \quad \dots(4.13)$$

thus

$$DT = \frac{C_{v(40J)} - y_0}{a} \quad \dots(4.14)$$

where y_0 and a are constants and $C_{V(40J)}$ is the absorbed energy value at the 40J level.

4.8 Slow Blunt Notch Bend Tests

The approach utilized here uses the FEM elastic-plastic stress analysis of Griffiths and Owen [163] for the finite element (FEM) calculations of the stress and strain fields surrounding a blunt notch. This analysis estimates the maximum principal tensile stress ($\sigma_{yy\max}$) ahead of the notch root essential to promote cleavage fracture in steels. Specimen of two sizes were tested; Charpy size specimens ($10 \times 10 \times 55 \text{mm}^3$) dimension with a notch geometry of one third of the specimen width (3.33mm depth) and 0.25mm root radius and specimens matching the original sample size of ($12.7 \times 12.7 \times 75 \text{mm}^3$), with a notch depth of 4.33mm and a root radius of 0.25mm are detailed in Fig. 4.15 [220]. The notch is one third of the specimen width ensuring general yield plastic deformation occurs across the minimum section; the notches were EDM machined precisely to prevent any plastic deformation prior to testing. Testing was performed in four-point bending as illustrated in Fig. 4.16 and in an insulated low temperature bath. The tests were carried out at -196°C to allow the specimen to fail prior to general yielding. Desired test temperatures were achieved using liquid nitrogen -196°C . Temperature was monitored by attaching a thermocouple into a drilled hole, which was

located mid-section of the specimen, 3mm from the notch root to allow for metal-metal contact. The specimen was held at required temperature for at least 15 minutes and controlled within $\pm 3^\circ\text{C}$, prior to loading at a cross-head displacement rate of 1 mm/min. Tests were carried out using a screw-driven Denison Mayes machine with a 50 kN load cell. The nominal stress, σ_{nom} , was obtained from the tests as described below [163].

$$\sigma_{nom} = \frac{6M}{B(W-a)^2} \text{ and } M = \frac{PL}{2} \quad \dots(4.15)$$

Where M is the bending moment calculated in three or four point bending

L is the difference between the inner and outer rollers

P is the fracture load

B is the specimen thickness

W is the specimen width

a is the notch depth

$\frac{\sigma_{nom}}{\sigma_y}$ ratio obtained at -196°C from yield strength values allows the appropriate ratio of the largest values of the maximum principal stress ($\sigma_{yy\max}$) to the yield stress, from the results of the FEM analysis the stress intensification factor R can be determined from Fig. 3.22, thus the maximum principal stress, $\sigma_{yy\max}$, can be calculated by:

$$R = \frac{\sigma_{yy\max}}{\sigma_y} \quad \dots(4.16)$$

$\sigma_{yy\max}$ values compare to the values σ_{x0} and σ_F^* , where σ_{x0} is the calculated stress at the position of a cleavage fracture initiation site (CIS), found from the FEM analysis $\sigma_{yy\max}$ from the plot of maximum stress versus distance from the notch root at various loads, Fig. 4.17, σ_F^* is the calculated stress for an initiation inclusion site found by the CIS predicated by the modified Griffith type equation for a penny shaped crack.

$$\sigma_F^* = \left[\frac{\pi E \gamma_p}{(1 - \nu^2) d} \right]^{\frac{1}{2}} \quad \dots (4.17)$$

Where E Young's Modulus

d is the diameter of the initiation inclusion

ν is Poisson's ratio

γ_p is the effective surface energy

4.9 Crack Tip Opening Displacement (CTOD)

CTOD is an elastic-plastic fracture mechanic parameter used to characterise the fracture process, the specimen dimensions used in the study were prohibitively small to allow the determination of valid plane strain fracture toughness, K_{IC} values. CTOD tests were performed in accordance to the procedure described in BS 7448: Part 1: 1991 [149] and BS 7448: Part 4: 1991 [161], on a Dension Meyes Group, DMG machine fitted with a 50 kN load cell.

4.9.1 Test Specimens

Specimens measuring $13 \times 25 \times 80 \text{mm}^3$ were cut and machined from the bulk material; the specimen size was reduced to square cross-sectional bend specimens of nominal dimensions of $10 \times 10 \times 55 \text{mm}^3$ (pre-cracked Charpy specimens) Fig. 4.17. After cutting (similarly to the Charpy impact test specimen with the transverse notch orientation) the full transverse cross-sections had to be etched to reveal the macrostructure before the specimen location could be marked at the desired position and the specimen then machined to its final dimensions. Two specimen locations relative to the weld were selected in such a way that the fatigue precrack tip sampled either the AD or RH region. A notch was machined at the centre of the specimen, for the AD region, the notch was located within the largest weld bead at the centre of the specimen. Notch orientation relative to the weld and schematic representation of the specimen sampling AD and RH microstructure, is shown in Fig. 4.18.

4.9.2 Fatigue Precracking

Fatigue precracking was carried out on specimens at room temperature using an Amsler Vibrophore machine with a 20kN capacity. The maximum fatigue precracking force (F_f) during precracking extension was lower than 4.2kN, with the maximum stress intensity factor (K_Q) not exceeding $20 \text{MPa}\sqrt{\text{m}}$. K_Q was calculated using the following equations [149, 161, 221];

$$K_Q = \frac{PS}{BW^{1.5}} f\left(\frac{a_0}{W}\right) \quad \dots(4.18)$$

and

$$f\left(\frac{a_0}{W}\right) = \frac{3\left(\frac{a_0}{W}\right)^{0.5} \left[1.99 - \left(\frac{a_0}{W}\right) \left(1 - \frac{a_0}{W}\right) \left(2.15 - \frac{3.93a_0}{W} + \frac{2.7a_0^2}{W^2} \right) \right]}{2 \left(1 + \frac{2a_0}{W} \right) \left(1 - \frac{a_0}{W} \right)^{1.5}} \quad \dots(4.19)$$

Where $f\left(\frac{a_0}{W}\right)$ is a compliance coefficient for a three-point bend specimen

P is a relevant load used in the fatigue precracking procedure

S is the span between out loading points

B and W are the specimen thickness and width respectively.

The load ratio used was:

$$R = \frac{P_{\min}}{P_{\max}} = 0.1 \quad \dots(4.20)$$

where P_{\min} and P_{\max} are the minimum and maximum loads applied over the fatigue load cycle respectively.

4.9.3 Potential Difference Technique

The potential difference technique was used to measure the status of the fatigue precrack. Wires were spot welded either side of the notch [222]. The fatigue precrack was initiated and extended from the notch and grown to a corresponding length of $\frac{a_0}{W} = 0.45 - 0.55$. Current was applied through crocodile clips which were attached to either end of the specimen,

providing an initial voltage of $100\mu\text{V}$. Variation in voltage was then used as an indication of the extension of the fatigue crack, using the following polynomial curve fitting equation

$$\frac{a_i}{W} = f\left(\frac{V_i}{V_0}\right) = 0.0212\left(\frac{V_i}{V_0}\right)^3 - 0.1365\left(\frac{V_i}{V_0}\right)^2 + 0.3567\left(\frac{V_i}{V_0}\right) - 0.0374 \quad \dots(4.21)$$

relating to the decreasing notch cross-section due to the crack extension as a consequence of increasing voltage. The equation was obtained through using replicas on both sides of randomly selected specimens to measure the crack extension relative to a specific voltage across the notch, during the fatigue precracking.

4.9.4 Testing

CTOD testing was performed on the fatigue precracked sample on a DMG machine fitted with a 50kN load cell and testing was carried out in accordance with BS 7448 Part 1: 1991 [149]. Samples were tested using a three-point bend configuration with a 40mm span, the cross head displacement was 1mm/min, with the clip gauge seated on external knife edges, shown in Fig. 4.19. Tests were carried out over a range of temperatures from -196 to 20°C , to achieve low temperature the testing configuration was placed in an insulated bath and filled with liquid nitrogen, and cooled in the vapour from the boiling liquid nitrogen. The temperatures were monitored using a thermocouple placed in contact with the specimen surface within 2mm of the fatigue precrack tip and controlled to within an accuracy of $\pm 2^\circ\text{C}$.

After the specimens have fractured, the fracture surfaces were examined to determine the fatigue pre-crack length and the amount of stable crack growth preceding brittle fracture. The fatigue pre-crack original crack length, a_0 , was measured at nine equally spaced positions

along the pre-crack front. This is obtained by averaging the two outer points' measurements and then averaging the seven inner points, Fig. 4.20, [149, 161, 221].

CTOD values were calculated using the following expression [149, 161]:

$$\delta = \left[\frac{3.P.S_1}{B.W^{1.5}} \cdot f_0 \left(\frac{a_0}{W} \right) \right]^2 \frac{(1-\nu^2)}{2\sigma_{YS}E} + \frac{0.4(W-a_0)V_p}{0.4W + 0.6a_0 + Z} \quad \dots(4.22)$$

where P load

B thickness of specimen

W width of specimen

S₁ loading span

ν Poisson's ration

σ_{YS} 0.2% proof stress temperature of the fracture toughness test

E Young's modulus

a₀ original notch length

Z distance of clip-gauge location above the surface of specimen

V_p plastic component of the clip gauge opening displacement

$f_0 \left(\frac{a_0}{W} \right)$ Walker and May compliance function

For three point bending using an overall span to specimen width ratio $S(=2S_1)W$ of 4:1. The stress intensity factor $f_0 = \left(\frac{a_0}{W}\right)$ is defined as:

$$f_0\left(\frac{a_0}{W}\right) = 1.93\left(\frac{a_0}{W}\right)^{0.5} - 3.07\left(\frac{a_0}{W}\right)^{1.5} + 14.53\left(\frac{a_0}{W}\right)^{2.5} - 25.11\left(\frac{a_0}{W}\right)^{3.5} + 25.80\left(\frac{a_0}{W}\right)^{4.5} \dots(4.23)$$

Depending on the load versus clip gauge displacement and the amount of stable crack growth, Δa , prior to brittle fracture, the following notations are used for CTOD, and defined in BS 7448 Part 1: 1991 [149]:

- δ_c - critical CTOD at the onset of brittle crack extension when Δa is less than 0.2 mm;
- δ_u - critical CTOD at the onset of brittle crack extension when Δa is equal to or greater than 0.2 mm;
- δ_m - value of CTOD at the first attainment of a maximum force plateau for fully plastic behaviour.

4.10 Fractography

Charpy impact specimens fractography was performed on one broken half of the selected specimen which were tested in the lower and upper shelf energy regions, as well as in the transition region. Selected halves of tensile, fracture toughness specimens were also analysed, whilst both halves of the blunt notch specimens were examined. Fractography was carried out using an Philips XL-30 SEM, Jeol 6060 SEM and an Hitachi-4000S FEG SEM at an accelerating voltage of 20 kV and 0° tilt.

When utilizing energy dispersive x-ray microanalysis (EDX) an accelerating voltage of 15 kV was used to improve the clarity of the inclusion analysis. Specimens exhibiting brittle fracture were examined for cleavage initiation sites (CIS), these were located by tracing the macro and microscopic river lines characterising the fracture surface. Once a site was located measurements were taken of the distance from the pre-crack (CTOD) or blunt notch root (where relevant) together with the sizes of the group of the cleavage facets were made for an estimation of σ_{X0} values.

Groups of cleavage facets were defined subjectively, as individual facets were not precisely measured because it can be difficult to determine the facet boundary clearly. Facets were delineated by “eye” and the facet size was measured using Zeiss KS3000 3.0 image analysis software, calculating the minimum and maximum dimension of the facet, as well as its area. From the area information an equivalent diameter (Feret’s diameter) was calculated by considering the facet to be circular in shape.

Chapter 5 - Results - Materials Characterisation.

5.1 Introduction

Chapter 5 presents the results for material characterisation, glow discharge spectrometry (GDS) and hardness testing of the weld metals were obtained for the different microstructures; AD and RH microstructures and for the as-received and strain aged conditions: AR and 5%SA.

Characterisation of the microstructural features, i.e. percentage phases, grain sizes and inclusion distribution/composition of the weld were accomplished through metallographic examination of the AD and RH regions for the weld metals and conditions above. It should be noted that measurement of microstructural phases in the AD microstructure was difficult due to the mixture and the characteristic nature of different forms of ferrite (allotriomorphic, Widmånstatten and acicular).

Glow discharge spectrometry was utilised to assess the chemical (weight %) composition of both the supplied welds. Hardness variations were assessed in the microstructure and thermo mechanical treatments of both welds, as well as profile variations relating to sample locations.

5.2 Results

5.2.1 Microstructure

An example of the macrostructure of the multipass submerged arc weld for Weld N^o1 and Weld N^o2 are shown in Fig. 4.2 and 4.3 respectively. Both weld metal materials consist of two distinctive microstructure: as-deposited, AD and reheated, RH, as well as the parent plate microstructure, PP. Shown in Fig. 5.1-5.4 are micrographs and SEM images for the PP (Fig. 5.1), AD (Fig. 5.2) and RH (Fig. 5.3 and 5.4) microstructures for Weld N^o1. Micrographs and SEM images are shown in Fig. 5.5-5.8, for the PP (Fig. 5.5), AD (Fig. 5.6) and RH (Fig. 5.7-5.8) microstructures.

Twenty beads were deposited in order to fill the joint and the grain structure clearly indicates the solidification direction. The joints were filled with variable degrees of overlapping beads, which result in variable welding geometry and different degrees of refinement. In all the weld pieces for both weld metals, three beads dominate the top layer, the AD microstructure, which are elongated ferrite grains formed at different staged of cooling, consisting of a mixture of allotriomorphic ferrite α_{all} , acicular ferrite α_{ac} and Widmännstatten ferrite α_w , as well as small quantities of microphase microconstituents, M-A-C, Fig. 5.9. The RH microstructure consists fully of equiaxed ferrite grains which originate from the annealing process that occurs during the multipass submerged arc welding procedure (SAW).

The mean grain size measurement for Weld N^o2 was 20 μ m with the actual grain size varying between 8.4 μ m and 45.3 μ m for the RH microstructure and no significant difference in these grain sizes were noted after 5% plastic deformation and static strain ageing. It should be noted that the RH microstructure for Weld N^o1 was measured as part of a previous study and research programme [15], the mean grain size was 11.1 μ m, with a minimum and maximum values of 9.4 and 12.8 μ m. Also the grain size measurements for the RH microstructure were performed in the 'sampling area' for the different specimens used throughout this work,

corresponding to the weld region at the bottom of the weld cross-section. Due to the nature of the AD microstructure the grain sizes cannot be measured or analysed by the linear intercept method. The parent plate, coarse RH and fine RH regions of the weld metal (Weld N^o2) were analysed using KS 3000 software measuring the ferrite min and max, as well as the D circle and area of the grains. The parent plate area ranged from 210 to 289 μm^2 compared with 65 to 153 μm^2 and 23 to 93 μm^2 for coarse RH and fine RH respectively.

The elongated ferrite grain structure in the AD weld metal ranged in size from 130 to 220 μm for both Weld N^o1 and Weld N^o2, this was distinguishable by the naked eye on the fracture surfaces. The results of the measured area percentage of the different morphologies within the AD microstructure for both Weld N^o1 and Weld N^o2 lie within the range 46 to 58% acicular ferrite, 3 to 20% Widmännstätten and 33 to 42% for grain boundary ferrite. Similar results were exhibited by the corresponding strain and aged condition samples.

5.2.2 Inclusion Analysis

Polished samples of weld metal (Weld N^o2) were used to obtain a typical distribution of inclusions. Samples were observed from both microstructures (AD and RH) and in both conditions (AR and 5%SA), as shown in Fig. 5.10. From the observations and measurements carried out the results showed that the AD and RH microstructures presented similar 2-D modal diameter values of 0.53 and 0.48 μm , respectively, and overall mean volume fraction and diameter values of 1.76% and 0.5 μm , respectively, as shown in Table 5.1 and Fig. 5.11. Hence, no clear difference has been noted in the size of distribution of non-metallic inclusions between the two weld metals. The AD5%SA had a diameter of 0.59 μm , a slight increase compared to the AR condition, whilst the RH5%SA condition observed a slight decrease, 0.45 μm . Results within the microstructural conditions are fairly consistent (Table 5.2), implying the size distribution is relatively unaffected by the multipass SAW welding procedure and strain ageing.

Inclusion diameters carrying from 0.8 to 1.2 μm may be considered as the upper end of this distribution, hence if these are considered as a reliable representation of the overall inclusion size distribution within the bulk weld metal then inclusions greater than these will represent less than 1%. From the experimental data it would indicate that the 95th percentile of measured inclusion diameters is 0.8 to 1.2 μm , which is lower than previous data obtained for Weld N^o1 of 1.0 to 1.5 μm (part of a previous experimental programme [15]) and lower than 2.0 to 2.25 μm found by Knott [113, 223] and Curry and Knott [155] for C-Mn weld metals of a similar confidence level. Those inclusions are produced as a result of deoxidation processes that occur within the weld pool and it is reasonable to assume a smooth, well behaved inclusion size distribution.

5.2.2.1 Inclusion Chemical Analysis

X-ray spectra analysis is only a qualitative approach since the relative size of the peaks may vary between inclusions as well as from point to point within an inclusion. Energy dispersive x-ray (EDX) analysis was carried out on all four microstructural conditions; ADAR, RHAR, AD5%SA and RH5%SA, shown in Table 5.3 and Fig. 5.12-Fig. 5.15, respectively. Results indicated there was no significant difference in the inclusion chemical composition for the microstructures, although 'large' inclusions ($\geq 3\mu\text{m}$) and 'small' inclusions ($\leq 1\mu\text{m}$) show differences in chemical composition. The highest peaks for the majority of the EDX spectrums indicate Fe, Cr, Co and Mn constituents. The lower (background) peaks indicated Al, Ti, C, N, N, and Cu constituents. EDX detected oxygen within some of the inclusions, therefore it can be inferred these inclusions are a mixture of oxides and/ or silicates, iron aluminium and carbon are also traced within the inclusions. Inclusions also contain iron and aluminium and traces of carbon and sulphur. Sulphur may be present as a coating of the manganese sulphide surrounding the central oxide/ silicate core [224].

The elements were divided into major and minor constituents, based on their peak height to facilitate comparison, after Tweed and Knott [7]. A dividing line at approximately 30% of the maximum peak was chosen. The principal difference between large and small inclusions is

the presence of Cobalt and a reduction in manganese in inclusions less than 3 μ m. Cobalt is not present in the chemical composition Table 4.1, although from the GDS results carried out on this material; traces were found within the parent plate and HAZ with a reduction in the weld metal, Table 5.5-5.6.

5.2.3 Glow Discharge Spectrometry (GDS)

Glow discharge spectrometry was applied to both Weld N^o1 and Weld N^o2 to compare the chemical composition to that supplied from ESAB. Table 5.4 lists the chemical composition supplied for Weld N^o1, the chemical elements of greatest interest for the GDS analysis are indicated in yellow. The results from the analysis are shown in Tables 5.5-5.6 and plotted in Fig. 5.16-5.17 for Weld N^o1 and Weld N^o2 respectively. It should be noted that individual microstructures could not be assessed due to the nature of GDS so it was applied to the parent plate and the weld material. Measurements are taken to a depth of 100 micrometers, with a resolution of <0.025nm.

Mo, Mn, C, Ni, Si were all found to be in the range of the weight % as quoted by ESAB. Both Weld N^o1 and Weld N^o2 were found to have virtually no Al present compared with ESAB's values of 0.021%. The most significant difference in the observed results was for Cu, ESAB quoted 0.29% weight, compared with significantly lower levels, Weld N^o1 exhibited Cu levels of 0.1% and 0.07% for Weld N^o2.

5.2.4 Macrohardness

Macrohardness profiles were taken for both Weld N^o1 and Weld N^o2 in both the AR and the 5%SA weld metal conditions are summarised in Tables 5.7-5.8, and plotted in Fig. 5.18-5.20.

Three profiles were taken for both welds and in both the AR and the 5%SA conditions. Profile Line 1 is in the location where the AD samples were removed. Profile Line 2 refers to where the RH samples are located and Profile 3 is at the root of the weld. Table 5.7 summaries the results showing lower, mean and upper values of hardness, clearly showing that for both Weld N^o1 and Weld N^o2 in the AR condition Profile Line 1 has a high mean hardness value compared with that of Profile Line 3. Average hardness values of 188.5H_v (Profile Line 1) and 161.1H_v (Profile Line 3) for Weld N^o1 compared with 205.6H_v (Profile Line 1) compared with 193.7H_v (Profile Line 3) for Weld N^o2. Similarly for the 5%SA condition for both welds showed an increase in the average hardness values when compared with the AR weld metal condition. Average hardness values of 227.4H_v for Profile Line 1 for Weld 1 5%SA condition compared with 228.3H_v for Weld N^o2 5%SA comparing these with the values for Profile Line 3; 200H_v and 197.6H_v for Weld N^o1 5%SA and Weld N^o2 5%SA respectively.

The data collocated from profile data was split into the individual microstructures; parent plate, RH and AD for both weld metals and for both the AR and 5% conditions, as shown in Table 5.8 and Fig. 5.21. For Weld N^o1 for the AR condition the hardness profile in the C-Mn parent plate had an approximate value of 131 to 160H_v, there was a notable increase in the AD range from 191 to 220H_v. The RH microstructure exhibited a slight decrease in hardness ranging from 163 to 191H_v. The hardness profile fluctuates as the profile crosses the AD and RH microstructure. Increased hardness values were observed in the parent plate, RH and AD microstructure for the 5%SA condition. The RH microstructure had hardness values of 201 to 221H_v, the AD microstructure had average values of 222 to 257H_v, whilst the parent plate observed hardness values of 175 to 198H_v.

Weld N^o2 observed similar trends as Weld N^o1 for both the AR and 5%SA conditions. For the AR condition the parent plate exhibiting the lowest average hardness values of 158 to 188H_v, compared with 192 to 215H_v and 216 to 234H_v for the RH and AD. Similarly for the 5%SA condition the parent plate the average values ranged from 172 to 199H_v, whilst the RH microstructure ranged from 200 to 223H_v and 225 to 253H_v for the AD microstructure.

Generally Weld N^o2 exhibited higher hardness values for both the AR and the 5%SA conditions compared with Weld N^o1. Macrohardness indents, shown in Fig. 5.22 indicate that the AD microstructure has smaller indents than the RH microstructure.

5.2.5 Microhardness

Microhardness profiles for RH and AD microstructures in both the AR and 5%SA conditions for both Weld N^o1 and Weld N^o2 are shown in Table 5.9, and illustrated in Fig. 5.23-5.24.

For Weld N^o1 the reheated as-received profile (RHAR) ranged from 175 to 234H_v, compared with the as-deposited as-received profile (ADAR) which ranged from 222 to 277H_v. The microhardness values for Weld N^o2 ranged from 202 to 257H_v and 240 to 280H_v for the RHAR and ADAR microstructural conditions respectively.

Strain-aged material showed variability in microhardness values, with a slight increase being observed in both of the weld metals. RH5%SA and AD5%SA microhardness values ranged from 200 to 236H_v and 230 to 287H_v respectively, for Weld N^o1 compared with 220 to 265H_v for RH5%SA and 253 to 290H_v for AD5%SA for Weld N^o2.

It should be noted microhardness measurements for individual microstructural phases within the AD microstructure could not be assessed due to the fine nature of the weld materials (indents could not sample individual grains). However it is clear from Fig. 5.25 that the AD weld metal region exhibits smaller indentation marks than the RH microstructure for all equivalent conditions.

5.3 Discussion

5.3.1 Microstructure

It has been shown within the weld material that the microstructural features of the AD and RH microstructures are significantly different. The weld is produced from a multi-pass submerged-arc welding process; the AD microstructure is produced by deposition and solidification of the weld bead, and dominates the top layer of the weld, there are three large deposited weld beads. The RH microstructure is produced from the next pass raising the temperature, on cooling this region is grain refined.

The microstructure of the weld is complex, it is formed by a mixture of carbide and ferrite as well as a distribution of non-metallic inclusions such as oxides and silicates formed from deoxidation precipitation mechanisms in the molten weld pool. The typical AD microstructure as stated in Chapter 5.2.1, consists of three phases, allotriomorphic or grain boundary ferrite, α_{all} , acicular ferrite, α_{ac} and Widmånstatten ferrite, α_w , shown in Fig. 5.9. Acicular ferrite has a fine scale morphology, this increasing the strength of the material due to its small grain size making it a desirable feature whereas coarse grain boundary ferrite and lamellar structure (α_w) are undesirable from this view point. Acicular ferrite nucleates within prior austenite grains, at the interface between the non-metallic inclusions and the matrix. Acicular ferrite is often found on a fine-scale, this increases the strength of the material due to the small effective grain size (Hall-Petch relationship [178, 189], see 5.3.3) and also has good notch ductility because it is difficult for microcracks to propagate through acicular ferrite boundaries (high grain boundary density). Cleavage initiation sites on fracture surfaces of tensile, Charpy, CTOD and Blunt notch specimens often found in allotriomorphic ferrite areas.

Widmånstatten ferrite has a side plate, lamellar morphology nucleated at the austenite grain boundaries. It can also be classified as ferrite with aligned martensite retained austenite and

carbides, (MAC) and is akin to upper bainite or feathery bainite. Allotriomorphic ferrite is formed by a reconstructive mechanism, where all the atoms diffuse and grow across austenite grain boundaries.

The RH microstructure contained mainly equiaxed grains which exhibited coarser grain sizes nearer to the AD interface. The region with the coarser grains had a mixture of equiaxed ferrite and allotriomorphic ferrite grains. Due to the multi-pass welding procedure reheating into the intercritical region ($\alpha \rightarrow \gamma$) leads recovery, recrystallisation and grain growth, with an 'annealing' of the previous AD weld microstructure, therefore creating the RH weld microstructure.

5.3.2 Hardness Tests

Hardness tests revealed that the weld cross-section exhibited different hardness values from the top of the weld to the bottom, with the hardest regions being the top weld beads (located in the AD microstructural region, Profile Line 1) with the lowest hardness being found at the bottom of the weld, mainly the RH microstructural region (Profile Line 3). This is mainly due to the fine morphology of the AD microstructure, which is due in part to the annealing process that occurs from subsequent weld passes, Fig. 5.18-5.20.

If the weld is subjected to a postweld heat treatment (Table 4.3) the AD microstructure remains harder than the RH microstructure along the cross section of the weld (Fig. 5.21). AD values ranged from 191 to 220H_v and 221 to 257H_v in the AR and SA conditions respectively compared with 162 to 191H_v for RHAR and 201 to 220H_v for RH5%SA microstructural conditions for Weld N^o1. For Weld N^o2 the hardness values ranged from 216 to 224H_v and 225 to 253H_v for ADAR and AD5%SA microstructural condition, respectively, compared with values for 192 to 215H_v the RHAR microstructural condition and 200 to 223H_v for RH5%SA condition.

The higher AD hardness values were noted mainly in Profile Line 1 whilst the higher RH values were located in Profile Line 2. As a consequence specimens sampling the AD microstructure were located in at the top of the weld and the RH were located at the bottom of the weld cross section, so the limits of the hardness distribution in the weld cross-section for each condition would be sampled (Fig. 5.18-5.19). The weld metal also permitted a specimen arrangement of two Charpy sized samples (10x10x55 mm) from a single block, Fig. 4.12.

Therefore it can be inferred from the mean hardness values (Table 5.7 and 5.8) obtained for both microstructures in the AR and the 5%SA conditions for both weld metals (N^o1 and N^o2) that the strength of the weld increases at the expense of a decrease in ductility of the material after the prestraining and ageing process. The difference in hardness between the AD and RH microstructure in the AR condition was 23H_v compared with 21H_v for the equivalent microstructure in the strain and aged condition for Weld N^o1. Weld N^o2 exhibited differences in hardness of 20H_v between the ADAR and RHAR conditions, compared with 26H_v for the AD5%SA and RH5%SA conditions.

Considering the two weld microstructures in both weld metals, the AD region in Weld N^o1 exhibited the largest increase of 31H_v between the AR and 5%SA conditions compared with 12H_v for Weld N^o2 for the equivalent conditions. Thus it can be predicted from these higher hardness values within the AD microstructure for both welds and weld metal conditions, that this region exhibits a greater strength, hence a lower ductility compared with the RH microstructure, which exhibited a difference in hardness between the AR and 5%SA of 33H_v for Weld N^o1 and 5H_v for Weld N^o2. Using equation 5.1 and a mean hard hardening exponent value at room temperature approximately equated to disparities in the yield stress between AR and 5%SA of about 71MPa for the microstructure of Weld N^o1 and 23MPa for Weld N^o2, with differences between the AD and RH microstructure, in yield predicated yield stress of 72MPa and 11MPa for Weld N^o1 and Weld N^o2, respectively. The predicted disparities in yield stress are in agreement with the characteristic inhomogeneous nature of submerged arc weld. Also showing that a particular yield stress value should not be used as a

representative value for the whole weld metal material. This is an important result as it estimates the detrimental effects of low work hardening exponent values, showing for both microstructures after static strain ageing on the flow properties of the weld.

$$\sigma_y = 9.81 \frac{VHN}{3} (0.1)^n \dots (5.1)$$

Where σ_y is the yield stress in MPa

VHN is Vickers hardness number

n is the work hardening exponent.

If it is considered that both of the weld microstructures have the same chemical composition, the variation in hardness and therefore the predicted yield stress values can be associated with different ferrite phases found in the microstructures, as previously discussed. The AD microstructure contains a larger volume fraction of harder ferrite phases than the RH microstructure, such as bainite, acicular ferrite and Widmännstatten ferrite, which are not present in the RH microstructure. Microhardness measurements of individual ferrite phases in the AD microstructure and/or individual grains for the RH weld metal region could not be carried out due to the fine scale of these constituents. However previous researchers [98, 225] have estimated microhardness values for individual phases separately from their chemical composition. It was estimated by Bhadeshia and Svensson [98] that the hardness of acicular ferrite was 267VHN, which is used in this work as an approximate hardness value in the AR condition of the weld metal. The hardness value of bainite in the ADAR was evaluated by Blondeau [225] through the following equation:

$$VHN_{(bainite)} = -323 + 185C + 330Si + 153Mn + 65Ni + 144Cr + 191Mo + \log V_R (89 + 53C - 55Si - 22Mn - 10Ni - 20Cr - 33Mo) \dots (5.2)$$

where each element is used in wt.% and the cooling rate V_R , in °C/h. Harrison [226] estimated the mean cooling rate for the SAW process varied between 4.8×10^3 and 10.8×10^3 deg/hr. If the above equation was used to evaluate the approximate hardness values for bainite in the weld metals used in this work, it is expected Weld N^o1 would have a minimum value of 219HVN compared a minimum to 235VHN for Weld N^o2. Comparing the values of hardness Table 5.7 and 5.8, it is clear that the RH microstructure present lower values than those predicted for bainite and acicular ferrite phases, since this microstructure only contains equiaxed ferrite. The hardness value of acicular ferrite alone predicted by Bhadeshia and Svensson [98, 114] is greater than measured for the AD microstructure in the AR condition. This is consistent since not all austenite transformed to acicular ferrite during cooling to room temperature.

Another factor that should be considered is the higher dislocation density and internal enginery of the AD microstructure compared to the RH microstructure. The reduction of the dislocation density of the RH microstructure is considered to occur due to the annealing out of dislocation by the reheating effect of subsequent weld passes. Also the RH microstructure plasticity should also more uniformly distributed than in the AD microstructure. These comments help to explain the evaluated hardness values presented by both microstructures after static strain ageing and especially in the AD microstructure. Strain ageing behaviour is directly associated with density of dislocations formed after cold-working, the deleterious effect of strain ageing is more evident in the AD weld metal region due to the number of dislocations compared with the RH microstructure. The copper (0.29 wt%) adds solid solution strengthening to the weld through interstitial solid solution mechanism. However, this should affect both microstructures equally, since both weld metal regions contain the same chemical composition.

5.4 Conclusions

1. The microconstituents of the AD microstructure of the low alloy ferritic steel weld metal (Weld N^o1 and Weld N^o2) used as part of this research programme are; acicular ferrite, located in the interior of the austenite grain structure, Widmånstatten ferrite which nucleate at the austenite grain boundaries forming lamellar structure, and finally allotriomorphic ferrite or grain boundary ferrite, often delineating the columnar structure from the prior delta ferrite grains. The RH microstructure of the two welds contained mainly equiaxed ferrite grains and showed some coarsening of the RH grain size near the AD/RH boundary. Weld N^o1 generally exhibited slightly large weld beads in the AD region, as well as the weld width (gap filled) being slightly larger.
2. Inclusions were found to be similar for the two weld metals and for AD and RH microstructures, no differences were apparent between the AR and SA conditions. The inclusions were found to consist mainly of silicon, oxygen, manganese and iron with traces carbon and aluminium. Distribution of inclusions for Weld N^o2 showed that the 2-D modal inclusion diameter was approximately 0.53 and 0.48µm for the AD and RH microstructures, respectively. There were no notable statistical differences between either of the two microstructures, with the 95th percentile level lying in the order of 0.8 to 1.2µm. Larger inclusions can be found at the tail end of the distribution size.
3. GDS results confirmed the chemical compositions of both the weld metals as compared with the data supplied by ESAB. There were no significant differences in weight percent as quoted by ESAB compared to those acquired through GDS, apart from that the copper levels were lower.

4. A difference in macrohardness was found between the AD and RH microstructures for equivalent weld metal conditions in both Weld N^o1 and Weld N^o2. The AD microstructure is harder than the RH microstructure, while straining (cold working) and ageing the weld metal produced an increase in hardness values.
5. Weld N^o1 in the AR condition hardness values ranged from 191 to 204H_v and 162 to 191H_v for the AD and RH microstructures respectively, compared with 216 to 234H_v and 192 to 215H_v for the AD and RH microstructure for Weld N^o2. After straining and ageing a notable increase in hardness was observed for both weld metals. The hardness values of AD and RH in Weld N^o1 values ranged from 221 to 257H_v and 201 to 221H_v respectively compared with values for Weld N^o2 225 to 253 H_v and 200 to 223H_v for AD and RH respectively.
6. The weld metals also showed a variation of hardness across the cross-section of the weld and in respect to the sampling location. Profile Line 1 exhibited the highest hardness value, (AD weld beads) top of the weld compared with the RH microstructures, Profile Line 3, at the bottom of the weld, exhibited the lowest hardness values.
7. Microhardness values also exhibited an increase after prestraining and ageing of the weld metal had occurred. For Weld N^o1 values for the ADAR and RHAR conditions ranged from 222 to 227H_v and 175 to 234H_v, respectively, compared with 230 to 287H_v and 200 to 236H_v for AD5%SA and RH5%SA microstructural conditions. Weld N^o2 showed increases of 240 to 280 H_v for the ADAR condition compared to 253 to 290 H_v for the AD5%SA condition. The RHAR condition had hardness values ranging from 202 to 257H_v compared to 220 to 265H_v for RH5%SA condition.

Chapter 6 - Results - Tensile and Charpy Tests.

6.1 Introduction

Chapter 6 presents the results observed for the tensile and Charpy Impact testing of both weld metals, Weld N°1 and Weld N°2, in both microstructures AD and RH, for both conditions, AR and 5%SA. Flow property changes and variations in strength were assessed through tensile testing and analysis of the yield stress, tensile strength, work hardening exponent and elongation to failure, for both weld metals in various conditions and orientations. Absorbed energy transition curves were obtained through Charpy Impact testing to understand the effect of microstructure and thermo mechanical treatments of the weld metals.

6.2 Results

6.2.1 Tensile Testing

6.2.1.1 Weld N° 1

Engineering stress-strain and the equivalent true stress-true strain curves for the AR, mixed and transverse microstructural conditions are shown in Fig. 6.1-6.4 respectively and a summary of the flow properties are tabulated in Tables 6.1-6.4. A total of 18 ADAR and 18 RHAR specimens were tested for the single microstructure conditions, 15 mixed microstructure specimens and 18 mixed transverse specimens were tested across the temperature range. The flow properties, yield stress, ultimate tensile strength (UTS), total strain and work hardening exponent are also plotted in Fig. 6.5-6.6. It should be noted from the test curves that not all specimens exhibited a discontinuous yield point and therefore a

0.2% proof stress has been quoted for these specimens. The yield stress of the weld increases from 471 to 892MPa and 409 to 771MPa, over the temperature range from +20 to -196°C for the AD and the RH microstructure respectively, and 420 to 719MPa and 469 to 794MPa for the mixed and transverse microstructures. The tensile strength increased from 543 to 909MPa, 510 to 790MPa, 525 to 815MPa and 568 to 832MPa for the AD, RH, Mixed and transverse microstructures respectively across the same temperature range as the yield stress values (+20 to -196°C).

It can be seen from Fig. 6.5(a) and 6.5(b) that little variation between the AD, RH and mixed microstructure with a combined yield stress and ultimate tensile strength of 420 to 893MPa and 510 to 909MPa respectively. The yield stress drop between the upper (UYS) and lower (LYS) values was also evaluated from the data for the AD, RH, mixed and transverse conditions and microstructure across the temperature range. The results show that the as-deposited microstructure had the lowest yield drop compared with the other three conditions, with the mixed microstructure exhibiting the highest. The transverse results shown in Fig. 6.6(a) and 6.6(b) were consistently higher than both the AD and RH microstructures for both yield stress and ultimate tensile stress.

Values for total strain are plotted in Fig. 6.5(c) for the mixed and transverse Fig. 6.6(c) condition compared with both the AR microstructural conditions. Total strain values ranged from 25 to 38% for RHAR microstructure, 7 to 27% for the ADAR microstructure, 13 to 32% for the mixed microstructure and 21 to 33% for the transverse microstructural conditions over the temperature range of -196 to +20°C, relative to the length of the tensile specimen. In general the RH microstructure exhibited larger total strain than the ADAR, Mixed and transverse microstructural conditions. All specimens except those tested at -196°C exhibited localised necking before failure.

The mixed microstructural testpieces exhibit slightly higher tensile strength over the temperature range of -120 to -40°C, Fig. 6.5(b), as well as higher work hardening exponent

values across the temperature range, Fig. 6.5(d). The values of the work hardening exponent are slightly higher 0.14 to 0.21 for the mixed microstructural condition when compared to the 0.01 to 0.19 (ADAR) and 0.08 to 0.20 (RHAR) microstructures. The transverse microstructure exhibits both higher yield stress and tensile strength values of approximately 100MPa across the test temperature range, Fig 6.6(a) and 6.6(b). The total strain values of the transverse microstructure were in the same range as the ADAR condition, with the RHAR condition exhibiting the greatest amount of total strain. Work hardening values were slightly higher (0.08 to 0.24) for the transverse microstructure when compared to both the AR conditions, Fig. 6.6(d).

6.2.1.2 Weld N^o2

Tensile testing for Weld N^o2 was carried out for the AR; 18 specimens for the ADAR and 18 specimens for the RHAR, 17 mixed specimens and 18 transverse microstructural specimens, the flow properties for each of the conditions are tabulated in Tables 6.5-6.8 and Fig. 6.7-6.10 show the Engineering stress-strain and the equivalent true stress-true strain curves. As seen with Weld N^o1 not all specimens exhibited discontinuous yielding and so a 0.2% proof stress is quoted. The ADAR condition exhibited yield stress values ranging from 430 to 583MPa compared with the RHAR condition from 456 to 886MPa and tensile strength increases ranging from 468 to 883MPa and 545 to 965MPa for the ADAR and RHAR conditions respectively. Yield stress and tensile strength values ranging from 444 to 842MPa and 576 to 873MPa were exhibited for the mixed microstructural condition, compared with and transverse conditions respectively, while the transverse condition exhibited tensile strength values ranging from 439 to 928MPa and yield stress values of 561 to 948MPa, Fig. 6.11-6.12.

The ADAR and RHAR, mixed microstructure and transverse microstructure condition total strain values are plotted in Fig. 6.11(c) and 6.12(c). Total strain values for the ADAR condition ranged from 5 to 31% compared with 15 to 31% for the RHAR condition, whilst the mixed and transverse microstructural conditions ranged from 5 to 28% and 8 to 33% respectively. Work hardening values are shown in Fig. 6.11(d) and Fig. 6.12(d) it can be seen

that there is little difference or no distinctive trend between the four sets of data. Work hardening values ranged from 0.09 to 0.23 (ADAR), 0.10 to 0.23 (RHAR), 0.07 to 0.21 (Mixed microstructural condition) and 0.08 to 0.25 (Transverse condition). As seen for Weld N°1 the transverse condition for Weld N°2 exhibited slightly higher work hardening exponent values compared to the as-received condition. The work hardening exponents for both the as-received conditions are very similar, with the transverse being slightly higher.

6.2.1.3 Weld N°2 Strain and Aged Condition (5%SA)

The tensile specimens were nominally strained by 5% plastic deformation, loaded and unloaded at room temperature. The samples were then placed in a Lenton vacuum furnace at 300°C for 2hrs, following the procedures for Charpy, CTOD and Blunt notch tests, described in Chapter 4.3. A total of 36 specimens were tested in the 5%SA condition, 18 for both the AD and RH microstructure.

The corresponding engineering and true stress-true strain curves for the AD and RH microstructure weld metal regions are shown in Fig. 6.13-Fig. 6.14 respectively. As previously discussed in section 4.6, a reduction in the cross-section diameter is considered in the determination of the engineering stress-strain curves. The specimens presented a mean reduction in gauge cross section diameter from 2.99 ± 0.001 mm to 2.91 ± 0.001 mm.

Values of yield stress, tensile strength, elastic strain and total strain are presented in Table 6.9. In general the AD microstructure specimens were plastically deformed by $4.96\pm 0.08\%$ compared with the RH specimens by $4.97\pm 0.09\%$. The AD microstructure exhibited no discontinuous yielding, with yield stress values ranging from 415 to 600MPa. The RH microstructure had yield stress values ranging from 446 to 459MPa and 354 to 490MPa for 0.2% proof stress. Ultimate tensile strength values ranged from 536 to 601MPa and 475 to 546MPa for the AD and RH microstructures respectively.

Once the specimens had been aged, (applying 300°C for 2hrs) they were tested across the temperature range of -196 to 20°C. A summary of the flow properties including work hardening exponent for both weld metal regions is shown in Table 6.10 and displayed graphically in Fig. 6.17, corresponding engineering and true stress-true strain curves are shown in Fig. 6.15-6.16.

All but two of the specimens tested exhibited discontinuous yielding, AD18 tested at -160°C with a 0.2% proof stress of 705MPa and RH8 tested at -100°C with a 0.2% proof stress of 690MPa. The yield stress values ranged from 500-881MPa for the AD5%SA microstructure compared with 581-930MPa for the RH5%SA microstructure. The results presented in Fig. 6.17(a) demonstrate the yield stress values are very similar for both of the microstructures and are constantly higher than those for the AR condition, values ranging from 585 to 885MPa and 581 to 987MPa were observed for the AD5%SA and RH5%SA conditions, respectively. Ultimate tensile strength values varied little between either of the microstructures and/ or conditions. The AD5%SA microstructure exhibited UTS values of 613 to 855MPa compared with 588 to 921MPa for the ADAR condition. Whilst UTS values ranged from 544 to 965MPa and 602 to 987MPa for the AR and 5%SA condition respectively for the RH microstructure, Fig 6.17(b). The RH microstructure in the 5%SA condition exhibited both higher values for the yield stress and UTS compared with AD5%SA condition.

Shown in Fig 6.17(c) the total strain values for the 5%SA condition are similar to the AR values, the AD5%SA microstructure exhibits total strain of 11 to 26% and the RH5%SA condition exhibits values of 18 to 27% compared with 4 to 29% and 14 to 33% for the ADAR and RHAR respectively, although the 5%SA values are lower than those of the AR condition. There is little difference between the work hardening exponent values for the microstructural conditions, with values ranging from 0.07 to 0.12 for the AD5%SA and 0.08 to 0.13 for the RH5%SA, Fig 6.17(d). Work hardening exponent values for the 5%SA condition are much lower than those exhibited for the AR condition, 0.09 to 0.23 for the ADAR and 0.10 to 0.23 for the RHAR condition. Across the test temperature range of -120°C to 20°C the AR

condition has a mean work hardening exponent value of 0.19, compared to a slight decrease to 0.11 for the 5%SA condition.

6.2.2 Analysis of Charpy Tests

Both an extensive temperature range and number of specimens were used in the Charpy impact tests to allow for a good estimation of ductile-to-brittle transition temperature (DBTT) to be made for Weld N^o2 for both the AD and RH microstructures in both the AR and 5%SA weld metal conditions. A total of 28 AD and 28RH test specimens for the as-received condition, and 20 AD and 26 RH test specimens for the 5%SA condition. These experiments were already carried out for Weld N^o1 as part of an earlier research programme [15]. The results of the impact tests are presented in Tables 6.11-Table 6.14 for both weld metal regions and in both conditions. For each of the weld metal conditions the absorbed energy data has been plotted against temperature and is shown in Fig. 6.18-Fig. 6.26. The overall collected data is shown in Fig. 6.18, for all four weld metal conditions, whilst Fig. 6.19 and Fig. 6.20 show the separate data for the AR and 5%SA weld metal conditions, respectively. The data also plots AD and RH microstructural regions Fig. 6.21 and Fig. 6.22, respectively. The ADAR microstructural condition absorbed energy values ranged from 3J to 143J across the test temperature range of -196 to 200°C. The RHAR microstructural condition, across the same temperature range, exhibited absorbed energy values ranging from 4 to 167J. Compared with 2 to 105J and 2 to 140J for the AD5%SA and RH5%SA microstructural conditions, respectively.

Tanh curves were fitted to the data, using the basic weighting function and used for comparing the different data sets for aiding the determination of the impact toughness properties of the weld metal exposed to different thermo mechanical treatments and temperatures, Fig. 6.23. For this work the DBTT has been defined at 40 J level from the Tanh curve. It can be seen that the ADAR and RH5%SA conditions exhibited similar Tanh curves, with the RHAR and AD5%SA conditions exhibiting extremes in conditions.

Values of DBTT (40 Joules), absorbed energy at the transition temperature of 40°C, and the upper-shelf energy level (USE) are shown in Tables 6.15 and Fig 6.24. It can be seen from the tables that the RHAR microstructure has a lower DBTT of -50°C compared with the -10°C for the ADAR microstructure, as defined at the 40J energy level. After strain ageing both microstructures exhibited an increase in the DBTT at 40J levels, with a temperature of -30°C for the RH5%SA microstructure and -10°C for the AD5%SA microstructure. The difference between the DBTT values at 40J energy levels for the RHAR and RH5%SA microstructures was 25°C compared with 20°C for the AD microstructure in equivalent weld metal conditions. The overall difference in the DBTT at 40J was 65°C, comparing the two extremes in conditions RHAR to AD5%SA.

Using the data to compare energy levels at a given temperature (in this work defined at 40°C) it can be seen from Fig. 6.26 and Table 6.15 that the AD5%SA exhibits the lowest absorbed energy level of 70J compared with the ADAR microstructure condition of 105J, a difference of 35J. A similar trend is noted in the RH microstructure with a difference of 27J from the RH5%SA (110J) to RHAR (137J) microstructural conditions. Upper shelf energy values decreased slightly from 158J for the RHAR microstructural condition to 140J for RH5%SA a difference of 35J, with a further decrease noted for both the ADAR and AD5%SA microstructural conditions of 138J and 105J, repetitively, a difference of 20J. The USE ranging 53J between the two extremes in weld metal conditions, RHAR and AD5%SA. The AD microstructure seems to be more sensitive to the strain and ageing process compared to the RH microstructure. The absorbed energy values have shown more scattered in the transition region, but it can be inferred from the data that the RHAR and the AD5%SA, respectively are the best and worst microstructural conditions.

The surfaces of the broken halves of the Charpy impact specimens are shown in Table 6.16-6.19 for all microstructural conditions. Fig 6.25-6.29 show the corresponding plots, for absorbed energy levels and temperature versus ductile thumbnail, crystalline area and lateral expansion. Tables 6.16-6.19 detail ductile thumbnail (DT), lateral expansion (LE) and

crystalline area % (CA) measurements. Ductile thumbnail ranged from 0 to 2.365mm across the test temperature range of -196 to 40°C for the ADAR condition, compared with 0 to 3.568mm for the RHAR condition across the temperature range of -196 to 20°C. Both the 5%SA conditions exhibited less ductile thumbnail than the AR condition with the AD5%SA condition ranging from 0 to 1.315mm for -196 to 60°C and 0 to 2.199mm for -196 to 40°C for the RH5%SA condition. The lateral expansion ranges from 0 to 2.115mm for -196 to 100°C for ADAR compared with 0.245 to 2.510mm for -60 to 140°C for RHAR. 5%SA conditions again, exhibited a similar trend with the RH5%SA condition exhibiting values of 0 to 1.930mm for -196 to 40°C and 0 to 2.373mm for -196 to 60°C for AD5%SA. Crystalline area % ranged from 100 to 0% for -196 to 100°C for ADAR compared with 100 to 0% for -196 to 40°C for RHAR. Values ranged from 100 to 0% for -196 to 60°C and 100 to 16% for -196 to 40°C for AD5%SA and RH5%SA conditions, respectively.

The plots in Fig 6.25-6.29 show the basic trend, that at the same temperature, for equivalent conditions that the RH microstructure will exhibit larger amounts of ductile thumbnail and lateral expansion and small amounts of crystalline area % than those measured for the AD microstructure. Plots presenting the linear regression for the ductile thumbnails versus absorbed energy show that the RH microstructure exhibits slightly larger absorbed energy per unit of ductile thumbnail extension than the AD microstructure for both conditions, Fig 6.25(a), 6.26(a) and 6.27(a). This trend is even more evident after the strain ageing treatment has been applied Fig 6.27 and 6.30. There is no clear difference between equivalent microstructural conditions in the correlation between absorbed energy and lateral expansion. However, ductile thumbnail, lateral expansion and crystalline area % all show linear relationships with impact energy. There is clear separation in the data for crystalline area %, Fig 6.26(b) with the RHAR condition exhibiting higher values, except this trend is not quite so evident after straining and ageing, Fig 6.27(b). Again it is clear that the AD5%SA and the RHAR microstructural conditions are the extremes in behaviour.

6.3 Fractography

Extensive fractography has been carried out on the fracture surfaces of the tensile and Charpy specimens. The specimens were tested over a temperature range of -196 to 200°C to analyse the fracture micromechanism taking place and to gain an insight into the nature of microstructure features and influence of microstructure. Fracture surfaces were generally examined from the extremes in temperature range, with some selected from the transition region.

6.3.1 Tensile Tests

The AD microstructure in both Weld N°1 and Weld N°2 exhibited larger areas of cleavage fracture than the RH microstructural condition at a given temperature for all the conditions studied. Fig. 6.30 and Fig. 6.31 show typical fracture surface of a tensile specimen tested at -196°C and it can be seen that the specimen exhibits fully brittle transgranular cleavage behaviour, with no visible necking on the specimen. For both of these specimen cleavage fracture was initiated by an inclusion, these are generally located within large allotriomorphic ferrite grains. From the observations of the fracture surfaces it can be inferred that the AD microstructure has larger cleavage facets, these are defined by the cleavage steps indicated by an arrow in Fig. 6.30 and river lines (principal features of cleavage fracture), indicated with an arrow on Fig. 6.31.

The RH specimens tested at -196°C exhibited a mixed mode of fracture, with characteristics of both cleavage and ductile fracture. Fig. 6.32 shows a typical fracture surface, it can be seen there has been some localised plastic deformation in the form of microvoid coalescence, as there has been slight necking of the specimen diameter and areas of cleavage fracture are visible, indicated by flat facets on the fracture surface and shown with an arrow. Both microstructures when tested at 20°C exhibited extensive necking of specimen diameter,

failing in a fully ductile manner. Fig. 6.33-6.34 show two typical fracture surfaces from both microstructural conditions, there is general microvoid coalescence across the whole fracture surface, with inclusions being responsible for the initiation of microvoids.

Fig. 6.35 shows an AD specimen tested at -120°C . The fracture surface shows a mixture of two principal fracture mechanisms, necking of the specimen can clearly be seen, as well as microvoid coalescence, both ductile mechanisms. While large areas of cleavage are visible, as well as secondary cracking, cleavage steps and macroscopic river lines, all indicative of brittle fracture. While a RH specimen tested at -160°C , Fig. 6.36, exhibited general necking of the specimen and localised plastic deformation characterised by microvoid coalescence. In general terms it was noted that for the AR and 5%SA conditions the fracture surfaces were either characterised by either fully brittle fracture or fully ductile fracture, very few exhibited the mixed mode failure. Whereas for the mixed and transverse conditions the fracture surfaces went through the transition of fully brittle, mixed mode with more brittle fracture dominating, mixed mode with more ductile dominating (creating “star” fracture surface) to fully ductile fracture, corresponding from temperature increasing from -196 to 20°C , Fig. 6.37. Typical fracture surfaces for the transverse microstructure are shown in Fig. 6.37 ranging from -196 to 20°C , all these specimens exhibiting varying amounts of plastic deformation. It can be seen that the specimen tested at -196°C , Fig. 6.38(a) and 6.38(b), exhibited quasi - cleavage fracture, with the surface having both microvoids and large flat cleavage facets. The specimens tested at -40 and 20°C both failed in a fully ductile mode, with inclusions found for the initiation of microvoids.

6.3.2 Charpy Tests

The fracture surfaces of the Charpy specimens are shown in Fig. 6.39-Fig. 6.44 for all four microstructural conditions. It can clearly be seen, using the naked eye without magnification the different modes of failure; ductile, brittle or a mixture of both. Fig. 6.43 shows the fracture appearance changes from 100% cleavage fracture to 100% fibrous or ductile fracture as the temperature increases. It can be seen that lateral expansion and ductile thumbnail size

all increase in both microstructures and across all conditions with increasing temperature, conversely a decrease in crystallinity is observed with temperature increases. The AD microstructure in the AR condition exhibited fully ductile fracture at 100°C, where as the RHAR microstructural condition is fully ductile at 40°C, this transition is the same for the 5%SA condition. Examination of some of the Charpy fracture surfaces showed bands of both AD and RH microstructures, with metallographic examination confirming that ductile bands lay in the RH microstructure, also these were only found on the fracture surfaces of the AD specimens. It should also be noted these ductile bands were far more prominent in the AR condition when compared with the 5%SA condition, this is could be due to the relatively low DBTT of the weld in the AR microstructure, thus permitting the appearance of the RH ductile bands within the transition region.

Fractographic examination of specimens revealed that all specimens which had failed by fracture instability were a result of brittle transgranular cleavage fracture for both the AR and the 5%SA microstructural conditions. Fig. 6.44 shows a comparison between the cleavage facets for the AD and the RH microstructures for both conditions, the fracture surfaces for the AD microstructure exhibited a wide range of cleavage facets and sizes, with a characteristic “rough appearance”. For this type of weld metal it has been widely reported that large cleavage facets related to allotriomorphic grains, whereas smaller facets correspond to regions of acicular ferrite. Brittle fracture in the RH microstructure was characterised by a more uniform distribution of cleavage facets, both in appearance and size. This corresponds to fracture through equiaxed ferrite grains, hence giving a finer appearance on the fracture surface. Despite the high strain rates generated by Charpy impact tests, ranging from 10^2 to 10^4 s^{-1} , transgranular cleavage initiation sites could be found on the fracture surface, Fig. 6.44-Fig. 6.49. It was found that initiation was caused by an inclusion in both the AD and RH microstructures, it can also be seen that cleavage initiated quite close to the notch root, for specimens tested from the AD microstructure, Fig. 6.45-6.47 and RH Fig. 6.50. Other features that have been labelled are cleavage steps and secondary cracks; Fig. 6.48 shows a secondary crack running though the site of initiation, secondary cracking is not as common for the RH microstructure due to its morphology, shown in Fig. 6.49 and Fig. 6.50.

Examination of specimens which showed some purely ductile failure, e.g. specimens tested in the transition and upper - shelf regions or exhibited some ductile thumbnail extension before the onset of catastrophic failure, revealed that due to the levels of shear stress this resulted in internal necking and coalescence of microvoids initiating from non - metallic inclusions, this is a result of decohesion of the matrix/ inclusion interface. Fig. 6.51-6.54 show the general appearance of ductile fracture mechanism for both microstructures and in both of the weld metal conditions. Size and shape of the dimples has been found to be dependent on their location on the fracture surface, with their direction being highly orientated if located close to the borders and the notch root of the Charpy specimen and non - equiaxial due to the tensile testing stress state acting in those regions. The shape and size of the dimples appears to be the same for both the AD and RH microstructures, although specimens tested in the 5%SA condition appeared visually to have exhibited shallower voids, hence the strain and ageing has affected both the plastic deformation and work hardening properties.

6.4 Discussion

6.4.1 Tensile Testing

6.4.1.1 Microstructural Effects

Tensile test results showed little difference in the yield stress and tensile strength of the two microstructures. However, the strength across the weld cross - section from top to bottom and within a microstructural condition can vary considerably in terms of the hardness from corresponding microstructures. This is possibly due to the amount of annealing the weld beads received from the subsequent weld passes. If it is considered that both the microstructures are subjected to the same amounts of annealing the AD microstructure would still present both yield stresses and higher hardness than the RH microstructure due to the constituents of the weld metal. Tensile test results thus show closely similar yield stress and tensile strength of the two microstructures in their AR and 5%SA conditions. The AD microstructure did present lower ductility than the RH microstructure.

The RH microstructure also exhibited longer uniform and total deformation before specimen failure for equivalent conditions. Therefore, quoting or using a singular yield stress value would not be representative for the whole weld metal. The differences exhibited in yield stress values are in agreement with the characteristic inhomogeneous nature of a submerged arc weld metal. Novovic [13] prestrained a carbon - manganese weld metal by 9% using cold deformation, this material presented similar shifts for impact toughness tests. If this level of prestraining was considered as a “saturation level”, as both microstructures present similar properties, then the AD and the RH microstructure would still present some differences in flow properties after cold deformation by just 5%, this is in agreement with the hardness and tensile test results presented in this current work.

6.4.1.2 Grain size

The AD microstructure presented both higher yield stress and tensile strength values, compared to those in the RH microstructure; this cannot be attributed to the effects of grain size. From the Hall-Petch relation (equation 6.1) [178, 189], for materials which are similar but exhibit different grain size, the one with the small grains should be stronger. Hence, on this basis, the RH microstructure would be stronger than the AD microstructure due to it having smaller equiaxed grains. The strength of the AD microstructure can be reasonably attributed to its increased dislocation density, as discussed 5.3.1 and larger surface area of the harder ferrite phases. Reduction in strength due to large grain size AD microstructure does not overcome the opposite effects suggested due to the two reasons stated above. Reduction in the dislocation density of the RH microstructure is considered to occur due to annealing, as a result of the multi - pass welding process, this is evident by the hardness results obtained. The strength reduction due to large grain size of the AD microstructure does not overcome the opposite effect possibly caused by the dislocation density and larger surface area of harder ferrite

$$\sigma_0 = \sigma_i + kD^{-\frac{1}{2}} \dots 6.1$$

Where σ_0 is the yield stress, σ_i is the “friction stress”, k is the “locating parameter”, measuring the relating hardening contribution of the grain boundaries and D is the grain diameter.

6.4.1.3 Strain Ageing

Strain hardening and then subsequent ageing of the weld metal resulted in an increase in strength and hardness values, and a decrease in ductility, these effects are similar to those caused by neutron embrittlement. It can be inferred from the engineering stress - strain curves and from the flow properties observed for the AR compared to those for the 5%SA condition that the cold deformation process influences and causes a reduction in the microstructural effects on the flow properties of the different microstructures. Thus it can be inferred that applying a more severe cold deformation process would result in both microstructures exhibiting similar flow properties. Due to the RH microstructure being annealed because of the heat input from the multi - pass welding procedure, it has a smaller dislocation density and therefore could have a shorter dislocation length per unit volume than the AD microstructure. This is supported by slightly higher values of work hardening exponent, n and larger total plastic strain for the RHAR condition compared with the RH5%SA condition, compared with the AD microstructure in both conditions.

It would seem that the AD microstructure is more sensitive to the strain - ageing process than the RH microstructure, the effect of strain - ageing on the ductility of the AD microstructure is more evident compared with the RH microstructure. After strain - ageing the AD microstructure has a more accentuated yield point drop when compared with the RH microstructure. After plastic deformation the AD microstructure only exhibited 2% proof stress values, whereas after strain - ageing, all specimens exhibited discontinuous yielding.

An explanation for this apparent susceptibility of the AD microstructure to static strain ageing is the higher dislocation density, also both microstructures have higher yield stress values after the strain - ageing process compared with the AR condition, it can be inferred from this results that part of the C and N atoms remain in solid solution even after PWHT. These elements could be responsible for the ageing process through their interaction with dislocations.

The AD microstructure is more sensitive to the strain ageing process compared to the RH microstructure, with a further effect being seen on the ductility of the weld metal, with the AD microstructure being greater effected than the RH microstructure. The AD microstructure also presents an increase in yield stress and tensile strength higher than the RH microstructure. One apparent explanation for this pronounced susceptibility of the AD microstructure to the static strain ageing is the different ferrite phases; fractography revealed that cleavage initiation sites (CIS) were located within large allotriomorphic ferrite grains; these contain dislocation pile - ups which are long, which could be more susceptible to strain ageing through dislocation pinning by atoms in solid solution compared to the RH microstructure which contain smaller and equiaxed ferrite grains. The RH5%SA condition tested at -196°C , -160°C and -120°C had fracture surfaces which revealed a mixture of both ductile and brittle fracture modes, exhibiting both plastic deformation linked with the characteristics of cleavage fracture with no distinctive cleavage initiation sites. The fracture surfaces from the tensile tests revealed that the percentage of brittle areas, e.g. cleavage facets become larger from the AR condition to the 5%SA condition. Cleavage cracks are also noted in the fracture surfaces of the RH specimens.

6.4.1.4 Natural ageing

Both the weld materials used in this research received a post weld heat treatment as shown in Table 4.3. The PWHT is applied to relieve and reduce any residual stress that may have occurred during the weld procedure. Another benefit of this procedure is to promote the precipitation of carbides, thus avoiding the presence of elements in solid solution, mainly N

and C. Therefore it is not expected for the material to have aged naturally at room temperature. However, the tensile strength for the data gathered for the 5%SA conditions are slightly higher than those in the AR condition. This maybe an indication that the material might have aged naturally before testing was conducted. During the prestraining process none of the AD microstructure exhibited a yield point, whilst the majority of the RH microstructure specimens did exhibit a yield point.

6.4.1.5 Work - Hardening Exponents

It is evident from the results obtained and the discussions thus far there has been a reduction in the work hardening exponent, n for both microstructures after cold deformation and static strain ageing. Over the test temperature range of -120°C to 20°C the AR condition exhibited mean work hardening exponent values of 0.19 compared to 0.11 for the 5%SA condition. It should be noted that the difference between the work hardening exponents between microstructures is small, any interpretation is made more challenging because it is difficult to locate the entire gauge length within a single microstructure.

The attainment of work hardening exponent values from the true stress-true strain curves is easier for the AR, mixed and transverse conditions because as load increases, the work hardening is more evident in these conditions. The estimation of n values becomes difficult as the interpretation of the 5%SA curves exhibit flattened behaviour in the plastic region of the curve. Nevertheless, both the AD and RH microstructures exhibit constantly lower work hardening values when there are subjected to the straining and ageing process compared to those in the AR condition.

Therefore, it can be inferred from the low n values that the work hardening capacity of the microstructures is affected. Values of work-hardening exponent, n , for both welds exhibited no effect of temperature within the temperature range (-196 to 20°C) used in the current work. However, in general the ADAR microstructure exhibits similar n values (0.09 to 0.23)

compared to RHAR microstructure (0.10 to 0.23), whilst the AD5%SA condition exhibited similar but reduced work hardening exponent values ranging from 0.07 to 0.12 and 0.08 to 0.13 for the RH5%SA condition. The AD5%SA and RHAR microstructural conditions respectively, lowest (mean value of 0.11) and highest (mean value of 0.19) n values at equivalent temperatures (shown in Fig. 6.17(d)), therefore the work hardening capacity of the AD microstructure is more affected static strain ageing than the RH microstructure. It should be emphasised that n values were obtained in region of uniform plastic deformation up to maximum load.

6.4.2 Charpy Tests

6.4.2.1 Effects of Notch Plane Orientation

It has been discussed in Chapter 4.7 that the Charpy specimens were machined with the notch plane orientation defined that the notch root would sample only a single microstructure, the notched face of the specimen is parallel to the direction of the weld. The root of the notch was fixed to a specific location with respect to the microstructure. The main advantage of the surface notch orientation was to allow for the assessment of impact properties for a single weld metal region, either AD or RH. However the geometry of the multipass weld and the size of the last deposited weld bead would not allow the cross-section of the Charpy impact specimens to sample only one microstructure. This is because although the notch root is placed within the AD microstructure, specimen halves examined from the lower shelf and transition region usually consisted of both microstructures. This study should be differentiated from those of Novovic and Wenmen [13, 14] both of which had Charpy notch faces perpendicular to the welding direction. In-particular Novovic worked with a C-Mn weld metal which contained a lower number of weld passes than the weld metal used in this programme of work, and consequently larger weld beads, this permitted the sampling of only one microstructure.

6.4.2.2 Upper and lower shelf behaviour

The upper shelf energy levels of both microstructures are very distinctive for the AR and the 5%SA conditions, with the RHAR and the AD5%SA presenting the extremes, with the AD5%SA condition consistently exhibiting lower values. On the lower shelf the energy levels are indistinguishable whereas on the upper shelf they are different values. This behaviour is also noted in the plots for the ductile thumbnail, lateral expansion and percentage of crystallinity versus both temperature and energy absorbed. Comparisons of impact transition curves for the AD and RH microstructure revealed the RH microstructure was not as affected when strained and aged compared with the AD microstructure. The RH microstructure saw a decrease in the USE of 27J compared with 35J for the AD microstructure, this may be related to the higher work hardening exponent values for the RH weld microstructure for both the AR and 5%SA conditions, also the reduction in the upper shelf energy could be a consequence of the reduced work - hardening capacity of the strain aged materials, as there is an appreciable reduction on both microstructure following strain and ageing.

It has been shown that the micromechanism of fracture at the upper shelf energy level for the weld metal in all microstructural conditions is microvoid coalescence. Absorbed energy results and fractography showed the AD microstructure exhibits higher temperature values corresponding to 0% crystallinity than the RH microstructure for all conditions. The onset of the upper shelf temperature region is not strongly affected by prestraining, both Novovic [13] and Patrocinio [15] obtained the same conclusion. Specimen tests at lower temperatures essentially failed by brittle cleavage fracture. The impact energies in this lower shelf region are so small that any variations caused by microstructure in all conditions are not differentiated.

Microvoid coalescence and the amount of energy absorbed are expected to depend strongly on the work hardening exponent, second phase particles and their distribution. Noting that the 2D distribution of inclusions is closely similar in both microstructures, then the influence of

the work-hardening exponent would be expected to dominate. Attempts have been made, Figs. 6.25-6.29, to analyse the amount of ductile thumbnail in each Charpy testpiece and to relate this to the impact. Any comparison between different microstructure and condition is complicated by the fact that a similar amount of ductile crack growth for each condition, at will occur at different test temperatures.

Similar trends and correlations are also seen for the shear lip size and the lateral expansion both plotted against impact energy. These show little separation of the microstructures, with results more scattered than the data set for the ductile thumbnail plotted against impact energy. However, when plotted (Fig. 6.26) against temperature there is still a separation of microstructures, in general the AD microstructure, for both conditions exhibits small lateral expansion, ductile thumbnail sizes and shear lip sizes when compared to the RH microstructure in both conditions when compared at the same temperature.

6.4.2.3 Transition region behaviour

Notched - bar impact tests are often subject to considerable scatter within the transition temperature region [1, 13-15, 24, 27, 40, 219, 227, 228]. Charpy impact test results for multipass submerged - arc welds have shown a large amount of scatter even when located within a single microstructure as studied as part of this programme. This behaviour can be attributed to several factors; variations in local properties within the weld metal in specimens machined from the same microstructure, and variability in the testing procedure. Also the intervention of cleavage after varying amounts of ductile thumbnail extension is an important factor. However, there are clear differences in the impact transition curves for both the AD and RH microstructures, which strongly suggest these weld metal regions exhibit distinctive impact toughness for all conditions studied. Straining and ageing the materials shifted the DBTT at 40J by 65°C between the two extremes in microstructural conditions, RHAR and AD5%SA. The DBTT shifts at 40J by 45°C between the two AR conditions compared with 40°C between the two strain aged conditions. The differences in the DBTT can be related to microstructure since both the weld metal regions will have similar compositions.

The Charpy results clearly show that even within the fine beaded welds, as used during this experimental programme, differences can clearly be seen in the transition temperatures for both the weld microstructures AD and RH, and these become accentuated after strain and ageing has occurred. The AD microstructure exhibits higher DBTT than the RH microstructure for both conditions. Within the results there is a large amount of scatter within the transition region and even within a single microstructure. This is attributed to the varying amounts of ductile crack growth, and then the intervention of cleavage fracture. There is however a very clear separation between the two microstructures and even between the conditions, thus suggesting a difference in the resistance of the two microstructures to cleavage fracture. Both of the conditions for the RH microstructure exhibited an increased gradient of slope in the transition region compared to the same conditions for the AD microstructure, shown in Fig. 6.23; this could be a result of the difference exhibited in the work hardening of the material. The DBTT also decreases as the work hardening exponent, n , increases, Fig. 6.24 and Tables 6.15-6.16. For the extremes in condition the RHAR microstructural condition exhibits the lower DBTT of -43°C and a mean n value of 0.19 compared with the AD5%SA microstructural condition which exhibits the highest DBTT of 15°C and a mean n value of 0.11.

When considering a value of ductile thumbnail extension in the transition region, (e.g. -20°C) the amount of absorbed energy is higher for the AR condition compared with the 5%SA condition, shown in Fig. 6.27, where the two AR conditions have values of absorbed energy and ductile thumbnail of 33J and 1.37mm and 65J and 2.59mm for the ADAR and RHAR conditions respectively, compared with 19J and 0.61mm and 49J and 1.30mm for the AD5%SA and RH5%SA conditions respectively. It can be seen from these results that the ductile thumbnail is reduced after the strain ageing process has been applied.

Within the transition region there is competition between fibrous (microvoid coalescence) and transgranular (cleavage) fracture. Microvoid coalescence involves high absorption of energy and this is related to the amount of deformation during the process. On the other hand,

transgranular cleavage has a very small contribution to the overall energy absorbed process, thus the size of thumbnail extension is essential to promote high impact energy values. Work - hardening exponent also plays a fundamental role in microvoid coalescence since this parameter is directly related to the amount of energy absorbed per unit of ductile thumbnail extension.

The results observed from the fracture surfaces measure the percentage crystallinity versus temperature followed a similar trend to the impact energy versus temperature. Lower shelf results show 100% cleavage fracture whereas upper shelf temperatures show 100% ductile fracture. Higher hardness of the strain aged condition could help promote cleavage fracture at higher temperatures. Also there is a difference in the hardness of both the microstructures and the conditions which might promote cleavage fracture at higher temperatures. Also Weld N^o2 had higher hardness values than Weld N^o1 thus lower upper shelf values were exhibited, also higher DBTT temperatures, as well as smaller amounts of ductile thumbnail and lateral expansion and a higher percentage of crystalline area for corresponding temperatures.

In summary, the extremes of microstructural conditions, the RHAR exhibited the largest ductile thumbnail extension and a higher amount of energy absorbed per unit of ductile thumbnail extension compared with the AD5%SA condition. On this basis it is possible to suggest why the RH microstructure exhibited smaller Δ DBTT and Δ USE shifts after strain - ageing than the AD microstructure. Within the transition range there is the occurrence of both ductile thumbnail extension and then the occurrence of cleavage fracture, thus cleavage fracture directly controls the amount of absorbed energy at a given temperature. It has been shown that the RH microstructure has longer ductile thumbnail extension compared with the AD microstructure. Hence the cleavage fracture mechanism intervenes earlier in the AD weld metal region and especially for the AD5%SA condition.

6.4.2.3.1 Forms of the Ductile-to-Brittle Transition (DBT)

Other authors [14, 15] claim there is a close correlation between the forms of DBT (steady or abrupt) and the density and distribution of the dislocations and dislocation sources in the material. Here the AD microstructure exhibits more steady impact transitions and higher ductile-to-brittle transition temperatures than the RH microstructure for all the equivalent weld metal conditions, as shown in Fig. 6.18-6.20. Even after static strain ageing the RH microstructures exhibits lower DBTT (-68°C) than the AD microstructure (-17°C) in the as-received condition. Thus the latter microstructure supposedly contains higher dislocation density and also dislocation sources than the RH microstructure.

The trend of ductile-to-brittle transition can also be correlated with the fracture toughness, K_{IC} (δ_{crit}), of the material. Soft transitions are related to a steady increase of the K_{IC} (δ_{crit}) with temperature. Therefore the K_{IC} (δ_{crit}) fracture of the RH microstructure would be expected to rise less steadily with temperature than the AD microstructure. The different trends in the variation of crack tip opening displacement (CTOD) with increasing temperature, for both the AD and RH microstructures was obtained in earlier work by Farron [229] over the temperature range of -120 to -60°C , using the same material and was further explored during this current work. Both studies showed that the AD5%SA condition and the RHAR condition were the extremes of behaviour, with these exhibiting the worst and best CTOD values respectively.

6.4.2.3.2 Effects of prestraining and static strain ageing on Charpy impact energy in the transition region

Within the transition region, there is competition between fibrous fracture (microvoid coalescence), involving relatively high absorption of energy since it is related with high levels of deformation during the coalescence process and transgranular (cleavage) fracture, has a very small contribution to the overall energy absorbed in the process. Thus the size of the

thumbnail extension is essential to promote high absorption of impact energy (i.e. high impact or notch toughness). Moreover, the work-hardening exponent also plays a fundamental role in the fibrous crack extension process since this parameter can be directly related to the amount of energy absorbed per unit of extension. So, for the same amount of ductile thumbnail extension values, the energy absorbed by the as-received material is expected to be greater than the 5%SA condition. As shown in Tables 6.16-6.19 at 100J absorbed energy the corresponding values of ductile thumbnail extension are 2.37mm and 3.14mm for the ADAR and RHAR microstructures, respectively, and 1.95mm for the RH5%SA condition. Therefore, the material which exhibits lower n values would need to present a longer ductile thumbnail extension at the same energy level, in turn, increasing the chances of a cleavage intervention through sampling.

6.5 Conclusions

1. Significant differences in yield stress and tensile strength were, however, noted after straining and ageing for both the AR conditions. Little effect of microstructure on yield stress and tensile strength has been seen in this study. The ADAR microstructure did exhibit reduced ductility of the RHAR microstructure.
2. Both of the microstructures and across all conditions; AR, mixed, transverse and 5%SA exhibited a strong dependence of yield stress and tensile strength in relation to temperature, with the strength increasing as the temperature decreases. Any trend in work hardening exponent with microstructure were unclear. However over the temperature region of -120°C to 20°C, the mean work hardening exponent for the AR condition was 0.19 (ranging from 0.15 to 0.23), compared to the strain aged condition, which exhibited a reduction to 0.11 (ranging from 0.08 to 0.13).
3. The AD microstructures exhibited increased ductile-to-brittle transition temperatures (DBTT) and reduced upper - shelf energy levels compared with the RH microstructure

in both the AR condition and the 5%SA condition. Measuring the DBTT at 40 J the Charpy impact transition curves show a clear difference between all microstructures and conditions. The RH microstructure has higher upper-shelf energy levels for. Lower shelf energies were relatively indistinguishable amongst the different microstructural conditions.

4. The extremes in conditions the RHAR and the AD5%SA exhibited differences in DBTT and USE values of 65°C and 53J respectively. The ADAR condition exhibited $\Delta\text{DBTT}_{40\text{J}}$ and USE shift values of -10°C and 138J compared with the AD5%SA condition of 10°C and 105J, compared with -55°C and 158J for the RHAR and -30°C and 140J for the RH5%SA conditions. The differences between the AD and RH microstructural region transition temperature at 40 J for the AR and 5%SA conditions were 45°C and 40°C respectively.
5. A strong linear relationship was obtained between the absorbed energy and increased ductile thumbnail extension values, lateral expansion and decreased crystalline area. A similar trend was also observed for temperature versus increased ductile thumbnail, lateral expansion and decreased crystalline area.

Chapter 7 - Results – Slow Notched Bend Tests.

7.1 Introduction

Slow blunt notch bend tests were performed at -196°C on Weld N^o2 only, to assess the effects of both microstructures and in both the AR and the 5%SA conditions on the cleavage fracture stress, which is the measure of resistance to cleavage. Slow blunt notch bend tests are used to obtain the intrinsic cleavage fracture stress of a material, and in this case have been applied to the AD and RH microstructure to analyse the effect on weld metal regions of the local brittle fracture stress of the AR and 5%SA conditions. The results from the Charpy impact results showed very little difference in the lower shelf regions of the impact transition curves between the different microstructural conditions; hence these tests have been applied to gain a greater understanding of the mechanisms of the cleavage fracture behaviour in both the AD and RH microstructures.

Four point bending was used for the testing specimen arrangement, all the specimens tested at -196°C failed before the general yield limit as predicted by Griffiths and Owen [163]. Results from the slow blunt notch bend tests are a good assistance for explaining the temperature transition behaviour of both the weld metal regions in the 5%SA conditions. Groom and Knott [47] found that prestraining causes small increases in fracture stress in mild steel. An increase in the transition temperature was the result of the increase in yield stress due to work hardening to overcome this problem and the net effect was an increase in the transition temperature. It is therefore important to find if this is valid for the weld metal used in this work, also investigated is slow blunt notch bend tests were performed for both weld microstructures in the 5%SA condition to indirectly measure any possible embrittling effect

of copper precipitation and/ or grain-boundary segregation of impurity elements that might have occurred during ageing at 300°C on the intrinsic cleavage fracture stress.

7.1.1 Results

A photograph of a slow blunt notch testpiece is shown in Fig. 7.1, the specimen measures 10 x 10 x 55mm with a notch located at the centre of the specimen. The specimens were EDM machined (wire eroded), Fig. 7.2 shows three photomicrographs of the notch from the ADAR, RHAR, AD5%SA and the RH5%SA conditions, it can be seen how accurately the notches have been produced, which is critical for this experiment. Load displacement data was obtained for Weld N^o2 for both the AD and RH microstructures in both the AR and 5%SA conditions. The data was recorded using a chart recorder and noting the fracture loads, P_{max} , for tests conducted at -196°C, these traces are not included in this work, these experiments were carried out on Dension Meyes machine fitted with a 50kN load cell. It can be seen that in general the AD microstructure exhibited lower fracture loads, than the equivalent RH microstructure. Fig. 3.22 shows Griffiths and Owen [163] analysis calculated through FEM to find the variation in stress intensification ratio ($R = \sigma_{yy_{max}}/\sigma_y$) below the notch root for different loads, Fig. 3.21 shows the variation in stress intensification with applied load. These figures have been used to calculate from the experimental results the local cleavage fracture stress σ_{X_0} , as well as values of X_0 distance being obtained from fractography, these are presented in Table 7.1 and summarised in Table 7.4 for both weld metal microstructures and both conditions.

Fig. 7.3 illustrates local cleavage fracture stress, σ_{X_0} , it can be seen that the AR weld metal microstructures are higher than those observed for the 5%SA materials. Local cleavage fracture stress, σ_{X_0} , range from 1514 to 1940MPa for the ADAR condition compared with 2003 to 2221MPa from the RHAR condition, this is in contrast to 1629 to 1786MPa and 1739 to 1869MPa for the AD5%SA and the RH5%SA microstructural condition respectively. One specimen, ADAR1 failed extremely early at 11.70 kN, upon further analysis and fractography it was found to have an extremely large slag inclusion, close to the notch root.

For the AD microstructure the mean values for the local cleavage fracture stress, σ_{X0} , calculated using the cleavage fracture initiation site (CIS), decreased from 1910MPa at -196°C in the AR condition to 1710MPa in the 5%SA condition. Similarly for the RH microstructure there was also a decrease in the mean values for local cleavage fracture stress, σ_{X0} , from 1808MPa for the RH 5%SA condition compared with 2078MPa for the RHAR condition. In general the AD microstructure exhibited lower σ_{X0} values than the RH microstructural region for equivalent conditions. No significant difference in the mean σ_{X0} values are found for either the RH or AD microstructures after prestraining and ageing.

Using Griffith and Owen [163] FEM analysis and equation 4.16 the maximum principal tensile stress, $\sigma_{yy\max}$, was calculated for the two microstructures; AD and RH, in both conditions, AR and 5%SA are presented in Table 7.2 and 7.3, for the AR and 5%SA conditions respectively, these tests were carried out at -196°C. All results are summarized in Table 7.4 and plotted in Fig. 7.4, the $\sigma_{yy\max}$ data for the ADAR microstructural condition ranged from 1600 to 2196MPa compared with 1747 to 1858MPa for the AD 5%SA condition. Both the RHAR and the RH 5%SA conditions exhibited an increase in the $\sigma_{yy\max}$ values ranging from 2118 to 2291MPa and 1866 to 2258MPa for the RHAR and the RH 5%SA conditions respectively. It can be seen that the AD microstructure exhibits lower maximum principal tensile stress values than the RH microstructure for similar conditions. For the AD microstructure, the mean principal tensile stress values $\sigma_{yy\max}$ decrease slightly from 1989 to 1795MPa for the AR condition compared to the 5%SA condition. However from the RH microstructure there is a slight increase in the mean maximum principal tensile stress from 2212MPa in the AR condition to 1994MPa for the 5%SA condition. Again the AD microstructures from equivalent conditions exhibited lower $\sigma_{yy\max}$ maximum principal tensile stress values compared to the RH microstructure.

Plotted in Fig. 7.5 is the relationship between local cleavage fracture stress, σ_{X0} , and the maximum principal tensile stress, $\sigma_{yy\max}$. Ideally, there would be a perfect correlation between these values, if σ_{X0} occurred at the exact position of the maximum principal tensile

stress. Clearly from this figure they are close proximity, but not exact. Fig. 7.6 illustrates the location of relevant cleavage fracture initiation sites plotted against the FEM analysis of the stress intensification factor R versus X_0 , the distance below the notch, at various loads, with a notch root radii of $200\mu\text{m}$. It can clearly be seen for equivalent microstructural conditions that the AD microstructural specimens fail at lower values of R than the RH microstructural conditions. The AD5%SA weld metal condition and the RHAR are the worst and best conditions respectively, with the AD5%SA condition exhibiting the lowest values of R and the shortest X_0 distances, compared to the RHAR weld metal condition which exhibited the larger values of R with longer X_0 distances. In Fig. 7.6, it can now be seen that sites occur closer to the notch than the position of maximum tensile stress.

From the FEM analyses, the values of stress intensification ratio, R ($\sigma_{yy\text{max}}/\sigma_y$) were calculated, and are presented in Fig. 7.7. The R value range for the ADAR microstructural condition was 1.84 to 2.52 and this decreases after 5%SA to 1.77 to 1.88 (AD5%SA). Mirroring this, the RHAR has a R value range of 2.42 to 2.63 compared to 2.01 to 2.42 for the RH5%SA microstructural condition. Thus the AD microstructure exhibits lower stress intensification values and therefore has less resistance to cleavage initiation and fracture than the RH microstructure for all conditions studied. It can also be inferred from the diagram there is a significant reduction in the mean R from the AR condition compared to the 5%SA condition, for both microstructures, also explaining why 5%SA condition has lower resistance to cleavage fracture. For the purpose of interpreting the data, R values above 2.62 have been discounted, (RHAR5).

The X_0 distance for the all weld meal conditions is shown in Fig. 7.8, it can clearly be seen that both the AD microstructural conditions exhibited small X_0 values compared with the respective RH microstructural conditions. The X_0 values for the ADAR microstructure ranged from 187 to $245\mu\text{m}$ compared to 236 to $320\mu\text{m}$ for the RHAR microstructure, these both decrease to 189 to $212\mu\text{m}$ for the AD5%SA condition and 201 to $244\mu\text{m}$ for the RH5%SA condition. Using the FEM analysis obtained by Griffiths and Owen, as shown in Fig. 7.9, illustrates the spread of plasticity, x , below the notch root at various loads. Using

this graph it is possible to estimate the size of the plastic zone region underneath the notch root for the various microstructural conditions, these results are plotted in Fig. 7.10. The RHAR microstructural condition exhibits both the higher x values and the largest amount of plastic spread, compared with the AD5%SA weld metal condition which exhibits the smallest plastic region ahead of the blunt notch and the lowest x values. Straining and ageing the weld material appears to effect to the spread of plasticity. It is clear that a single cleavage initiation site is more distant from the blunt notch root (higher X_0 values) for larger spread of plasticity. The RH microstructure in the AR condition exhibited the largest spread of plasticity and therefore the AD5%SA microstructural condition exhibits the smallest plastic region.

7.2 Fractography

Extensive fractography has been carried out on the blunt notch specimens, on both halves of the fracture surfaces. Examination of the blunt notch fracture surfaces involved location the site of cleavage initiation (CIS) and the measure of initiation features (non-metallic inclusions) from the notch root (X_0).

The broken halves of two fracture surfaces are shown in Fig. 7.11 these specimens were tested at -196°C and sampled the AD and the RH microstructure. In general there was 100% coverage for the RH microstructure samples, compared with the AD microstructure, which dependant upon the notch location in relationship to the sample had approximately 45% coverage. The area of coverage for the AD microstructure is consistent for both the Charpy specimens and CTOD specimens which were tested within the lower shelf where brittle fracture is more predominant. It should be noted that the notch region and the plastic zone, formed during loading ahead of the notch only sampled a single microstructural condition either AD or RH.

All the specimens from both the AR and 5%SA conditions for both microstructures were examined. Overall it was more difficult to locate the cleavage initiation sites in the RH weld metal region compared to those in the AD weld metal region because of to the finer microstructural nature of the RH microstructure. Although not measured carefully as part of this study, it was clear that the AD microstructure exhibited larger cleavage facets than those observed in the RH microstructure.

Fig. 7.12 through to 7.21 show examples of fractography taken during the analysis of the blunt notch samples. Fig. 7.12 shows the fracture surface of RHAR4, the overall fracture surfaces is shown with the distinctive river lines to the cleavage initiation site. At the centre of the cleavage initiation site is a void Fig. 7.12(d) also labelled is some secondary cracking Fig. 7.12(c). Fig. 7.13 shows an ADAR fracture surface, again there are the distinctive river lines indicting the cleavage initiation site. A distinctive fracture surface feature of the AD microstructure are cleavage steps, Fig. 7.13(c). Also shown is a decohered inclusion on the fracture surface Fig. 7.13(d). An example of the overall fracture surface of an AD5%SA microstructural condition is shown in Fig. 7.14(a), the cleavage initiation site is clearly seen with an inclusion located at the centre of the CIS Fig. 7.14(c). Fig. 7.15 shows an example of a RH5%SA microstructure fracture surface, the cleavage initiation site is shown in Fig. 7.15(c) and 7.15(d), however this sample seems to have two initiation sites close together, therefore it would be hard to establish which initiated cleavage fracture in the specimen.

Fig. 7.15 to 7.21 exhibit more examples of cleavage initiation and fracture surfaces for a range of samples. The cleavage initiation sites are generally characterised by macro and micro-river lines, cleavage steps generally observed in the AD microstructure, secondary cracking and decohered inclusions. X_0 distance values for both microstructures in the AR and 5%SA conditions are plotted in Fig. 7.8. Generally the RH microstructure exhibits higher X_0 values than the AD microstructure for equivalent conditions. It should therefore be noted that all slow blunt notch bend tests were carried out at -196°C and changes in X_0 are hence related to only to the different microstructural conditions.

7.3 Discussion

7.3.1 Blunt Notch Tests

Slow blunt notch tests, carried out at liquid nitrogen temperature -196°C , in four point bending allow the effects of different microstructural conditions on the resistance to cleavage of the weld metal. The discussion will focus on local cleavage fracture stress, σ_{X0} , depending on microstructure; this is as a result of differences being found between the AD and RH microstructures, for both the AR and 5%SA condition. Events are to be considered on a microstructural scale. The relation of fracture toughness to local cleavage fracture stress relies on the identification of “critical distance” [203] when dealing with the difference microstructures and the two different conditions. Despite the relatively small quantity of specimens tested in each microstructure, the fine grained RH microstructure presented considerably higher cleavage fracture resistance than the AD microstructure.

The discussion is based on the evaluation of some of the microstructural features of both microstructures; e.g. non-metallic inclusion sizes (2D distribution) as well as measured facet sizes from the cleavage initiation sites with the “local” Griffith criterion equation approach. Changes in flow properties of both weld metal regions after prestraining and static strain ageing are used to explain lower localised cleavage fracture stress of the AD microstructure. Also considered, is the statistical nature of sampling potent inclusions of radius sufficiently large enough to propagate a micro-crack (penny shaped) through the matrix.

7.3.2 Previous proposed model for cleavage fracture in C-Mn weld metal.

Tweed and Knott [143] proposed a model for cleavage fracture in C-Mn weld metal; based on results from their limited investigation. Their experimental results also indicated the same

basic concept can operate in both AD and fine-grain RH weld metal microstructures. Previous research has also reached similar conclusions for C-Mn and low-alloy ferritic steel weld metals [13-15]. Essentially the model requires prior plasticity to crack an inclusion, followed by catastrophic failure from such unique initiation sites.

The effects of prestrain and strain ageing on cleavage fracture in mild steel [47] and C-Mn [230] steels assessed using single-edge-notched specimens in slow bending established that temperature at which fracture is coincident with general yield increases as a consequence of these treatments. This implied that prestrain and strain ageing treatments promote brittle fracture to higher temperatures. In the current work, unique initiation sites at inclusions have been established in many cases. This allows the local cleavage fracture stress, σ_{X0} , to be predicated accurately from the Griffiths and Owen stress analysis [163], see Fig. 7.3 and Fig 3.22. Here, there is no increase in cleavage fracture stress as a consequence of strain ageing. Indeed, based on the mean values obtained for σ_{X0} , Table 7.1, there appears to be a decrease in σ_{X0} after strain ageing. Table 7.1, also suggests that the RHAR microstructure, has increased σ_{X0} than the ADAR microstructure. The RHAR microstructure in both conditions exhibits increase σ_{X0} compared to the AD microstructure.

7.3.3 Static strain ageing effect on cleavage fracture.

Cleavage fracture in low-alloy ferritic steel weld metals is controlled by the development of tensile stress ahead of a stress concentrator. When load is applied to a testpiece, the elastic/plastic strain ahead of the stress concentrator within the process region increases shown in Fig. 3.22 [163], thus nucleating a microcrack in brittle non-metallic inclusion or second phase particle, this propagates on the attainment of the critical tensile stress. This cleavage stress is considered to be temperature independent [7, 9-11, 52, 152, 153]. The materials flow properties control the cleavage fracture resistance within the material, other influencing factors are the distribution of non-metallic inclusions and microstructural parameters, such as grain size and microstructural constituents, found within the highly stressed zone ahead of the blunt notch. Both the as-deposited and reheated microstructures possess similar inclusion

distributions, with static strain ageing not effecting or modifying the 2D inclusion size distribution, as shown in Table 5.2 and Fig. 5.11 and discussed in Chapter 5.2.2. As a result it can be inferred that there are two factors which could be controlling/ influencing cleavage fracture resistance of the weld microstructure: (i) the microstructural parameters (e.g. grain size, inclusion size distribution, microconstituents) within the process zone ahead of the crack tip and (ii) plastic behaviour e.g. yield stress σ_y and work hardening exponent n .

7.3.4 Plastic deformation and strain ageing in low alloy ferritic steel weld metal.

During this current work it has again been shown that plasticity is required, but is not a sufficient condition for the onset of cleavage fracture, as the fracture stress in tension at -196°C is greater than the yield stress for all weld metal conditions. Mean $\sigma_{yy\max}$ values at -196°C were 1989MPa and 2212MPa for the ADAR and the RHAR conditions, compared to yield stress values of 863 MPa and 901MPa for the same conditions respectively. This trend was the same for the 5%SA condition, with the AD and RH microstructures exhibiting yield stress values of 885MPa and 987MPa at -196°C , corresponding $\sigma_{yy\max}$ values were 1795MPa and 1994MPa, shown in Fig. 6.11 and 6.17, Tables 7.2 and 7.3. This underlines the observation in Chapter 5.3.2 that yield stress and σ_{X0} and $\sigma_{yy\max}$ are not representative of the weld metal as a whole due to the inhomogeneous nature of the material.

It would be reasonable to deduce that plasticity preceded cleavage fracture in the weld metal, this was also inferred by Tweed and Knott [7, 143] for C-Mn weld metals. This is also confirmed by the fact that local cleavage fracture stress values are localised within the plastic process zone ahead of the blunt notch root. Also, in the same study, Tweed and Knott [7, 143] observed that if total strain in the material is relatively low, roughly smaller than 7%, then strain is perhaps more easily accommodated by deformation of grain boundary ferrite, which is a relatively soft constituent. It has also been suggested that the cleavage initiation micromechanism at lower strains could be associated with plastic deformation solely in the

grain boundary ferrite constituent [7]. Previous authors and research [7, 13, 14, 52, 71, 113] has highlighted the deleterious effect on fracture toughness of C-Mn steels and weld metals and also in Mn-Mo-Ni steel weld metals [14, 15] due to the occurrence of grain boundary or allotriomorphic ferrite constituents in the materials microstructure. More recent research [14, 15] has also concluded that initiating inclusions were located within large allotriomorphic grains in a C-Mn weld metal within the AD microstructure. This is in agreement with the results from previous research [15] and observed during this current work, however these were not measured as this would be outside the current scope. The fractography presented here revealed that initiating inclusions are located within larger allotriomorphic ferrite grains in the AD microstructure and this is in good agreement with previous authors [14, 15]. However it should be noted that both microstructures presented similar inclusion size distributions, Chapter 5.2.2. In the RH microstructure the initiating inclusions were still located within larger cleavage facets; however these were smaller than the corresponding allotriomorphic ferrite grains in the AD microstructure. It should also be noted that a similar trend was also identified during fractographic examination of tensile, Charpy and CTOD fracture surface samples and examining cleavage initiation sites of both microstructures.

Assuming that inclusions crack under the influence of a dislocation pile-up and the stress magnitude depends on the length of the dislocation pile-up, then a large allotriomorphic ferrite (generally found in the AD) would be more detrimental to cleavage fracture resistance than the small equiaxed grains (generally found in the RH microstructure), since the allotriomorphic constituent would contain longer dislocation pile-up lengths. If global prestraining procedure is uniform, then the total stress applied during the cold deformation should be more equally distributed in the RH microstructure (due to its equiaxed ferrite grains) compared to the AD microstructure where total strains may be more accommodated by deformation of grain boundary ferrite than of other constituents such as acicular ferrite. Hence, large allotriomorphic ferrite grains and long dislocation pile-up lengths may explain why the AD microstructure is more sensitive to static-strain ageing than the RH microstructure and therefore presenting a lower cleavage fracture resistance.

The importance of the facet size parameter in reducing the cleavage fracture resistance of the weld metal is in agreement with early dislocation models for cleavage fracture of a polycrystal, where cleavage fracture stress is related to the materials grain size through the Petch [178] model for yielding. However, the influence of facet size in allowing the easier propagation of a microcrack from grain to grain ensures that this debate will run for many decades to come.

7.3.5 Relative position between maximum principal tensile stress ($\sigma_{yy\max}$) and the cleavage initiation site.

Maximum tensile stress, $\sigma_{yy\max}$, is shown (Fig. 3.22) below the notch root [163]. From the analysis it is possible to see that the peak $\sigma_{yy\max}$ is always located behind the elastic/ plastic interface and moves further as the load is applied from the notch root, and plastically spreads. The results of this current work have shown that most of the cleavage initiation sites are located in close proximity to, but closer to the notch than, the peak tensile stress, as predicted from the finite element analysis, as shown in Fig. 7.6. Specimens sampling the AD microstructure exhibit lower stress intensification values than those sampling the RH microstructure for both the AR and 5%SA conditions. This is due to the higher yield stress values and the lower values of σ_{X0} exhibited for the AD microstructure compared to that of the RH for a similar conditions Fig.7.7. The consequence is that less stress intensification, R, is needed to attain the critical fracture stress. In addition, all the catastrophic cleavage events are located above the 85% $\sigma_{yy\max}$ level for both of the weld metal microstructures and for all conditions studies in this current experimental programme. This demonstrates that cleavage fracture starts reasonably close to the maximum local tensile stress and within the area covered by 85% of $\sigma_{yy\max}$, this tends to support the critical stress controlled criteria for cleavage fracture initiation from non-metallic inclusions.

All the specimens tested at -196°C failed within the plastic zone, this is essential as the strain and ageing procedure affects the deformation properties of the weld metal conditions, as

previously discussed in Chapter 6.4. This result offers good support from the different response of mean X_0 distances exhibited from the AR condition and the 5%SA condition for both microstructures. The distance X_0 , which is between the blunt notch root and the cleavage initiation site (CIS), depends on the microstructural condition of the weld metal. The AD microstructure generally exhibits shorter X_0 distance than the RH microstructure for equivalent conditions. It also exhibited smaller X_0 shifts in both the AR and 5%SA condition than the RH microstructure Fig. 7.6. In short these results reinforce the fact that the RH microstructure exhibited a greater local cleavage fracture stress, σ_{X_0} than the AD condition for similar microstructural conditions. Thus it is crucial that the stress intensification ratio is increased to higher levels in order to reach the required local cleavage fracture stress. As a consequence the size of the plastic zone becomes larger and the cleavage initiation sites (CIS), the distance X_0 shifts further away from the root of the blunt notch (for the RH microstructures).

The tensile stress criterion predicts that catastrophic cleavage fracture occurs in slow blunt notch bend testing when the stress intensifies. Thus the principal local tensile stress overcomes the intrinsic cleavage fracture stress at a potent initiation site, for example a non-metallic inclusion, which is located ahead of the blunt notch in the plastic process zone. The variations in the experimental results for X_0 for all the microstructural conditions could be explained by the possibility of sampling a inclusion of a given size ($\leq 3.5\mu\text{m}$) in the high stress region.

In conclusion the AD weld metal microstructure exhibits lower local cleavage fracture stress values, σ_{X_0} compared to the RH microstructure. This is deduced to be due to the RH microstructure having small facet sizes at the cleavage initiation sites, for similar inclusion size distribution between the weld metal regions. Also any small changes in local cleavage fracture stress, σ_{X_0} , are observed for both microstructures after the static strain ageing procedure, shown in Fig. 7.3, with an increase in the yield stress. This contributes to early onset of catastrophic cleavage fracture in both weld microstructures and conditions and this supports shifts in DBTT after static strain ageing.

Therefore, despite cleavage fracture stress remaining practically the same after the strain and ageing procedure, the cleavage fracture resistance of both microstructures, (mainly in the AD5%SA microstructural condition) is expected to be reduced due to an increase in yield stress. Chapter 8 explores in more detail the relationship between local cleavage fracture stress σ_{X0} and yield stress σ_y with the cleavage fracture resistance of the weld metal in the presence of a sharp crack, together with the transition shifts obtained from the Charpy impact tests.

7.3.6 Relationship between inclusion size and local cleavage fracture stress, σ_{X0} .

By applying a modified Griffith relation, Curry and Knott [158, 191, 231], have inferred the fracture stress of spheriodised carbides by treating microcrack propagation from microstructural constituents as propagation of a penny shaped crack. Using the modified Griffith equation, presented in Section 4.2.9, to estimate the fracture stress for non-metallic inclusions and evaluate cleavage fracture resistance of weld metal. Inclusion sizes and corresponding facet sizes were not evaluated in detail as part of this current work. However using Griffiths and Owen [163] to evaluate local cleavage fracture stress σ_{X0} values, these can be plotted against the reciprocal square root of the inclusion size located at these cleavage fracture initiation sites see Fig. 7.6, for each microstructural condition. From this figure an effective surface energy, γ_p , can be estimated by using equation 4.17.

Previous research [14, 15] using Weld N^o1 has shown that effective surface energies for both the AR and 5%SA conditions in the AD microstructure was 7.6Jm^{-2} and 8.0Jm^{-2} for the RH microstructure. Wenman [14], using a similar composition of material also noted a comparable mean value γ_p of 7Jm^{-2} in the AR weld metal condition, with previous authors for a value of γ_p in “classical weld” metal microstructures 9Jm^{-2} [22] and numerous types of plate materials containing carbides 14Jm^{-2} (Curry and Knott [155, 158, 231]) and 4.3 to 6Jm^{-2}

(Bowen [10, 11]). The relationship between the reciprocal square root of the inclusion diameter and local cleavage fracture stress, here, very weak. Thus for the onset of cleavage fracture to occur the size of the inclusion is a necessary constituent but not fundamental, as the majority of non-metallic inclusions vary in size from 1.1 to 4.5 μm , as shown in Fig. 5.21.

Nevertheless fractography did show that the facet sizes at the cleavage initiation site were visibly larger in the AD microstructure than those observed in the RH microstructure. Thus cleavage initiation sites with larger facet sizes, as exhibited in the AD microstructure are deduced to be explainable for the poor cleavage fracture resistance of this microstructure, compared to the fine equiaxed RH microstructure.

7.4 Conclusions

1. The AD microstructure exhibited slightly lower local cleavage fracture stress, σ_{X0} , values than the RH microstructure for similar conditions. Mean values of σ_{X0} were 1910MPa and 2078MPa for the ADAR and RHAR conditions respectively. After strain ageing, mean values of σ_{X0} were 1710MPa and 1808MPa for the AD5%SA and RH5%SA conditions, respectively. Thus local cleavage fracture stresses for both weld metal microstructures were slightly reduced after prestraining and statically strain ageing.
2. Locations of cleavage initiation sites for all microstructural condition were located within the plastic zone ahead of the blunt notch and close to the predicated position of maximum principal tensile stress in the specimen.
3. Non - metallic inclusions were found to be the primary cleavage initiation factors for cleavage fracture to occur. These were from the upper tail of the inclusion size

distribution and were of similar sizes in both microstructures. It was also observed in the weld metal, that the RH microstructure visually exhibited considerably smaller cleavage facets sizes compared to those of the AD microstructure at cleavage initiation sites.

Chapter 8 - Results - Crack Tip Opening Displacement (CTOD) Tests.

8.1 Introduction

This chapter explores the effect of static strain ageing on the CTOD behaviour of small - scale specimens, for both weld metal microstructures across a test temperature range of -196°C to 20°C to compare their resistance to stable crack growth extension and brittle fracture. Examination of the effect of initial pre-crack length on the type of fracture obtained are investigated in some detail. Fractography was carried out on the fracture surfaces of the specimens to confirm that the fatigue precrack tip was properly located within the desired microstructure; checks were also made to ensure that the corresponding physical crack extension had propagated within the same microstructure. In Chapter 9, results are compared to Charpy, tensile and slow blunt notch tests.

8.2 Results

8.2.1 Fatigue pre-cracking.

Upon completion of the CTOD tests, the fatigue pre-crack length was measured at nine equally spaced positions along the crack front, as described in section 4.9. The average pre-crack length, a_0 , is used to calculate the CTOD value, shown in Tables 8.1 to 8.18. Also

shown are $\frac{a_0}{W}$ values, where W is the width of the specimen, which is also used to calculate CTOD values. British standard BS7448: Part 4, 1991 requires that the crack length, a_0 should be within the range of 0.45 to $0.55 \frac{a_0}{W}$. Due to the weld microstructure and the weld bead height measuring between 0.45 to 0.55mm for Weld N^o1 and 0.33 to 0.45mm for Weld N^o2 it was not possible to meet the requirements of the British Standard. This is due to the need the fatigue precrack and any stable crack growth to be within the designated microstructure, as previously discussed in section 4.9.

8.2.2 CTOD Results for Weld N^o1.

CTOD test results for Weld N^o1 are shown in Tables 8.1 to 8.4 and have been assigned the correct δ_c , δ_u and δ_m designations where:

- δ_c - critical CTOD at the onset of brittle crack extension when Δa is less than 0.2 mm;
- δ_u - critical CTOD at the onset of brittle crack extension when Δa is equal to or greater than 0.2 mm;
- δ_m - value of CTOD at the first attainment of a maximum force plateau for fully plastic behaviour.

A total of 42 AR specimens were tested, 20 ADAR specimens and 22 RHAR specimens and 32 specimens in the 5%SA conditions, consisting of 15AD5%SA specimens and 17 RH5%SA specimens. These results are presented in Fig. 8.5 to 8.7. Load versus clip gauge displacement curves are illustrated in Fig. 8.1 to 8.4 for all specimens, for all four microstructural conditions.

ADAR microstructure CTOD values ranged from 0.005 to 0.368mm across the temperature range of -196 to 20°C. Across this same temperature range the RHAR microstructure exhibited CTOD values of 0.003 to 0.582mm. As with previous experiments carried out during this programme the 5%SA condition exhibited lower CTOD values when compared to the AR conditions. CTOD values ranged from 0.022 to 0.058mm and 0.007 to 0.263mm for the AD5%SA and the RH5%SA microstructural conditions respectively, across the temperature range of -120 to 20°C.

As illustrated in Fig. 8.5 to 8.6, the ADAR microstructural condition exhibited δ_c values ranging from 0.005 to 0.060mm across the temperature range of -196 to -100°C. One specimen, ADAR specimen 1, exhibited a δ_c value of 0.128mm tested at room temperature. This specimen failed extremely early, the reason for the cause of failure was unknown, so was investigated further on the SEM. δ_u values ranged from 0.070 to 0.280mm across the temperature range of -80 to -40°C, whilst the δ_m values across the temperature range of -60 to 20°C ranged from 0.150 to 0.368mm. In comparison, the majority of the RHAR samples were δ_m values; these ranged from 0.289 to 0.594mm for -80 to 20°C, only 4 samples exhibited δ_u values across the temperature range of -100 to -40°C, these ranged from 0.091 to 0.408mm. There were only three δ_c specimens with CTOD values ranging from 0.003 to 0.064mm across the temperature range of -196 to -120°C, shown in Fig. 8.5 and 8.6.

The AD5%SA microstructural condition only exhibited two δ_m values, both at 20°C, of 0.119 and 0.100mm, δ_c values ranged from 0.004 to 0.027mm from -120 to -60°C and there were 5 specimens that exhibited δ_u values ranging from 0.050 to 0.084mm for the temperature range of -40 to 20°C, shown in Fig. 8.5 and 8.7. Finally the RH5%SA microstructural condition exhibited 4 specimens with δ_c values at -120 to -60°C, exhibited CTOD values of 0.005 to 0.085mm compared with δ_u values ranging from 0.099 to 0.193mm across the temperature range of -60 to -40°C, with δ_m CTOD values ranging from 0.204 to 0.276mm for -40 to 20°C, as shown in Fig. 8.5 and Fig. 8.7. It should be noted that the δ_m value is sensitive to the remaining ligament size and specimens with similar values of original crack length should be compared to establish any trends within these results. Also the amount of stable crack growth

length, Δa was not measured here given that testpieces were past general yield (plastic collapse).

Fig. 8.8 shows the amount of stable crack growth (where measured) plotted against the CTOD value, (values for the amount of stable crack growth are shown in Tables 8.1 to 8.4). The stable crack growth ranged from 0 to 0.545mm for the ADAR microstructural condition, compared with 0 to 0.426mm for the RHAR microstructural condition. Stable crack growth for the 5%SA condition ranged from 0 to 0.410mm and 0 to 0.268mm for the AD5%SA and RH5%SA microstructures respectively. Fig. 8.9 illustrates that the increasing temperature corresponds with an increase in the amount of stable crack growth. It can be seen that at -80°C that the AD5%SA and RH5%SA microstructural conditions both exhibited δ_c values, with both of the AR microstructural conditions exhibiting δ_u values. It can be seen that at lower temperatures all four of the conditions exhibited δ_c values. As the temperature increases a mixture of δ_c and δ_u values are exhibited in the transition region. There was mixture of δ_u and δ_m values on the upper shelf region, δ_m values are not plotted on this graph as stable crack growth was not measured for these samples (since taken past general yielding).

8.2.3 CTOD Results for Weld N^o2.

The test results for Weld N^o2 are shown in Tables 8.5 to 8.8, have been summarised and assigned the correct CTOD designations. 42 AR specimens, 20 AD and 22 RH specimens were tested and 25 specimens in the 5%SA condition, 12 AD and 13 RH specimens. Figures 8.10 to 8.13 exhibit the load versus clip gauge displacement graphs for the four microstructural conditions while Fig. 8.14 to 8.16 exhibits the CTOD values plotted against temperature. It is clear from the Figures presented here and for Weld N^o1 that AD5%SA microstructural condition exhibits lower work-hardening exponent and a higher maximum load plateau compared to the AR condition. This behaviour is a result of higher yield stress levels and low ductility exhibited by the 5%SA condition.

CTOD values ranged from 0.027 to 0.538mm for the ADAR microstructural condition across the temperature range of -140 to 20°C, across the same temperature range the RHAR microstructure exhibited CTOD values of 0.086 to 0.811mm. The 5%SA condition again exhibited the lower CTOD values when compared with the AR condition. For the AD5%SA condition the CTOD values ranged from 0.026 to 0.455mm and 0.034 to 0.561mm for the RH5%SA condition as the same temperature range as the AR condition. The ADAR microstructural condition across the temperature range of -120 to -80°C, δ_c exhibited values ranging from 0.027 to 0.072mm. Values for δ_u ranged from 0.066 to 0.246mm across the test temperature range of -80 to -40°C, whilst δ_m values ranged from 0.303 to 0.538mm for the temperature range of -40 to 20°C. As with the results in Weld N^o1, the majority of specimens for the RHAR microstructural condition for Weld N^o2 exhibited δ_m values, these ranged from 0.510 to 0.811mm, across the temperature range of -60 to 20°C. Only six specimens exhibited δ_u values and these ranged from 0.248 to 0.509mm for the temperatures -80 to -60°C. Across the temperature range of -120 to -100°C there were seven RHAR specimens with δ_c values noted and these ranged from 0.086 to 0.292mm.

Again for Weld N^o2 the 5%SA condition exhibited the lowest CTOD values, the AD5%SA condition exhibited two δ_m values ranging from 0.402 to 0.455mm, both at room temperature. Three δ_u values were observed from -60 to -20°C which exhibited CTOD values of 0.230 to 0.321mm. The majority of the specimens exhibited δ_c ranging from 0.026 to 0.151mm across the temperature range of -120 to -60°C. The RH5%SA microstructural condition exhibited two δ_m values at room temperature ranging from 0.499 to 0.561mm. δ_u values range from 0.173 to 0.381mm across the temperature range of -60 to -20°C and δ_c values from 0.034 to 0.170mm across the temperature range of -120 to -60°C.

The amount of stable crack growth is plotted against CTOD values, as shown in Fig.8.17 and Tables 8.5 to 8.8. The stable crack growth ranged from 0 to 0.317mm for the ADAR microstructural condition compared with 0 to 0.299mm for the RHAR microstructural condition. For the 5%SA microstructural condition the stable crack growth ranged from 0 to 0.325mm and 0 to 0.363mm for the AD5%SA and RH5%SA microstructures respectively.

Fig. 8.18 illustrates the stable crack growth plotted against temperature, following the same trend as Weld N^o1; the amount of stable crack growth increases with increasing temperature. δ_c values are exhibited on the lower shelf, as the temperature rises up through the transition region there is a mixture of all three CTOD designations with δ_m values defining the upper shelf.

8.3 Fractography

Fractography was carried out on selected specimens for the RH and AD microstructural conditions in both the AR and 5%SA conditions. Some fractography was carried out on both weld metals, but attention is given to Weld N^o2 and particularly to testpieces which presented some areas of cleavage fracture. It was also essential to check the fatigue pre-crack tip in relation to the weld microstructure and the position of the corresponding physical crack extension. Fig. 8.19 and Fig. 8.20 show typical fracture surfaces for both the AD and RH microstructures, clearly illustrating that the fatigue pre-cracks were properly located within the desired location and microstructures (AD or RH). A number of specimens exhibited irregular stable crack extension prior to the onset of transgranular cleavage fracture. In the case of the RH microstructure the fatigue precrack tip and corresponding stable crack extension are always located within this microstructure. This is mainly a result of notch positioning with respect to weld cross-section, which only samples this microstructure.

Fractography for some of the specimens are presented in Fig. 8.21 - Fig. 8.34. As previously discussed for the tensile and Charpy specimens, the fracture surfaces are characterised with many of the same features. Fig. 8.23 shows fractography carried out on Sample 31, ADAR Weld N^o1, where both sides of the fracture surface were examined, secondary cracking was noted close to the cleavage initiation site (CIS). Fig. 8.25 exhibited a large amount of ductile tearing as well as cleavage steps. Sample 5, RH5%SA, Weld N^o2 exhibited a large secondary crack, initiating from the CIS. Some samples presented stable crack growth followed by transgranular cleavage, mainly for the AD microstructure. The remaining specimens

exhibited stable crack growth, with no cleavage fracture mechanism both the specimen reached the maximum load plateau. On some specimens it was possible to trace back river lines on large grain boundary ferrite cleavage facets to a distinct initiation site, Fig. 8.21 and Fig. 8.23.

The micromechanism of fracture in the stable crack growth regions of all the microstructures and conditions was microvoid coalescence formed around non-metallic inclusions, as shown in Fig. 8.22, Fig. 8.26, Fig. 8.31 and Fig.8.33. Examination by fractography of these testpieces which had failed by fracture instability showed that this was a result of the onset of brittle fracture by transgranular cleavage. The AD specimens for both the AR and 5%SA conditions displayed a wide distribution of cleavage facet sizes.

The AD microstructural fracture surfaces are characterised by a “rough” appearance resulting in shallower voids, this is due to the morphology of the microstructure. Within the RH microstructural condition the cleavage facets were more uniform in appearance; this resulted in a “finer” surface appearance for the cleavage fracture surface. These small facets crack propagation more difficult as the crack must change direction more often, shown in Fig. 8.22 and 8.26 for the RHAR and ADAR conditions respectively. Previous [15] research carried out on the same weld metal also noted that there were visually shallower voids for the RH microstructure compared to those of the AD microstructure. Theory also suggests that dislocation pile-up causes the inclusion to crack and nucleate a microcrack, limiting the pile-up length is the grain size (equivalent to the facet size). Cleavage initiation sites were identified by tracing back diverging river lines. The majority of these testpieces showed that cleavage initiation occurred in non-metallic inclusions located within large cleavage facets, these are shown in Fig. 8.21 and Fig. 8.27.

The McMeeking [232] analysis of the stress distribution ahead of the blunted crack-tip shows that the peak tensile stress occurs at a distance of 1.9δ , where δ is CTOD. Fractography was carried out on the fracture surfaces to measure the distance of the initiation site ahead of the

ductile crack-tip. The results are shown in Tables 8.9 to 8.13 for both weld metals in all four conditions, good correlation was found between the predicted site from the McMeeking [232] analysis and the actual measured site. Fig. 8.35 and Fig. 8.36 illustrate the results plotted against temperature for Weld N^o1 and Weld N^o2 respectively. Generally, the actual sites were located slightly ahead of the position of peak tensile stress predicted by the McMeeking analysis.

8.4 Discussion

8.4.1 CTOD values.

The effects of plastically deforming and statically strain ageing the A533B Class 1 weld microstructures has been assessed through CTOD tests. The tests were carried out on weld metals for both microstructures; AD and RH and both microstructural conditions; AR and 5%SA. The tests were carried out over the temperature range of -196 to 20°C on Charpy sized specimens (10 x 10 x 55mm) to assess the resistance to stable crack extension. The results clearly showed a significant effect of static strain ageing on the fracture toughness for the AD microstructure. Pre-cracked Charpy sized specimens were chosen because they are used in surveillance schemes for the nuclear industry [14, 15, 233]. However, smaller specimens tend to fracture under a mix of plane strain and plane stress conditions, reducing the plastic constraint near the crack tip [15, 234]. Due to the fine scale of the weld metal care was taken for the specimen preparation, leading to the attainment of an initial ligament size, permitting enough microstructure to be sampled ahead of the fatigue pre-crack within the process zone. Sampling plays a critical role, at higher temperatures yield stress is lower, therefore the maximum tensile stress available to drive cleavage is also lower, therefore a more potent site to initiate cleavage is needed. Due to specimen size the maximum tensile stress position may not sample a potent site for cleavage, hence, cleavage fracture does not occur, instead the crack front moves forward via the stable crack growth mechanism. Through this mechanism the position of the maximum tensile stress is pushed forward, material is sampled until a potent cleavage initiation site is sampled and catastrophic failure

occurs. It should be noted that CTOD values are calculated from the measurement of physical crack length. In some cases, δ_m , values the ductile crack extension continues after the attainment of the maximum load, where the net specimen section plastically collapses. However, some samples, still fail by cleavage. In Fig. 8.8 and 8.17 for Welds N^o1 and N^o2, respectively, the effect of the amount of stable ductile crack growth and increase in CTOD values is shown. Clearly, the value of CTOD increases as the value of ductile crack growth, Δa increases, therefore, it is noted that an effect of microstructural condition is seen clearly only for the RHAR condition. In Fig. 8.9 and 8.18, the influence of test temperature on the amount of ductile crack growth is shown. In general, the amount of ductile crack growth increases with increasing temperature, although the trend for Weld N^o1 is highly scattered at a given temperature.

Such an analysis indicates the importance of precursor ductile crack growth in determining CTOD toughness values. Such ductile crack growth is interrupted by catastrophic cleavage fracture (for δ_c and δ_u values) and occurs close to the predicted position of the maximum tensile stress (1.9δ), Fig. 8.35 and 8.36. For both welds, the RHAR microstructure exhibits the best CTOD toughness with temperature; see Fig. 8.5 and 8.14 for Weld N^o1 and N^o2, respectively. For this RHAR microstructure a given amount of ductile crack growth (Δa), Fig. 8.8 and 8.17, the CTOD is increased, consistent with more energy absorption with crack advancement.

After strain ageing, the amount of ductile crack growth prior to cleavage at a given temperature, see Fig. 8.18 for Weld N^o2, in particular is reduced from those compared with AR condition. Now it is likely that the resistance to cleavage fracture has been reduced. The load versus displacement curves presented in Fig. 8.1 - 8.4 for Weld N^o1 and 8.10 - 8.13 for Weld N^o2, clearly show that the AD microstructure had a lower CTOD toughness than the RH microstructural condition in both the AR and 5%SA conditions in both welds. In addition, a reduction in work hardening exponent could lead to a lower value of CTOD, δ , per unit of stable crack extension, Δa . This is a similar trend to that seen in Charpy specimens tested in

the transition region, where the amount of absorbed energy per unit of ductile thumbnail extension shown to be lower for the 5%SA condition compared with the AR condition.

8.4.2 Modelling Cleavage Fracture.

Cleavage fracture mechanism in low alloy ferritic steel weld metal occurs under tensile stress controlled fracture mode, where stress develops ahead of a concentrator such as the crack tip. Load is applied to a testpiece, the plastic strain in the process region ahead of a stress concentration increases, thus nucleates a microcrack in a non-metallic inclusion (brittle second phase particle). The microcrack propagates into the surrounding ferrite matrix under the influence of the applied stress, the maximum tensile stress is considered to be temperature independent. The materials toughness and cleavage fracture resistance is controlled by the materials flow properties and the distribution and size of non-metallic inclusions and microstructural parameters of the weld (e.g. grain size and microstructural constituents) within the process zone and crack-tip (region of high stress).

The materials plastic behaviour for example, yield stress and the materials microstructural parameters, distribution of inclusions and grain size, are two main factors which appear to control the weld metals cleavage fracture resistance. Previous studies into the effect of strain ageing on cleavage fracture in C-Mn steels [9, 10, 155, 158, 191, 213] and A533B steels [14, 15] demonstrated that initiation inclusions were located within large allotriomorphic ferrite grains. This is in agreement with the results from fractography examination carried out on cleavage initiation sites on the fracture surfaces of the CTOD specimens, which revealed that within the AD microstructure initiating inclusions were located within large allotriomorphic ferrite grains, presented in change Fig. 8.23 and Fig. 8.29. Patriocinio [15] noted in a recent study of A533B that both the AD and RH microstructures presented similar inclusions size distributions. Fractography revealed that within the RH weld metal region initiating inclusions were located within large cleavage facets, although these cleavage initiation sites are smaller than those observed in the AD microstructural region. It can be assumed that inclusions crack under the influence of dislocation pile-up; hence, large allotriomorphic ferrite

grains would have more influence on cleavage fracture resistance than smaller equiaxed ferrite grains (both before and after microcrack initiation).

CTOD curves clearly show that the toughness of the RHAR microstructure is greater than that of the AD weld metals for both the AR and 5%SA conditions. McRobie and Knott [52] proposed that C-Mn weld metal in a strain aged condition would have a reduced toughness and therefore catastrophically fracture by cleavage at a lower value of CTOD, compared to the AR weld metal, thus increasing the severity of strain ageing which result in smaller values of CTOD.

If global prestrain is uniformly distributed, then the total strain applied should be equally distributed in the equiaxed ferrite of the RH microstructure compared to the AD microstructure, where strain is more easily accommodated by deformation of grain boundary ferrite grains. The morphology of the AD microstructure, e.g. large allotriomorphic ferrite grains and long dislocation pile-up lengths may explain why the AD microstructure is more susceptible to strain ageing and therefore presenting lower cleavage fracture resistance compared to the RH microstructure.

8.4.3 δ -R Data Validity

During this programme of work, pre-cracked Charpy-sized specimens (10x10x55 mm) were chosen mainly because they are often used in surveillance schemes carried out within the nuclear industry. However, there is a general concern with size effects of the specimen and little fracture toughness data has been obtained for small sized specimens. These specimens tend to fracture under a mixture of plane stress and plane strain conditions that reduce the plastic constraint near the crack tip and can raise the CTOD value. The pre-cracked ligament size is only 5mm and the amount of microstructure sampled ahead of the fatigue pre-crack tip in the process zone is small to the extent that even fine weld beads as seen by Weld N^o2 can

sample a single microstructural region by the crack tip. However due to the fine nature of the weld beads, this become more problematic.

Some of the specimens from both weld metals tested above -80°C exhibited catastrophic brittle failure after the attainment of the maximum force plateau. However it is well documented [14, 15, 234, 235] that the maximum load attainable depends on yield stress of the material and on the ligament size. After the attainment of the maximum load the net specimen which collapse plastically, however a number of specimens still failed by cleavage fracture. At higher temperatures, the yield stress is lower and therefore the maximum tensile stress available for cleavage fracture is lower, so sampling plays an increasingly important role. The maximum tensile stress position may not sample such a potent site and therefore cleavage did not intervene and so the crack front moves forward via a ductile crack growth mechanism. As this is happening the position of the maximum tensile stress also moves forward with sampling more material until a potent site for cleavage fracture is sampled and catastrophic fracture results. Within these small samples it appears possible that the crack front can grow to a point where the maximum load occurs without cleavage initiation site being observed and the net section collapse of the specimen starts to occur. The crack is still growing and sampling of more material continues and therefore eventually cleavage fracture intervenes presumably because a potent site has been found. Thus it is plausible that in larger specimens that cleavage fracture might have intervened before the maximum load. On the USE level there is a lot of scatter even after allowing for different initial crack lengths (ligament size). Thus, despite the stable ductile crack tip was located within the top weld bead, the process zone could reach the second weld bead where cleavage fracture occurred, as schematically shown in Fig. 8.37.

In small specimens the USE is determined largely by the maximum load attained before plastic collapse and this is dependent on the load sustaining ligament and therefore its size. This must also affect the amount of stable growth crack that can occur before plastic collapse. For specimens with initial long crack length only a small amount of stable crack growth can occur before the ligament can no longer sustain the load, thus a “m” value is recorded. If the

ligament had been larger the ductile crack growth could have been longer and therefore sampled a potent cleavage fracture initiation site, this could lead to a “u” value being recorded, so care must be employed when interpreting results for small scale testpieces.

8.4.4 Fractography.

The effect of plastically deforming and statically strain ageing the AD microstructure led to a reduction in the value of CTOD at fracture, compared to the RHAR and ADAR weld metal.

Major cleavage initiation sites on the crack-tip opening displacement surfaces were often visually observed to be within allotriomorphic areas. In fact, Novovic [13] concluded that initiating inclusions in the AD microstructure of the C-Mn weld metal were located within allotriomorphic ferrite grains. Patrocínio [15] also observed cleavage initiation sites (CIS) within allotriomorphic ferrite grains for tensile, Charpy impact and blunt notch test specimens in A533B Class 1 steels.

The fracture mechanism in the CTOD testpieces was stable crack growth (microvoid coalescence) followed by cleavage fracture. It was observed that a number of testpieces reached the maximum load plateau, either failing by cleavage fracture, or the test being stopped. Some of the specimens failed under plastic collapse after attaining the maximum load plateau. Microvoid coalescence (MVC) occurs by the internal necking mechanism through the formation of voids around non-metallic inclusions and secondary phase particles by decohesion of the matrix/ inclusion interface. The growth of these voids is aided by plastic deformation, leading to ultimate coalescence and the formation of the final fracture surface. During the stable crack growth, the amount of energy absorbed depends on the weld characteristics, as void nucleation and void growth are influenced by local plastic deformation. The appearance of the cleavage fracture surface differed between the AD and RH microstructures, the microstructure clearly showed coarser facets when compared to the very

fine facets of the RH microstructure, Fig. 8.22 and Fig. 8.26, for the RH and AD microstructures, respectively.

Cleavage fracture initiation sites have been traced to non-metallic inclusions within large cleavage facets which appear to be larger than the average grain size. Hence, the dislocation pile-up length is increased in large grains, meaning higher stress build up against the inclusions within the grain and makes inclusions more liable to crack than those in other grains.

Novovic [13] observed in 9% prestrained C-Mn weld metal a “fast shear” mechanism occurred along shear band of localised plastic strain during ductile fracture instead of internal necking process. Hence overall the strain and fracture toughness associated with microvoid coalescence is significantly smaller in 5%SA condition compared to those in the AR material condition.

It is proposed that the RH microstructure is tougher than the AD microstructure due to their greater resistance to cleavage fracture, as shown by the larger CTOD values observed for the RH microstructure. Critical tensile stress must be exceeded some distance ahead of the crack-tip for cleavage to occur. The local cleavage fracture stress is considered to be temperature independent. The materials toughness and cleavage fracture resistance is controlled by the materials flow properties and the distribution and size of non-metallic inclusions and microstructural parameters of the weld (e.g. grain-size and microstructural constituents) within the process zone and crack-tip (region of high stress). However, as the temperature decreases and the yield stress increases it becomes easier for local tensile stresses to attain the local cleavage fracture stress and hence for cleavage to occur. Also, the AD5%SA microstructural condition exhibited high yield stress compared with both the AR conditions, thus tending to promote cleavage fracture if this model of behaviour is accepted.

The toughness of the RH microstructure is higher than that of the AD microstructure; therefore the crack may have to advance further in a ductile fracture mode until a potent inclusion site is sampled within the RH microstructural region. The McMeeking [232] analysis of the stress distribution ahead of a blunted crack-tip shows the peak tensile stress occurs at a distance of 1.9δ , this distance was calculated from earlier studies by Rice and Johnson [204] and corresponds to fullest extent of logarithmic spiral. Fractography was carried out on all the fracture surfaces, and showed good correlation between the initiation site and its distance (1.9δ) ahead of the stable ductile crack growth.

8.5 Conclusions

1. Fractography has located major cleavage initiation sites, and these are located close to the positions of maximum tensile stress ahead of the ductile crack growth (as predicated through the McMeeking finite element analysis). This supports a micromechanism of failure, where stable ductile crack growth is interrupted by cleavage fracture at a location of peak local tensile stress.
2. Good correlation has been seen between CTOD values and the amount of precursor ductile crack growth. For Weld N^o1 and Weld N^o2, one particular microstructure RHAR, it can be suggested that the ductile crack growth resistance is increased relatively to the other conditions, because a similar amount of ductile crack growth, results in increased CTOD values.
3. The result of strain-ageing appears to be consistent with a reduction in cleavage fracture resistance, because at a given temperature (when cleavage occurs) the amount of ductile crack growth is reduced. This results in lower CTOD values and is seen here, for Weld N^o1 in particular.

Chapter 9 - General Discussion.

9.1 Introduction

Throughout this current body of work a large amount of research and data has been undertaken to analyse a low-alloy ferritic steel weld metal and establish relationships between the microstructure (AD and RH) and its properties in both the as-received and strain aged conditions. The microstructure of the weld has two distinctive regions with very different microstructural constituents; the aim of the study was also to investigate the AD and RH microstructures independently to identify any clear difference in strength and toughness. This chapter brings together the main observations from tensile, Charpy, slow notch bend (fracture stress) and CTOD tests to produce a consistent picture of the factors that control the toughness of such welds. Opportunity is also taken to compare trends between data collected for Weld N^o1, Charpy impact values and fracture stress data, collected as part of a previous programme of work [15], and Weld N^o2, collected as part of this current body of work and analysed collectively.

9.2 Comparison of impact transition curves and CTOD values.

Trends for both such “toughness” tests are similar for the range of microstructural conditions investigated, see Fig. 6.18 and Fig. 8.14. Extremes of behaviour are seen for the RHAR and the AD5%SA conditions in terms of impact energy values and CTOD toughness values with temperature. The importance of precursor crack growth prior to cleavage in controlling impact toughness and CTOD values has been demonstrated, see Fig. 6.25(a) and Fig. 8.17. The observation of unique cleavage fracture initiation sites in blunt notch and CTOD tests has

also confirmed, in general, the importance of maximum local tensile stress in controlling cleavage fracture, see Fig. 7.6 and 8.36.

Impact experimental results have shown that failure at upper shelf energy test temperatures was one of microvoid coalescence, typical of low alloy ferritic steels. The fracture mode is driven by void nucleation on non-metallic inclusions by decohesion of the matrix / inclusions interface and their subsequent growth and final coalescence to form a fracture surface. Extensive fractography of the Charpy, CTOD and tensile specimens tested in both the transition region and the upper shelf region show that non-metallic inclusions act as void initiators after prestraining and static strain ageing. Thus the fundamental ductile failure mechanism is unchanged by this thermomechanical treatment. Another consideration relating to the Charpy and CTOD experimental results is the response at the transition and upper shelf test temperatures, the fracture surface appearance characterised by microvoids is very similar for all conditions. This is a consequence of the virtually identical distribution of non-metallic inclusions for both weld metal regions. Ductile crack growth is dependent mainly on the deformation characteristics of the material, and thus the amount of absorbed energy, in view of the fact that both the void growth and nucleation are processes of local plastic deformation the energy absorbed in the impact test is a reflection of energy spent in the deformation process. Therefore at the upper-shelf and transition temperature range the deformation characteristics of the materials play a key role in the overall impact response. Applying the cold deformation and static strain ageing treatment greatly affects the deformation characteristics of both weld metal regions.

Typically over the temperature range from -120 to 20°C, the yield stress increases by some 100MPa after straining and ageing, Fig. 6.17(a), while the tensile strength is essentially unaffected, Fig. 6.17(b). Naturally, a reduction in work hardening exponent is thus observed from a mean value of 0.19 to 0.11 as a result of strain ageing over this same temperature range, Fig. 6.17(d). The slope of the load-displacement curves post yielding and lower CTOD values observed for the AD5%SA condition confirm that the microvoid coalescence mechanism is affected considerably compared to the AR condition. Thus, for example, the

same amount of stable crack extension the RHAR condition gave higher δ values than for the AD5%SA condition, see Fig. 8.17. In addition to the deformation characteristics of the weld metals the cleavage fracture resistance can also be important for controlling the physical amount of ductile thumbnail extension in the transition region if cleavage results in catastrophic failure.

Local cleavage fracture stress was assessed for both the as-deposited and reheated microstructures, for both conditions, AR and 5%SA. The RH microstructure presented slightly higher cleavage fracture resistance (2078MPa) than the AD microstructure (1910MPa), Table 7.1 Fig. 7.3. After straining and ageing the RH microstructure continues to exhibit higher cleavage fracture resistance (1808MPa) than the AD microstructure (1710MPa); however these values are slightly reduced compared to the AR condition. Previous studies have demonstrated that the temperature at which fracture is coincident with the general yield of the specimen increases with as a result of prestrain and strain ageing on cleavage fracture [47, 230].

These values of σ_{X0} in combination with the yield stress and work hardening exponents measured for each condition, allows the cleavage fracture resistance of each microstructure to be quantified. To a close approximation, both AD and RH microstructures exhibit similar values of yield stress (Fig. 6.17a), work hardening exponents (Fig 6.17(d)) and hence their cleavage fracture resistance will depend directly on the values of σ_{X0} appropriate to each microstructure, Fig 7.3. These values are also closely similar leading to the suggestion that the transition from ductile crack growth to cleavage fracture would occur under near identical conditions. Thus transition temperature energy absorption in Charpy impact test and δ_c , δ_u values obtained in CTOD test might be expected to occur at very similar temperatures. As can be seen in Fig. 6.18 and Fig 8.14 for Charpy and CTOD behaviour respectively, some small difference are still observed. This appears to be as a result (at least in the CTOD test) of a greater value of CTOD resulting from similar level of ductile crack extension, Δa , see Fig. 8.17. This would not have been predicted from the tensile properties evaluated in this current

work, and perhaps suggests the importance of further study to evaluate CTOD resistance curves more carefully.

Such analysis can also be used to compare the performance of the AD and RH microstructures after strain ageing. Now, the cleavage fracture resistance is reduced slightly, see Fig 7.3, but significantly the yield stress is also increased after strain ageing Fig. 6.17. If the mechanism of cleavage fracture is driven by achieving a local tensile stress above σ_{X0} , then less stress intensification of this (higher) yield stress is required, and cleavage fracture should result more easily for such strain age conditions. Indeed this is reflected in both impact and CTOD values, see Fig. 6.18 and Fig. 8.14 respectively. This is also consistent with reduced ductile thumbnail (Fig. 6.25) and reduced Δa , (Fig 8.17) observed in impact and CTOD tests respectively at a given test temperature.

9.3 Trends between Weld N^o1 and Weld N^o2

As mentioned, some preliminary work was carried out on Weld N^o1 as part of a previous body of work [15], assessed Charpy impact values and blunt notch tests. These experiments were revisited as part of the current programme of work, as well as tensile and CTOD tests. Charpy impact values for both Weld N^o1 and Weld N^o2 have been plotted in Fig. 9.1. The ADAR condition absorbed energy values ranged from 3 to 140J for Weld N^o1 and 3 to 143J Weld N^o2. The RHAR condition ranged from 3 to 153J for Weld N^o1 and 4 to 167J Weld N^o2. After 5%SA the AD microstructure absorbed energy values ranged from 5 to 146J for Weld N^o1 and 2 to 105J for Weld N^o2 and for the RH microstructure 5 to 154J and 2 to 140J. Initially it can be seen that the RHAR microstructural condition exhibits the best impact properties when compared to the AD5%SA condition, which exhibited the worst for both weld metals. The upper shelf energy levels for both weld metals are broadly similar, however the 5% condition for Weld N^o2 are slightly lower than those for Weld N^o1. Both weld materials exhibited a 50J shift in USE between the RHAR and AD5%SA condition. After

straining and ageing, for both weld metals there was an increase in the transition temperature and a decrease in the USE.

Examining the two extremes in condition, at DBTT of 40J, the RHAR condition for Weld N^o1 is -80°C compared with -50°C Weld N^o2, the AD5%SA condition exhibited temperatures of 20°C for Weld N^o1 and -10°C for Weld N^o2. The overall difference in DBTT at 40J was 100°C for Weld N^o1 and 65°C Weld N^o2. The Charpy impact values for both RH microstructural conditions are higher for Weld N^o1 compared with Weld N^o2. The ADAR microstructural condition for Weld N^o1 exhibits similar Charpy values for RHAR condition for Weld N^o2, it can also be seen that Weld N^o2 exhibits similar values for ADAR and RH5%SA microstructural conditions. There is good agreement in the Charpy values for both weld materials for AD5%SA microstructural conditions. Both weld materials within the transition region exhibited scatter, however the RH microstructure exhibited more compared with the AD microstructure. One explanation for this is the placement of the notch location, which is relatively difficult for the RH microstructure, whereas the AD microstructure is easier to place due to the geometry of the AD weld bead. For both weld metals and all conditions there is very little scatter on the lower shelf energy levels. For both Charpy and CTOD test data for Weld N^o1 there is clear separation in the data between AR and 5%SA conditions, however this is not as prominent for Weld N^o2, where the ADAR condition exhibited similar as the RH5%SA condition.

Considering both the weld metals as one data set, as plotted in Fig. 9.2, it can be seen there is considerable scatter in the data, especially in the transition region -40 to 0°C, this is more prominent in the RH microstructure compared with the AD microstructure, there is little scatter observed for the AD5%SA condition. The trend remains the same, with the RHAR condition exhibiting lower DBTT and higher USE, compared with the ADAR condition. These are further decreased after straining and ageing, with the AD5%SA condition exhibiting the highest DBTT and lowest USE. At 40J the RHAR condition has a temperature of -70°C compared with -20°C for the ADAR condition, a shift of 50°C. The RH5%SA condition observed a temperature of -40°C compared with 10°C for the AD5%SA condition, a

shift of 50°C. Comparing the best (RHAR) and worst (AD5%SA) conditions, there is a shift of 80°C. Examining USE levels, the RHAR condition exhibited the highest at 158J compared with the worst case of AD5%SA condition of 110J, a decrease of 48J, with the RH5%SA and ADAR having a similar USE level of approximately 135J. There is very little scatter of data of lower shelf energy levels.

Local cleavage fracture stress, σ_{X0} , for both microstructures and both conditions for both weld metals are plotted separately in Fig. 9.3 and together as one set in Fig. 9.4. It can be seen that the local cleavage fracture stress values for both microstructures for Weld N^o2 are slightly higher than those for Weld N^o1, for the AR condition. However after strain and ageing, the local cleavage fracture stress values are now slightly higher for Weld N^o1 compared to Weld N^o2 for both the AD and RH microstructures. The RH microstructure for both conditions also exhibits slightly higher local cleavage fracture stress values compared with AD microstructure. If average values of local cleavage fracture stress σ_{X0} are quoted for each condition for Weld N^o1, then these average values are 1660MPa and 1948MPa for RHAR. After strain ageing the average σ_{X0} values are 1852MPa and 2027MPa respectively. Average σ_{X0} values for Weld N^o2 are previously discussed in Chapter 9.2 and shown in Table 7.1 and Fig. 7.3. However as Fig. 9.3 and 9.4 demonstrate the difference are slight between Weld N^o1 and Weld N^o2.

In summary, the two weld metals can be treated as one data set, however there will be a lot of scatter in the transition region for both the Charpy and CTOD results. The results across all the experiments completed as part of previous programmes of work and this current programme are essentially the same. There are slight differences in upper shelf energy levels, DBTT, hardness values and yield stress values. However, the trends remain that strain and ageing the material reduces upper shelf energy levels and CTOD, slightly reduces cleavage fracture stress and ductile crack resistance and increases DBTT, hardness and yield stress. Given that the scale of the weld beads, with Weld N^o1 having larger beads and few passes compared with Weld N^o2, this close agreement in behaviour gives confidence that underlying micromechanism of crack growth resistance are closely similar for both welds.

Chapter 10 - Conclusions and Suggestions for future work.

10.1 General Conclusions

Tensile and fracture properties of two microstructures (as-deposited (AD) and reheated (RH)) and the possible detrimental effects through prestraining and static strain ageing treatments were assessed for two (simulated) reactor pressure vessel steel weldments. Materials characteristics were assessed through hardness profiles, microstructure and inclusion analysis and GDS. Weld metal toughness was assessed in terms of Charpy impact and tensile tests, and crack-tip opening displacement tests. The cleavage fracture resistance of the two weld metals was measured through slow blunt notch bending tests carried out at -196°C . These tests were carried out for four microstructural conditions ADAR, RHAR, AD5%SA and RH5%SA.

1. Tanh curves were fitted to the impact transition data for both the AD and RH microstructures in both conditions, AR and 5%SA to compare the data in terms of ductile-to-brittle transition temperature (DBTT) at 40J energy level. Strain ageing had the effect both to shift in the transition curve towards higher temperatures for the AR condition and reduce the lower shelf energy level, which is more prominent for the 5%SA condition, the extent of these effects depends on the weld metal microstructure, either AD or RH. Extremes in behaviour were noted between the RHAR and AD5%SA weld metal conditions with a shift of 65°C (at the 40J value). For these extremes of condition a reduction in upper shelf energy level of approximately 53J. Thus these two conditions can be considered as the 'best' (RHAR) and the 'poorest' (AD5%SA) conditions.

2. The upward shift in the ductile-to-brittle transition temperature of both the RH and the AD weld metal microstructures, implies that the 5%SA condition indirectly promoted brittle fracture of these types of weld metals. Strain ageing reduces the upper-shelf energy level and shift the DBTT curves for the AR condition towards higher temperatures.

3. Impact energy values obtained from the Charpy tests for both the AD and RH microstructures in both the AR and 5%SA conditions were found to be subjected to significant variation in the transition region, characteristic of this type of test. Lower shelf impact energy values are much less scattered and are insensitive to both microstructure and treatments. However, at all other temperatures there is a clear trend for specimens with the notch root location in the RH microstructure having greater impact toughness than specimens with a notch located in AD microstructure. Scatter was more prominent in the RH microstructure and this is deduced to be the notch being more difficult to locate in the critical region of the microstructure, due to the fine scale of the weld beads

4. Performing cold deformation and static strain ageing treatments proved to have similar trends in terms of impact energy transition curves as irradiation, hence reducing the upper-shelf energy levels and shifting the transition curve towards higher temperatures. The magnitude of these effects can be related to weld metal microstructure, with the AD microstructure being slightly more sensitive than the RH microstructure.

5. The microstructure is also found to have a marked influence on the slope of the load-displacement curves for the CTOD results, in both the AR and the 5%SA conditions. The RH microstructure showed higher CTOD values compared to the AD

microstructure, in both weld metal conditions, for similar stable crack growth extensions. The extreme effect of static strain ageing on the fracture toughness of the AD microstructure has been confirmed with these CTOD tests. This result strongly supports the idea that the straining and ageing treatment considerably affects the deformation characteristics of the weld metal material.

6. Static strain ageing on the notch toughness of the Charpy specimens affected the AD weld microstructure more compared with the RH microstructure; therefore attention was paid towards the cleavage fracture resistance of the weld metal for different conditions. In terms of local cleavage fracture stress results showed that the AD microstructure had slightly lower cleavage fracture resistance than the RH microstructure, however both of these weld metal microstructures after straining and ageing had similar values of local cleavage fracture stress but with increased values of yield stress. Thus, either cleavage fracture resistance is deduced to be reduced compared with the as-received microstructures. This is consistent with the easier transition from ductile crack extension to cleavage fracture at a given temperature in both impact and CTOD tests, and is the single most important factor in reducing toughness in strain aged material (when such local mechanisms of fracture are in competition).

7. Cleavage fracture initiates from individual non-metallic inclusions at positions close to that of the maximum local tensile stress present ahead of a stress concentration. These are observed to be located in relatively large allotriomorphic ferrite grains for the AD microstructure and equiaxed ferrite grains for the RH microstructure. It was also noted that the distance to the critical initiation site (X_0) is dependent on microstructure as the AD exhibited lower values compared with the RH microstructure in both the AR and 5%SA conditions.

10.2 Suggestions for Future Research

Throughout this thesis numerous topics have been discussed and it is clear that many of the ideas and thoughts have not been fully exhausted. At this current time a complete “simulation procedure” of neutron embrittlement and its effects has yet to be developed. Cold deformation (prestraining) and static strain ageing at 300°C have been used throughout the work in this thesis to suggest the effects of neutron irradiation on this weld metal. Reduction of cleavage fracture stress through grain boundary segregation and the corresponding intergranular fracture mode that may be caused by neutron irradiation, cannot be assessed.

Other areas of interest would be:

- I. To determine cleavage fracture, this is defined by a “microstructural unit” meaning the position, facet/ grain and inclusion size, are analysed. It has also been shown using fractography that cleavage fracture was initiated in large allotriomorphic ferrite grains, this was associated with long dislocation pile up lengths. However this was not measured as part of this current work, therefore the measurement of the density of dislocations and length would be of great interest, experiments could be carried out on both the AR and 5%SA conditions using transmission electron microscopy (TEM) to confirm this theory.
- II. CTOD tests were performed on Charpy - size specimens which had been precracked, the tests were carried out with limited effectiveness for obtaining valid fracture toughness parameters. Larger specimens would need to be employed for future experiments although care over the crack tip would need to be employed to ensure that the desired microstructure/ region of weld metal was being sampled.

- III. More work should be carried out on the modelling of the transition data for the Charpy results. The data collected during this work was analysed using a Tanh fit model, which is strongly influenced by the upper and lower shelf data. Todinov [236, 237] and Novovic [13] have proposed using the Avrami fit, which model the transition region separately from the upper and lower shelves, this may provide a better fit for the data presented in this thesis.

Chapter 11 - References

- 1 J. F. Knott and C. A. English, *Views of TAGSI on the principles underlying the assessment of the mechanical properties of irradiated ferritic steel Reactor Pressure Vessels*, International Journal of Pressure vessels and Piping, Volume 76, Pages 891-908(1999).
- 2 P. Pareige and M. K. Miller, *Characterization of neutron - induced copper - enriched clusters in pressure vessel steel weld: an APFIM study*, Applied Surface Science, Volume 94/95, Pages 370-377(1996).
- 3 P. Pareige, K. F. Russell, R. E. Stoller and M. K. Miller, *Influence of long - term thermal aging on the microstructural evolution of nuclear reactor pressure vessel materials: an atom probe study*, Journal of Nuclear Materials, Volume 250, Pages 176-183(1997).
- 4 J. A. Spitznagel and F. J. Venskytis, *The annealing of copper-vacancy aggregates in neutron-irradiated ferritic pressure vessel steels*, Transactions of the American Nuclear Society, Volume 12, Page 161(1975).
- 5 G. R. Odette, *On the dominant mechanism of irradiation embrittlement of reactor pressure vessel steels*, Scripta Metallurgica. Volume 17, Pages 1183-1188(1983).
- 6 G. R. Odette and G. E. Lucas, *Embrittlement of nuclear reactor pressure vessels*, Journal of Materials, Volume 53-7, Pages 18-22(2001).
- 7 J. H. Tweed and J. F. Knott, *Micromechanisms of failure in C-Mn weld metals*, Acta Metallurgica, Volume 35-7, Pages 1401-1414(1987).
- 8 G. R. Odette, *On the ductile to brittle transition in martensitic stainless steels - Mechanisms, models and structural implications*, Journal of Nuclear Materials, Volume 212-215, Pages 45-51(1994).
- 9 P. Bowen, *Effects of microstructure on toughness in pressure vessel steel*, PhD, Churchill College, University of Cambridge, Cambridge (1984).
- 10 P. Bowen, S. G. Druce and J. F. Knott, *Effects of microstructure on cleavage fracture in pressure vessel steel*, Acta Metallurgica, Volume 63, Pages 339-345(1986).
- 11 P. Bowen and J. F. Knott, *Cleavage fracture of A533B pressure vessel steel in martensitic condition*, Metal Science, Volume 18, Pages 225-235(1984).
- 12 B. Standard, *Guide on methods for assessing the acceptability of flaws in fusion welded structures*.(BS 7910:1999).
- 13 M. Novovic, *Effects of microstructure and pre-straining on ductile to brittle transition in carbon-manganese weld metals*, PhD, Department of Metallurgy and Materials, University of Birmingham, Birmingham (2002).
- 14 M. R. Wenman, *Micromechanisms of fracture in the ductile to brittle transition region of a MoMnNi steel weld metal and a resistant beta titanium alloy*, PhD, Department of Metallurgy and Materials, University of Birmingham, Birmingham (2003).
- 15 A. B. do Patrocínio, *Effect of Prestraining and strain ageing on fracture toughness of MnMoNi steel weld metal*, PhD, Department of Metallurgy and Materials, University of Birmingham, Birmingham (2003).

- 16 B. J. Alloway and D. C. Ayres, *Chemical principles of environmental pollution*, UK: Blackie, Oxford (1993).
- 17 Great Britains Advisory Committee on the Safety of Nuclear Installations, *An Examination of the CBGB's R6 Procedure for the Assessment of the Integrity of Structures Containing Defects*, Report of the ACSNII Study Group on the R6 methodology, H.M.S.O London(1989).
- 18 W. S. Pellini, *Guidelines for Fracture-Safe and Fatigue-Reliable Design of Steel Structures*. The Welding Institute, Abingdon.(1983).
- 19 I. J. O'Donnell and R. Crombie, *On the ΔT_{41} Criterion for Irradiation Shift.*, International Journal of Pressure vessels and Piping, Volume 299-306(1996).
- 20 T. J. Williams, P. R. Burch and C. A. English, *Proceedings on environmental degradation of materials in nuclear power systems - water reactors*, Transverse City: The Metallurgical Society(1987).
- 21 W. Marshall, *An assessment of the integrity of PWR pressure vessels*, UKAEA, LWR Study Group Report, United Kingdom Atomic Energy Authority (1982).
- 22 W. W. Bose, *Micromechanisms of brittle fracture in high strength low alloy steel weld metals*, PhD, Department of Metallurgy and Materials, University of Birmingham, Birmingham (1995).
- 23 K. Dohi, T. Onchi, F. Kano, K. Fukuya, M. Narui and H. Kayano, *Effect of neutron flux on low temperature irradiation remember of reactor pressure vessel steel*, Journal of Nuclear Materials, Volume 265, Pages 78-90(1999).
- 24 L. E. Schubert, A. S. Kumar, S. T. Rosinski and M. L. Hamilton, *Effect of specimen size on the impact properties of neutron irradiated A533B steel*, Journal of Nuclear Materials, Volume 225, Pages 231-237(1995).
- 25 S. R. Ortner, C. E. Lane and C. A. Hipsley, *The effect of flow stress and segregation on the ductile to brittle transition.*, AEA Technology, AEA - T0319, Materials Performance Department, Materials and Chemistry Group, AEA Technology, Didcot, Oxon, OX11 - 0RA.(1996).
- 26 B. A. Gurovich, E. A. Kulehova, Y. I. Shtrombakh, O. O. Zabusov and E. A. Krasikov, *Intergranular and intragranular phosphorus segregation in Russian pressure steels due to neutron irradiation*, Journal of Nuclear Materials, Volume 279, Pages 259-272(2000).
- 27 B. A. Gurovich, E. A. Kuleshova and O. V. Lavrenchuk, *Comparative study of fracture in pressure vessel steels A533B and A508*, Journal of Nuclear Materials, Volume 228, Pages 330-337(1996).
- 28 R. G. Carter, N. Soneda, K. Dohi, J. M. Hyde, C. A. English and W. L. Server, *Microstructural characterization of irradiation-induced Cu-enriched clusters in reactor pressure vessel steels*, Journal of Nuclear Materials, Volume 298, Pages 211-224(2001).
- 29 M. J. Makin and F. J. Minter, *Irradiation hardening in Copper and Nickel*, Acta Metallurgica, Volume 8-October, Pages 691-699(1960).
- 30 Y. H. M. Jung, K. L., *Effect of interstitial impurities on fracture characteristics of A533-B Class 1 pressure vessel steel*, Influence of Radiation on material properties: 13th International symposium, American Society for Testing and Materials, Pages 395-407(1987).
- 31 F. M. Burdekin, J. F. Knott, J. D. G. Sumpter and A. H. Sherry, *TAGSI views on aspects of crack arrest philosophies for pressure vessels with thickness up to 100 mm*,

- International Journal of Pressure vessels and Piping, Volume 76, Pages 879-883(1999).
- 32 E. A. Little, *Strain-aging and neutron scattering studies in irradiated PWR pressure vessel steels*, ASTM: Twelfth International Symposium of the Effects of Radiation on Materials(1984).
- 33 K. L. Murty, *Interstitial - impurity radiation - defect interactions in ferritic steels*, Journal of Metals, Research Summary, Pages 34-39(1985).
- 34 K. L. Murty, *Role and significance of source hardening in radiation embrittlement of iron and ferritic steels*, Journal of Nuclear Materials, Volume 270, Pages 115-128(1999).
- 35 K. L. Murty, *Interaction of interstitial impurities with radiation-induced defects leading to improved elevated temperature technical properties of mild steel*, Nuclear Technology, Volume 67-October, Pages 124-131(1984).
- 36 K. L. Murty, *Beneficial (!) effect of neutron irradiation on mechanical properties of mild steel in blue brittle range*, Scripta Metallurgica, Volume 18, Pages 87-89(1984).
- 37 K. L. Murty and J. O. Dirk, *Friction and source hardening in irradiated mild steel*, Scripta Materialia, Volume 17, Pages 317-320(1983).
- 38 M. Weller and J. Diehl, *Internal friction studies on reactions of carbon and nitrogen with lattice defects in neutron irradiated iron*, Scripta Metallurgica, Volume 10, Pages 101-105(1976).
- 39 R. E. Stoller, B. D. Wirth and G. R. Odette, *Primary damage formation in bcc iron*, Journal of Nuclear Materials, Volume 251, Pages 49-60(1997).
- 40 G. E. Dieter and D. Bacon, *Mechanical Metallurgy*, McGraw-Hill Book Company, London (1988).
- 41 A. Cottrell, *An introduction to metallurgy*, Edward Arnold Ltd: Jesus College, Cambridge (1975).
- 42 A. H. Cottrell, Trans Metall Soc AIME, Volume 212, Pages 192-203(1958).
- 43 K. Nogiwa, Journal of Nuclear Materials, Volume 946, Pages 307-311(2002).
- 44 L. E. Steele, *Review and analysis of reactor vessel surveillance programs, in Statuses of USA Nuclear Reactor Pressure Vessel Surveillance for Radiation Effects.*, ASTM STP 784, Philadelphia: American Society for Testing and Materials, Pages 227(1983).
- 45 ASME, *Boiler and Pressure Vessel Code: Section II*(1995).
- 46 ASME, *Boiler and Pressure Vessel Code: Section III, Appendix G: Protection Against Non-Ductile Failure* (1995).
- 47 J. D. G. Groom and J. F. Knott, *Cleavage fracture in Prestrained Mild Steel*, Metal Science, Volume 9, Pages 390-400(1975).
- 48 E. A. Little and D. R. Harries, *The correlation of radiation-hardening with interstitial nitrogen content in mild steels.*, Met Sci, Volume 4, Pages 195-200(1970).
- 49 E. A. Little and D. R. Harries, *Radiation-hardening and recovery in mild steel and the effects of interstitial Nitrogen.*, Metal Science Journal, Volume 4, Pages 188-199(1970).
- 50 J. D. Baird and A. Jamieson, *Effect of manganese and nitrogen on the tensile properties of iron in the range of 20-600°C.*, Journal of the Iron and Steel Institute, Volume August, Pages 793-803(1966).
- 51 T. Kishi and T. Tanabe, *The Bauschinger effect and its role in mechanical anisotropy.*, Journal of Mechanical and Physics Solids, Volume 21, Pages 303-315(1973).

- 52 D. E. McRobie and J. F. Knott, *Effects of strain and strain aging on fracture toughness of C-Mn weld metal.*, Materials Science and Technology, Volume 1-May, Pages 357-365(1985).
- 53 A. K. Sachdev, *Dynamic strain aging of various steels.*, Metallurgical Transactions A, Volume 13A October, Pages 1793-1797(1982).
- 54 J. K. Chakravartty, A. Haq, T. K. Sinha and M. K. Asundi, *Static strain ageing of ASTM A203D nuclear structural steel*, Transactions of The Indian Institute of Metals, Volume 37-5, Pages 501-507(1984).
- 55 J. K. Chakravartty, S. L. Wadekar, T. K. Sinha and M. K. Asundi, *Dynamic strain-ageing of A203D nuclear structural steel*, Journal of Nuclear Materials, Volume 119, Pages 51-58(1983).
- 56 S. T. Mandziej, *The effect of nitrogen and strain-aging of C-Mn steel welds*. Scripta Metallurgica et Materialia, Volume 27-7, Pages 793-798(1992).
- 57 S. G. Druce, G. Gage and G. Jordan, *Effect of ageing on properties of pressure vessel steels*. Acta Metallurgica, Volume 34-4, Pages 641-652(1986).
- 58 K. C. Kim, J. T. Kim, J. I. Suk, U. H. Sung and H. K. Kwon, *Influences of the dynamic strain aging on the J-R fracture characteristics of the ferritic steels for reactor coolant piping system.*, Nuclear Engineering and Design, Volume 228, Pages 151-159(2004).
- 59 C. S. Seok and K. L. Murty, *Effect of dynamic strain aging on mechanical and fracture properties of A516Gr70 steel.*, International Journal of Pressure vessels and Piping, Volume 76, Pages 945-953(1999).
- 60 S. S. Kang and I. S. Kim, *Dynamic strain aging sensitivity of heat affect zones in C-Mn steels*, Journal of Nuclear Materials, Volume 252, Pages 123-129(1995).
- 61 D. Wagner, J. C. Moreno and C. Prioul, *Dynamic strain aging sensitivity of heat affected zones in C-Mn steels*. Journal of Nuclear Materials, Volume 252, Pages 257-265(1998).
- 62 D. Wagner, J. C. Moreno, C. Prioul, J. M. Frund and B. Houssin, *Influence of dynamic strain aging on the ductile tearing of C-Mn steels: modelling by a local approach method*. Journal of Nuclear Materials, Volume 300, Pages 178-191(2002).
- 63 D. Wagner, C. Prioul and D. Francois, *Sensitivity to dynamic strain aging in C-Mn steels.*, Journal of Alloys and Compounds, Volume 211-212, Pages 132-135(1994).
- 64 B. Ostensson, *The fracture toughness of pressure vessel steel at elevated temperatures.*(1978).
- 65 J. S. Blakemore and E. O. Hall, *Blue-brittle behaviour of mild steel.*, Journal of the Iron and Steel Institute, Volume August, Pages 817-820(1966).
- 66 J. H. Yoon, B. S. Lee, Y. J. Oh and J. H. Hong, *Effects of loading rate and temperature on J-R fracture resistance of an SA516-Gr.70 steel for nuclear piping.*, International Journal of Pressure vessels and Piping, Volume 76, Pages 663-670(1999).
- 67 I. S. Kim, *Dynamic strain - ageing effect on fracture toughness of vessel steels.*, IAEA Technical Committee Meeting on Materials for Advanced Water - Cooled Reactors. Plzen, Volume 76, Plzen. (1991).
- 68 I.-S. Kim and S. S. Kang, *Dynamic strain aging in SA508-class 3 pressure vessel steel.*, International Journal of Pressure vessels and Piping, Volume 62, Pages 123-129(1995).

- 69 J.-W. Kim and I.-S. Kim, *Effect of dynamic strain aging on the leak - before - break analysis in SA106 Gr.C piping steel.*, Nuclear Engineering and Design, Volume 174, Pages 59-67(1997).
- 70 V. Patel, *Effect of dynamic strain ageing on fracture toughness of A533B pressure vessel steel*, N.C. State University: Master of Nuclear Engineering Project Report (1985).
- 71 J. F. Lancaster, *Metallurgy of Welding*, Allen & Unwin, London (1987).
- 72 K. Easterling, *Introduction to the physical metallurgy of welding*, Butterworths(1983).
- 73 A. C. Davies, *The Science and Practice of Welding: The Practice of Welding. Volume 2*, The Cambridge University Press (1989).
- 74 A. C. Davies, *The Science and Practice of Welding: Welding Science and Technology: Volume 1*, The Cambridge University Press(1989).
- 75 L. M. Gourd, *Principles of Welding Technology*, Edward Arnold (1995).
- 76 P. Miao, *Effects of inclusions on fracture and hydrogen assisted cracking in ferritic welds*, PhD, Department of Metallurgy and Materials, University of Birmingham, Birmingham (2003).
- 77 G. M. Evans, *Effect of interpass temperature on the microstructure and properties of C-Mn all-weld metal deposits*, International Institute of Welding (IIW), II-A-490-78(1978).
- 78 O. Grong, *Metallurgical Modelling of Welding*. Cambridge: The Institute of Materials(1997).
- 79 O. Grong and N. Christensen, *Factors controlling MIG weld metal chemistry*, Scand. J. Metall, Volume 12, Pages 155-165(1983).
- 80 E. T. Turkdogan, *Proceeding International Conference on Chemical Metallurgy of Iron and Steel*, Sheffield: The Iron and Steel Institute (UK)(1971).
- 81 N. Bailey and R. J. Pargeter, *The influence of Flux type on the strength and toughness of the submerged arc weld*. The Welding Institute, Abingdon. (1988).
- 82 C. Hseith, S. S. Babu, J. M. Vitek and S. A. David, *Calculation of inclusion formation in low alloyed steel welds*, Material Science and Technology, Volume A215, Pages 84-91(1996).
- 83 J. M. Grreg and H. K. D. H. Bhadeshia, *Titanium rich mineral phases and the nucleation of bainite*, Metall Trans A, Volume 25A, Pages 1063-1611(1994).
- 84 A. A. Sudgen and H. K. D. H. Bhadeshia, *The non-uniform distribution of inclusions in low-alloy steel weld deposits.*, Metall Tran A, Volume 19A, Pages 669-674(1988).
- 85 N. S. Pottore, C. I. Garcia and A. J. DeArdo, *Interrupted and isothermal solidification studies of low and medium carbon steels*. Metall Trans A, Volume 22A, Pages 1871-1880(1991).
- 86 M. Nakonishi, *Doc IX-1281-83*, IIW(1983).
- 87 G. J. Davies and J. G. Garland, *Solidification structures and properties of fusion welds*, Inter Metall Reviews, Volume 20, Pages 83-106(1975).
- 88 W. F. Savage and G. H. Aronson, *Preferred orientation in the weld fusion zone.*, Weld J, Volume 45, Pages S85-S89(1966).
- 89 A. O. Kluken, O. Grong and J. Hjelen, *The origin of transformation textures in steel weld metals containing acicular ferrite.*, Metall Tran A, Volume 22A, Pages 657-663(1991).
- 90 T. H. Edvardson, H. Fredriksson and I. Svensson, *Met Sci*, Volume 10, Pages 298-306(1976).
- 91 H. Fredriksson, *Metall Trans*, Volume 3, Page 2989(1972).

- 92 M. Hansen and K. Anderko, *Constitution of binary alloys*, McGraw-Hill, New-York (1958).
- 93 E. C. Rollason, *Metallurgy for engineers*, Edward Arnold, London (1961).
- 94 Y. Ito and M. Nakanishi, *Journal of Japan Weld Soc*, Volume 44, Pages 815-821(1975).
- 95 Y. Ito and M. Nakanishi, *Sumitono Search*, Volume 15, Pages 42-62(1976).
- 96 R. A. Farrar and M. N. Watson, *Metal Construction*, Volume 17, Series Volume 374R(1985).
- 97 R. E. Dolby, *Metals Technology*, Volume 10, Pages 349-362(1983).
- 98 H. K. D. H. Bhadeshia and L.-E. Svensson, *The microstructure of submerged arc - weld deposits for high - strength steels*, *Journal of Materials Science*, Volume 24, Pages 3180-3188(1989).
- 99 N. T. Suutala, T. Taklo and T. Moision, *Metall Tran A*, Volume 19A, Pages 1183-1190(1979).
- 100 S. A. David, *Weld J*, Volume 60, Pages S63-S71(1981).
- 101 Davies, *Editorial*. *International Journal of Pressure vessels and Piping*, Volume 77, Pages iii-iv(2000).
- 102 D. R. Davies, A. C. Roberts and D. Ness, *A review of the design and construction of the Sizewell B pressurized water reactor building containment structures.*, *Nuclear Engineering and Design*, Volume 156, Pages 259-268(1995).
- 103 R. C. Cochrane, *World in the World* (1983).
- 104 R. C. Cochrane, *Doc. IXJ-102-85*, International Institute of Welding (IIW)(1985).
- 105 J. G. Garland and P. R. Kirkwood, *Towards improved submerged arc weld metal.*, *Metal Construction*, Volume 5, Pages 275-283(1975).
- 106 D. J. Widery, PhD, University of Cambridge, Cambridge (1974).
- 107 J. G. Garland and P. R. Kirkwood, *Proceeding Inter Symp on Welding of Line Pipe Steels.*, St. Louis (USA), Welding Research Council (New York)(1977).
- 108 P. L. Harrison and R. A. Farrar, *Influence of oxygen-rich inclusions on the gamma-alpha phase transformation in high-strength low-alloy (HSLA) steel weld metals.*, *Journal Mater Sci*, Volume 16, Pages 2218-2226(1981).
- 109 R. A. Ricks, G. S. Barritte and P. R. Howell, *Solid-State phase transformation*. Metallurgical Society of AIME, Pittsburg, Pages 463-468(1981).
- 110 R. A. Ricks, G. S. Barritte and P. R. Howell, *The nature of acicular ferrite in HSLA steel weld metals*, *Journal of Materials Science*, Volume 17, Pages 732-740(1982).
- 111 R. W. K. Honeycombe, *Steels - Microstructure and Properties*, Edward Arnold Ltd, London (1980).
- 112 C. A. Dube, H. I. Aaronson and R. F. Mehl, *Rev Met*, Volume 55, Pages 201-210(1958).
- 113 J. F. Knott, *Recent advances in the micro-modelling of cleavage fracture in steel*. George R. Irwin Symposium on Cleavage Fracture, The Minerals, Metals & Materials Society, Pages 171-182(1997).
- 114 H. K. D. H. Bhadeshia, B. Grefott and S. L. E., *The austenite grain structure of low-alloyed steel deposits*, *Journal Mater Sci*, Volume 21, Pages 3947-3951(1986).
- 115 H. K. D. H. Bhadeshia, L. E. Svensson and B. Grefott, *Acta Metallurgica*, Volume 33, Pages 1271-1283(1985).
- 116 J. M. Dowling, J. M. Corbett and H. W. Kerr, *Inclusions phases and the nucleation of acicular ferrite in submerged-arc welds in high-strength low-alloy steels.*, *Metall Trans A*, Volume 17A, Pages 1611-1623(1986).

- 117 A. R. Mills, G. Thewlis and J. A. Whiteman, *Nature of inclusions in steel weld metals and their influence on formation of acicular ferrite.*, Material Science and Technology, Volume 3, Pages 1051-1062(1987).
- 118 C. Liu and S. D. Bhole, *Fracture behaviour in a pressure vessel steel weld.* Materials & Design, Volume 23, Pages 371-376(2002).
- 119 S. Liu and D. L. Olson, *The role inclusions in controlling HSLA steel weld microstructures.*, Weld Journal, Volume 65, Pages 139s-150s(1986).
- 120 N. A. Fleck, Weld J, Volume 65, Pages 113S-150S(1986).
- 121 D. J. Abson and R. E. Dolby, *A scheme for the quantitative description of ferritic weld metal microstructure.* Welding Institute Research Bulletin, Volume 21, Pages 100-103(1980).
- 122 M. Strangwood, PhD, The University of Cambridge(1987).
- 123 D. A. Porter and K. E. Easterling, *Phase transformation in metals and alloys*, Working (England): Van Nostrand Reinhold(1981).
- 124 J. D. Verhoeven, *Fundamentals of physical metallurgy*, John Wiley & Son, New York (1975).
- 125 H. K. D. H. Bhadeshia and J. W. Christian, *Bainite in steel*, Metall Trans, Volume 21A, Pages 767-797(1990).
- 126 R. E. Dolby, *Factors controlling weld toughness-The present position. Part 2 weld metals*, Welding Institute Research Bulletin, Report R/RB/M93/76 (1976).
- 127 M. Strangwood and H. K. D. H. Bhadeshia, *Proce Int Confe on Advances in Welding Science and Technology*, ASM: International Metals Park, OH(1986).
- 128 H. K. D. H. Bhadeshia, L. E. Svensson, H. Cerjack and K. E. Easterling, *In mathematical modelling of weld phenomena*, The Minerals, Metals and Materials Society(1993).
- 129 L. E. Svensson and B. Grefot, *Microstructure and impact of C-Mn all-weld metals deposits.* Weld J, Volume 69-12, Pages 454s-461s(1990).
- 130 G. M. Evans, *The effect of carbon on the microstructure and impact toughness of C-Mn all-weld metal deposits*, Weld J, Volume 62-11, Pages 313S-320S(1983).
- 131 G. M. Evans, *The effect of silicon on the microstructure and properties of C-Mn all-weld metal deposits*, Metal Construction, Volume 18, Pages 438R-444R(1986).
- 132 G. M. Evans, *The effect of chromium on the microstructure and properties of C-Mn all-weld deposits*, Weld Metal and Fabrication, Volume 57, Pages 346S-358S(1989).
- 133 G. M. Evans, *The effect of nickel on the microstructure and properties of C-Mn all-weld metal deposits*, OERLINKON-ScweiBmitt, Volume 48, Pages 18-35(1990).
- 134 G. M. Evans, *The influence of aluminium on the microstructure and properties of all-weld metal deposits*, Weld J, Volume 70, Pages 32s-39s(1991).
- 135 G. M. Evans, *The effect of niobium in manganese containing MMA weld deposits.*, OERLINKON-ScweiBmitt, Volume 49, Pages 24-39(1991).
- 136 G. M. Evans, *Effect of manganese on the microstructure and properties of all-weld metal deposits*, IIW, II-A-432-77(1977).
- 137 O. Grong and D. K. Matlock, *Microstructural development in mild and low-alloyed steel weld metals*, Int. Met. Rev, Volume 31, Pages 27-48(1983).
- 138 E. S. Kayali, A. J. Pacey and H. W. Kerr, *The effects on Mo, Zr and To on submerged arc weld metal: II Toughness.* , Can. Metal Quarterly, Volume 23, Pages 227-236(1984).
- 139 G. M. Evans, *The effect of titanium in SMA C-Mn steel multipass deposits*, Weld J, Volume 71-2, Pages 447S-454S(1992).

- 140 A. H. Koukabi, T. H. North and B. H. B., *Properties of submerged arc deposits-effects of zirconium, vanadium and titanium/ boron.*, Metal Construction, Volume 12, Pages 639-642(1979).
- 141 M. Es-Souni, P. A. Beaven and G. M. Evans, Material Science Engineering, Volume A130, Pages 173-184(1990).
- 142 O. Grong, *Catalyst effects in heterogeneous nucleation of acicular ferrite.* Metall Mater Trans, Volume 26A-3, Pages 525-534(1995).
- 143 J. H. Tweed and J. F. Knott, *Effects of reheating on microstructure and toughness of C-Mn weld metal.*, Metal Science, Volume 17 February, Pages 45-54(1983).
- 144 J. F. Knott, *Fundamentals of fracture mechanics*, Butterworth & Co Ltd, London (1973).
- 145 A. A. Griffith, Phil. R. Soc, Volume 221, Pages 163(1920).
- 146 G. R. Irwin, *Analysis of stresses and strain near the end of crack traversing a plate.*, Journal of Applied Mechanics, Volume 24, Pages 361-364(1957).
- 147 E. Orowan, Trans. Engrs Shipbuilders Scotland, Volume 89, Pages 165(1945).
- 148 H. M. Westergaard, Journal of Applied Mechanics, Volume A39, Pages 60(1939).
- 149 *British Standard - Fracture mechanics toughness tests - Part 1: Method for determination of K_{IC} , critical CTOD and critical J values of metallic materials.*(BS 7448-1:1991).
- 150 J. F. Knott, *Some effects of hydrostatic tension on the fracture behaviour of mild steel*, J. I. S. I, Volume 204, Pages 104-111(1966).
- 151 J. F. Knott, Journal of Mechanical and Physics Solids, Volume 15, Pages 97-103(1967).
- 152 P. Bowen, S. G. Druce and J. F. Knott, Acta Metallurgia, Volume 35, Pages 1735-1746(1987).
- 153 P. Bowen and J. F. Knott, Metallurgical Transactions A, Volume 17A, Pages 231-241(1986).
- 154 C. Yan, Metallurgical Transactions A, Volume 24A, Pages 1381(1992).
- 155 D. A. Curry and J. F. Knott, *The effects of microstructure on the cleavage fracture stress in steels*, Metal Science, Pages 511-514(1978).
- 156 A. T. Price, H. A. Holl and A. P. Greenough, Acta Materialia, Volume 12, Pages 49(1964).
- 157 G. T. Hahn, *Fracture*, Wiley, New York (1959).
- 158 D. A. Curry and J. F. Knott, *The relationship between fracture toughness and microstructure in the cleavage fracture of mild steel.*, Metal Science, Volume January, Pages 1-6(1976).
- 159 D. E. McRobie, PhD, University of Cambridge, Cambridge (1985).
- 160 E. T. Wessel, *Practical fracture mechanics for structural steel*, UKAEA, Chapman and Hall, Volume H(1969).
- 161 *British Standard - Fracture mechanics toughness tests - Part 4: Method for determination of fracture resistance curves and initiation values for stable crack extension in metallic materials.*(BS 7448-4:1991).
- 162 Geesthacht, GKSS_94/E/60, *The GKSS test procedure for determining the fracture behaviour of materials: EFAM GTP 94*, GKSS - Forschungszentrum Geesthacht GmbH(1994).
- 163 J. R. Griffiths and D. R. J. Owen, *An elastic-plastic stress analysis for a notched bar in plane strain bending.*, Journal of Mechanical and Physics Solids, Volume 19, Pages 419-431(1971).

- 164 P. Bowen, C. A. Hipsley and J. F. Knott, *Applications of electron microscopy to micromechanisms of brittle failure in Electron microscopy plasticity and fracture research of materials*. International Symposium, Holzau(1989).
- 165 A. Cottrell, Iron and Steel Institute Spec Rep, Volume 69, Pages 281(1961).
- 166 A. A. Wells, *Unstable crack propagation in metals: Damage and fast fracture*, Proc. Syp Crack Propagation, Cranfield (1962).
- 167 A. A. Wells, *Application of fracture mechanics at and beyond general yielding*, B.W.R.A Report, British Welding Research Association, Volume 23, Pages 563-570(1963).
- 168 A. A. Wells, *Unstable crack propagation in metals: Cleavage and fast fracture*
- 169 F. M. Burdekin and D. E. W. Stone, *The crack opening displacement approach to fracture mechanics in yielding materials*, Journal of Strain Analysis, Volume 1-2, Pages 145-153(1966).
- 170 B. Wang and K.-C. Hwang, *Structural integrity assessment in elastic-plastic fracture*. Engineering Fracture Mechanics, Volume 54-4, Pages 471-478(1996).
- 171 C. G. Chipperfield, J. F. Knott and R. F. Smith, Third International Congress on Fracture, Volume April, Munich (1973).
- 172 D. R. Harries, *The "state of the art" in crack tip opening displacement (CTOD) testing and analysis*, Metal Construction, Volume 12, Pages 415-605(1980).
- 173 R. R. Barr, *The measurement of COD and its application to defect significance.*, Metal Construction, Volume 7, Pages 604-610(1975).
- 174 J. R. Low, *Symposium on relation of properties to microstructure*. American Society for Testing and Materials, Pages 153(1954).
- 175 C. Zener, *Fracture of Metals*, ASM, Cleveland, OH (1948).
- 176 A. N. Stroh, Proc R. Soc, Volume A(223), Pages 404(1954).
- 177 A. N. Stroh, Adv Physics, Volume 6, Pages 418(1957).
- 178 N. J. Petch, *The cleavage strength of polycrystals*, Journal of the Iron and Steel Institute, Volume 174, Pages 25-28, London (1953).
- 179 E. Orowan, *Reports Prog Phys*, Volume 12, Pages 185(1949).
- 180 E. R. Parker, *Brittle behaviour of Engineering Structures*, Wiley, New York (1957).
- 181 G. G. Chell and D. A. Curry, *Developments in fracture mechanics*, Applied Publishes, Pages 101(1981).
- 182 C. J. McMahon and M. Cohen, Acta Metallurgia, Volume 13, Pages 591-604(1965).
- 183 W. H. Brucker, Journal of Welding, Volume 29, Pages 467(1950).
- 184 J. P. Allen, W. P. Hopkins and H. R. Tripler, *Tripler, Tensile and impact properties of high-purity iron-carbon-manganese alloys of low carbon content*, J.I.S.I., Volume 174, Pages 103-120(1953).
- 185 E. Smith, *Physical Basis of Yield and Fracture*, Inst. Phsics. Soc, Pages 36, Oxford (1966).
- 186 J. F. Knott, *Atomistic of Fracture.*, NATO Advanced Research Institute on Atomistic of Fracture, Corsica, France, Pages 209-240(1983).
- 187 J. F. Knott, *Fracture, Plastic Flow and Structure Integrity*, IOM Communications, Pages 21-43(2000).
- 188 N. J. Petch, Iron and Steel Institute Spec Rep, Volume 173, Pages 25, London (1953).
- 189 E. O. Hall, *The deformation and aging of mild steel: iii discussion of results*, Proceedings of the Physical Society of London, Volume B64, Pages 747-753 London (1951).

- 190 E. Smith, *The stress distribution near the tip of an array of screw dislocations piled up against an inclusion*, Journal of Mechanical and Physics Solids, Volume 20, Pages 307-312(1972).
- 191 D. A. Curry and J. F. Knott, *Effects of microstructure on cleavage fracture stress in steel*. Metal Science, Volume November, Pages 511-514(1978).
- 192 N. Okumura, *Cleavage fracture of low carbon ferritic steels with fine grain size*. Metal Science, Volume 17 December, Pages 581-589(1983).
- 193 J. J. Lewandowski and A. W. Thompson, *In Fracture*, ICF 6 ED, Volume 2, Pages 1515-1524(1984).
- 194 J. J. Lewandowski and A. W. Thompson, *Microstructural effects on the cleavage fracture - stress of fully pearlitic eutectoid steel*, Metall Trans, Volume 17A, Pages 1769-1786(1986).
- 195 D. J. Alexander and I. M. Bernstein, *Cleavage fracture in pearlitic eutectoid steel*, Metall Trans, Volume 20A, Pages 2321-2335(1989).
- 196 J. F. Knott, *Reliability and structural integrity of advanced materials*, A.S.a.D.R.i. S Sedmak, Volume 2, Pages 1375-1400(1992).
- 197 P. A. S. Reed and J. F. Knott, *Fatigue and Fatigue*, Engineering Mater Struct, Volume 15, Pages 1251-1270(1992).
- 198 P. A. S. Reed and J. F. Knott, *Fatigue and Fracture Engng*, Materials Struct, Volume 19, Pages 485-500(1996).
- 199 R. O. Ritchie, W. L. Server and R. A. Wullaert, *Critical fracture stress and fracture strain models for the predication of lower and upper shelf toughness in nuclear pressure vessel steels.*, Metallurgical Transactions A, Volume 10A October, Pages 1557-1570(1979).
- 200 X. Z. Zhang, PhD, Department Metallurgy and Materials, University of Birmingham, Birmingham (1996).
- 201 X. Z. Zhang, *A study on crack growth in ductile materials.*, International Journal of Pressure vessels and Piping, Volume 76, Pages 583-590(1999).
- 202 X. Z. Zhang and J. F. Knott, *Cleavage fracture in bainitic and martensitic microstructures*. Acta Metallurgica, Volume 47-12, Pages 3483-3495(1999).
- 203 R. O. Ritchie, J. F. Knott and J. R. Rice, *On the relationship between critical tensile stress and fracture toughness in mild steel.*, Journal of Mechanical and Physics Solids, Volume 21, Pages 395-410(1973).
- 204 J. R. Rice and M. A. Johnson, *Inelastic behaviour of Solids*, McGraw - Hill, New York (1970).
- 205 J. F. Knott, *Fracture*, Canada, Waterloo(1977).
- 206 R. Iricibar, G. leRoy and J. D. Embury, *Relationship of strain hardening and damage in ductile failure.*, Metal Science, Volume 14, Pages 337-343(1980).
- 207 A. S. Argon, J. Im and R. Safoglu, *Cavity formation from inclusions in ductile fracture of A508 steel*, Metallurgical Transactions A, Volume 6A, Pages 825-837(1975).
- 208 L. M. Brown and W. M. Stobbs, *The work-hardening of copper-silica v. equilibrium plastic relaxation by secondary dislocations.*, Philosophical Magazine, Volume 34, Pages 351-372(1976).
- 209 S. Flooreen and H. W. Hayden, Scripta Materialia, Volume 4, Pages 87-94(1970).
- 210 T. B. Cox and J. R. Low, Metall Trans, Volume 5A, Pages 1457-1470(1974).
- 211 J. R. Rice and D. M. Tracey, *On the ductile enlargements of voids in triaxial stress fields.*, Journal of Mechanical and Physics Solids, Volume 201-217(1969).
- 212 P. F. Thomason, *Ductile fracture of metals*. Pergamon Press, Oxford (1990).

- 213 J. F. Knott, *Characteristic microstructural features of different types of fracture*. 2nd Griffith Conference Institute of Materials, Pages A1-A12(1995).
- 214 C. Naudin, J. M. Frund and A. Pineau, *Intergranular fracture stress and phosphorous grain boundary segregation of a Mn-Ni-Mo Steel.*, Scripta Materialia, Volume 40-9, Pages 1013-1019(1999).
- 215 M. A. Islam, *Intergranular fracture in 2.25Cr-1Mo Steel at low temperature.*, PhD, Metallurgy and Materials, University of Birmingham, Birmingham (2001).
- 216 P. L. Threadgill and S. J. Garwood, *Final Contract Report - The assessment of weldments in SA 533B Class 1 steel plate*, Contract A72b-1327, for: Nuclear Installations Inspectorate, The Welding Institute.(1980).
- 217 ASTM, *Standard test methods for determining average grain size using semiautomatic and automatic image analysis*, ASTM, West Conshohocken (1997).
- 218 E. E. Underwood, *Quantitative sterology*, Addison - Wesley Publishing Co., London (1970).
- 219 *Notched Bar Tests: Method for Precision Determinations of Charpy V-Notch Impact Energies for Metals*(BS 131 - Part 7: 1989).
- 220 D. J. F. Ewing, *Calculations on the bending of rigid / plastic stress analysis for a notched bar in plane strain bending*, Journal Mechanical and Physical Solids, Volume 19, Pages 419-431(1968).
- 221 *British Standard - Fracture mechanics toughness tests - Part 2: Method for determination of K_{IC} , critical CTOD and critical J values of welds in metallic materials.*(BS 7448-2:1991).
- 222 R. O. Ritchie and K. J. Bathe, *On the calibration of the electrical potential technique for monitoring crack growth using finite element methods*, International Journal of Fracture, Volume 15, Number 1, Pages 47-55(1979).
- 223 J. F. Knott, *The transition from fibrous fracture to cleavage fracture.*, International Journal of Pressure vessels and Piping, Volume 64, Pages 225-234(1995).
- 224 G. S. Barritte, R. A. Ricks and P. R. Howell, *Proc. conf. quantitative microanalysis with high spatial resolution*. London: Metals Soc.(1981).
- 225 R. Blondeau, *Mathematical model for the calculation of Mechanical Properties of Low-Alloy Steel Metallurgical Products: a few examples of its applications.*, Heat Treatment, London Metal Society (1976).
- 226 P. L. Harrison, M. N. Watson and R. A. Farrar, *How Niobium Influences SA Mild Steel Weld Metals. Part 2: Continuous Cooling Transformation (CCT) Diagrams*, Weld Metal and Fabrication, Volume 49, Pages 161-169(1981).
- 227 M. Lambrigger, *Ductile-to-brittle transition of low activation ferritic-martensitic steels with respect to critical cracks promoting final brittle fracture.*, Engineering Fracture Mechanics, Volume 71, Pages 633-646(2004).
- 228 K. Shiba and A. Hishinuma, *Low-temperature irradiation effects on tensile and Charpy properties of low-activation ferritic steels.*, Journal of Nuclear Materials, Volume 283-287, Pages 474-477(2000).
- 229 V. J. Farron, *Effects of microstructure on fracture toughness in A533B submerged-arc welds*. Master Thesis, Metallurgy and Materials, University of Birmingham.(2004).
- 230 R. Sandstrom, G. Engberg and Y. Bergstrom, *Metal Science*, Volume 15, Page 409-412.(1981).
- 231 D. A. Curry and J. F. Knott, *Effect of microstructure on cleavage fracture toughness of quenched and tempered steels*. Metal Science, Volume June, Pages 341-345(1979).

- 232 R. M. McMeeking, *Finite deformation analysis of crack-tip opening inelastic-plastic materials and implications for fracture.*, Journal of Mechanical and Physics Solids, Volume 25, Pages 357-381(1977).
- 233 R. Nicholson, *Private Conversation with Principal inspector of HSE NII*(2007).
- 234 M. El - Shennawy, F. Minami, M. Toyoda and K. Kajimoto, *Crack - tip plastic constraint activators and the application to plane - strain fracture toughness test: Proposal on small - size fracture toughness specimens.* Engineering Fracture Mechanics, Volume 63, Pages 447-479(1999).
- 235 S. Jitsukawa, A. Naito and J. Segawa, *Effect of size and configuration of 3-point bend bar specimens on J-R curves.* Journal of Nuclear Materials, Volume 271&272, Pages 87-91(1999).
- 236 M. T. Todinov, J. F. Knott and M. Strangwood, *An assessment of the influence of complex stress states on martensite start temperature.*, Acta Metallurgica, Volume 44-12, Pages 4909-4915(1996).
- 237 M. T. Todinov, M. Novovic, P. Bowen and J. F. Knott, *Modelling the impact energy in the ductile/brittle transition region of C-Mn multi-run welds.*, Materials Science and Engineering, Volume A287, Pages 116-124(2000).
- 238 Incontiguous Brick, <http://incontiguousbrick.wordpress.com> Incontiguous Brick, *Map showing location of nuclear reactors*, Internet source(2008).
- 239 British Energy, <http://www.british-energy-com> British Energy, *Various*, Internet Source(2008).
- 240 Weld Reality, <http://weldreality.com/ship-broke-in-two.gif> Weld Reality, *Liberty Ship*, Internet Source(2008).
- 241 The Welding Institute TWI, <http://www.twi.co.uk> The Welding Institute TWI, *Submerged arc welding*, Internet Source(2008).
- 242 S. Kou, *Welding Metallurgy*, Wiley, 2002, 2nd Edition(2002).
- 243 NDT Resource Centre, <http://www.ndt-ed.org/index-flash.htm> NDT Resource Centre, *Loading modes*, Internet source(2008).
- 244 A. Neimitz, *Dugdale model modification due to the geometry induced plastic constraints*, Engineering Fracture Mechanics, Volume 67, Pages 251-261(2000).
- 245 B. Wang and K.-C. Hwang, *An engineering approach to safety assessment for non-J-controlled crack controlled.* Engineering Fracture Mechanics, Volume 57-6, Pages 689-699(1997).